REPORT DOCUMENTATION PAGE

Form Approved
OMB No. 0704-0188

(2)

2. REPORT DATE	3. REPORT TYPE AND DATES COVERED
11-13-91	Annual 10-1-90 - 9-30-91

4. TITLE AND SUBTITLE
Theoretical Analysis of Microwave and Millimeter Wave Integrated Circuits Based on Magnetic Films

5. FUNDING NUMBERS
N00014-89-J-1019

4143115-02

6. AUTHOR(S)
Prof. J.A. Kong

7. PERFORMING ORGANIZATION NAME(S) AND ADDRESS(ES)
Research Laboratory of Electronics
Massachusetts Institute of Technology
77 Massachusetts Avenue
Cambridge, MA 02139

8. PERFORMING ORGANIZATION REPORT NUMBER

9. SPONSORING/MONITORING AGENCY NAME(S) AND ADDRESS(ES)
Office of Naval Research
800 North Quincy Street
Arlington, VA 22217

10. SPONSORING/MONITORING AGENCY REPORT NUMBER

11. SUPPLEMENTARY NOTES
The view, opinions and/or findings contained in this report are those of the author(s) and should not be construed as an official Department of the Army position, policy, or decision, unless so designated by other documentation.

12a. DISTRIBUTION/AVAILABILITY STATEMENT
Approved for public release; distribution unlimited.

12b. DISTRIBUTION CODE

13. ABSTRACT *(Maximum 200 words)*

Work by Prof. Kong and his collaborators is summarized here

14. SUBJECT TERMS

15. NUMBER OF PAGES

16. PRICE CODE

17. SECURITY CLASSIFICATION OF REPORT	18. SECURITY CLASSIFICATION OF THIS PAGE	19. SECURITY CLASSIFICATION OF ABSTRACT	20. LIMITATION OF ABSTRACT
UNCLASSIFIED	UNCLASSIFIED	UNCLASSIFIED	UL

NSN 7540-01-280-5500

Standard Form 298 (Rev 2-89)
Prescribed by ANSI Std Z39-18
298-102

ANNUAL REPORT

Title: THEORETICAL ANALYSIS OF MICROWAVE AND MILLIMETER WAVE INTEGRATED CIRCUITS BASED ON MAGNETIC FILMS

Sponsor by: Department of the Navy
Office of Naval Research

Contract number: N00014–89–J–1019

Research Organization: Center for Electromagnetic Theory and Applications
Research Laboratory of Electronics
Massachusetts Institute of Technology

OSP number: 71387

Principal Investigator: J. A. Kong

Period covered: October 1, 1990 – September 30, 1991

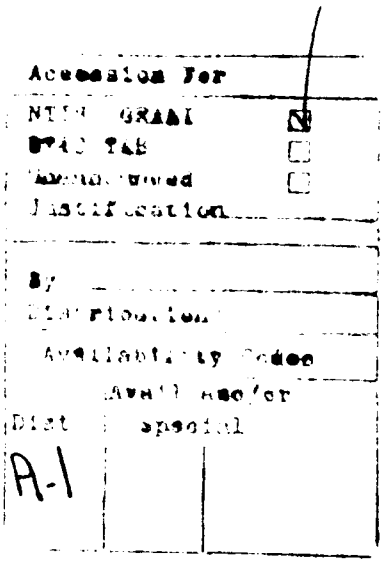

THEORETICAL ANALYSIS OF MICROWAVE AND MILLIMETER WAVE INTEGRATED CIRCUITS BASED ON MAGNETIC FILMS

Under the sponsorship of the ONR Contract Contract N00014-89-J-1019 we have published 24 refereed journal and conference papers.

A full modal analysis is used to study the dispersion characteristics of microstrip lines periodically loaded with crossing strips in a stratified uniaxially anisotropic medium. Dyadic Green's functions in the spectral domain for the multilayered medium in conjunction with the vector Fourier transform (VFT) are used to formulate a coupled set of vector integral equations for the current distribution on the signal line and the crossing strips. Galerkin's procedure is applied to derive the eigenvalue equation for the propagation constant. The effect of anisotropy for both open and shielded stuctures on the stopband properties is investigated.

The input impedance of a microstrip antenna consisting of two circular microstrip disks in a stacked configuration driven by a coaxial probe is investigated. A rigorous analysis is performed using a dyadic Green's function formulation where the mixed boundary value problem is reduced to a set of coupled vector integral equations using the vector Hankel transform. Galerkin's method is employed in the spectral domain where two sets of disk current expansions are used. One set is based on the complete set of orthogonal modes of the magnetic cavity, and the other employs Chebyshev polynomials with the proper edge condition for the disk currents. An additional term is added to the disk current expansion to properly model the current in the vicinity of the probe/disk junction. The input impedance of the stacked microstrip antenna including the probe self-impedance is calculated as a function of the layered parameters and the ratio of the two disk radii. Disk current distributions and radiation patterns are also presented. The calculate results are compared with experimental data and shown to be in good agreement.

The coupled-wave theory is generalized to analyze the diffraction of waves by chiral gratings for arbitrary angles of incidence and polarizations. Numerical results for the Stokes parameters of diffracted Floquet modes versus the thickness of chiral gratings with various chiralities are calculated. Both horizontal and vertical incidences are considered for illustration. The diffracted waves from chiral gratings are in general elliptically polarized; and in some particular instances, it is possible for chiral gratings to convert a linearly polarized incident field into two nearly circularly polarized Floquet modes propagating in different directions.

A general spectral domain formulation to the problem of radiation of arbitrary distribution of sources embedded in a horizontally stratified arbitrary magnetized linear plasma is presented. The fields are obtained in terms of electric and magnetic type dyadic Green's functions. The formulation is considerably simplified by using the kDB system of coordinates in conjunction with the Fourier transform. The distributional singular behavior of the various dyadic Green's functions in the source region is investigated and taken into account by extracting the delta function singularities. Finally, the fields in any arbitrary layer are obtained in terms of appropriately defined global upward and downward reflection and transmission matrices.

We have investigated a method for the calculation of the current distribution, resistance, and inductance matrices for a system of coupled superconducting transmission lines having finite rectangular cross section. These calculation allow accurate characterization of both high-T_c and low-T_c superconducting strip transmission lines. For a single stripline geometry with finite ground planes, the current distribution, resistance, inductance, and kinetic inductance are calculated as a function of the penetration depth for various film thickness. These calculations are then used to determine the penetration depth for Nb, NbN, and $YBa_2Cu_3O_{7-x}$ superconducting thin films from the measured temperature dependence of the resonant frequency of a stripline resonator. The calculations are also used to convert measured temperature dependence of the quality factor to the intrinsic surface resistance as a function of temperature for a Nb stripline resonator.

Proximity-print x-ray lithography is commonly performed with gold or tungsten structures of sizes down to 30 nm wide and 50–800 nm tall which are patterned onto the surface of a thin, x-ray transparent membrane. X-rays in the wavelength range of 0.5–5 nm are used for replication with mask-substrate gaps ranging from zero (contact print) up to 20 μm or more. The resolution o f this method (minimum achievable linewidth) is limited predominantly by the diffraction of the x-rays *around* these structures and the spreading of the diffracted waves *into* the 0–20 μm gap. Work to date has assumed that scalar diffraction theory is applicable—as calculated, for example, by the Rayleigh-Sommerfeld formulation—and that Kirchhoff boundary conditions can be applied. Kirchhoff boundary conditions assume that the fields are constant in the region between the absorbers, and also (a different) constant in the region just under the absorbers, and that there are no fringing fields. In this report we explore the validity of this assumption for the case of 30 nm-wide by 30–100 nm-tall gold absorbers with 4.5 nm (C_K) x-rays. Because of computational time limitations, the shorter wavelength and larger absorber cases are not currently possible.) Because the absorber is only 7 wavelengths wide and 7–20 wavelengths high, strong diffractive effects are expected. The finite-difference time-domain (FD-TD) technique was used on a Cray-2 supercomputer to predict the fields diffracted by the gold absorbers. In applying the FD-TD technique, Maxwell's equations are discretized in space and time on a uniform rectangular grid. A second-order absorbing boundary condition is applied at the outer boundary of the computational domain in order to simulate unbounded space. The results indicate that strong fringing fields exist in the shadow region of the absorber, and hence Kirchhoff boundary conditions are not accurate in this regime.

Because the effects of diffraction during proximity-print x-ray lithography are of critical importance, a number of previous researchers have attempted to calculate the diffraction patterns and minimum achievable feature sizes as a function of wavelength and gap. Work to date has assumed that scalar diffraction theory is applicable–as calculated, for example, by the Rayleigh-Sommerfeld formulation–and that Kirchhoff boundary conditions can be applied. Kirchhoff boundary conditions assume that the fields (amplitude and phase) are constant in the open regions between absorbers, and a different constant in regions just under the absorbers (i.e., that there are no fringing fields). An x-ray absorber is, however, best described as a lossy dielectric that is tens or hundreds of wavelengths tall, and hence Kirchhoff boundary conditions are unsuitable. In this report we use two

numerical techniques to calculate (on a Cray 2 supercomputer) accurate diffracted fields from gold absorbers for two cases: a 30 nm-wide line at $\lambda = 4.5$ nm, and a 100 nm-wide line at $\lambda = 1.3$ nm. We show that the use of Kirchhoff boundary conditions introduces unphysically high spatial frequencies into the diffracted fields. The suppression of these frequencies–which occurs naturally without the need to introduce an extended source or broad spectrum–improves exposure latitude for mask features near 0.1 μm and below.

In order to understand the physical meaning of rational reflection coefficients in one-dimensional inverse scattering theory for optical waveguide design, we have studied the relation between the poles of the transverse reflection coefficient and the modes in inhomogeneous dielectrics. By using a stratified medium model it is shown that these poles of the reflection coefficient have a one-to-one correspondence to the discrete modes, which are the guided and leaky modes. The radiation modes have continuous real values of transverse wave numbers and are not represented by the poles of the reflection coefficient. Based on these results, applications of the Gel'fand-Levitan-Marchenko theory to optical waveguide synthesis with the rational function representation of the transverse reflection coefficient are discussed.

We developed an inversion algorithm based on a recently developed inversion method referred to as the Renormalized Source-Type Integral Equation approach. The objective of this method is to overcome some of the limitations and difficulties of the iterative Born technique. It recasts the inversion, which is nonlinear in nature, in terms of the solution of a set of linear equations; however, the final inversion equation is still nonlinear. The derived inversion equation is an exact equation which sums up the iterative Neuman (or Born) series in a closed form and; thus, is a valid representation even in the case when the Born series diverges; hence, the name *Renormalized* Source-Type Integral Equation Approach.

The scattering and receiving characteristics of a probe-fed stacked circular microstrip antenna, both as an isolated element and in an infinite array, are investigated.

The receiving case, where the antenna is loaded with impedance Z_L, is solved by superposition, decomposing the problem into the scattering case with $Z_L = 0$ and the transmitting case. In the scattering case, the coaxial probe is short-circuited to the ground plane and the induced probe current I_1 due to an incident plane wave excitation is determined. In the transmitting case, a voltage V is applied to the base of the probe and the input impedance Z_{in} is solved for, giving a relationship between the applied voltage V and the transmitting probe current I_2. With the knowledge of I_1 and Z_{in}, for a given load impedance Z_L, the total probe current, $I = I_1 + I_2$, and the received power are determined.

The scattering and transmitting problems are solved rigorously using a dyadic Green's function formulation where the mixed boundary value problem is reduced to a set of coupled vector integral equations for the unknown disk and probe currents. Galerkin's method is employed in the spectral domain where the disk current distributions are expanded in terms of the complete set of transverse magnetic (TM) and transverse electric (TE) modes of a cylindrical resonant cavity with magnetic side walls. An additional term is added to the disk current expansion to properly model the singular behavior of the current in the vicinity of the probe, to ensure continuity of the current at the probe/disk junction, and to speed up the convergence of the solution.

The radar cross section (RCS) of a single stacked microstrip antenna is calculated for both the open and short-circuited cases. For an infinite array of phased elements, the reflection coefficient seen at the input of the antenna and the received power are calculated.

The complex resonant frequencies of the open structure of a microstrip antenna consisting of two circular microstrip disks in a three layer stacked configuration have been rigorously calculated as a function of the layered parameters and the ratio of the radii of the two disks. Using a dyadic Green's function formulation for horizontally stratified media and the vector Hankel transform, the mixed boundary value problem is reduced to a set of coupled vector integral equations. Employing Galerkin's method in the spectral domain, the complex resonant frequencies are calculated and convergence of the results is demonstrated. It is shown that for each mode, the stacked circular microstrip structure has dual resonant frequencies which are associated with the two coupled constitutive resonators of the structure and which are a function of the mutual coupling between them. This mutal coupling depends on the geometrical configuration of the stacked structure, the layered

parameters, and the disk radii. The maximum coupling effect occurs where the real parts of the resonant frequencies of the constitutive resonators are approximately equal, where the behavior of the resonances in this region is a function of the coupling. The dual frequency behavior of the stacked microstrip structure, easily controlled by varying the parameters of layer 2 and disk radii ratio, given fixed parameters for layer 1 and layer 3, may be used to broaden the bandwidth or provide for dual frequency use of the antenna.

We rigorously analyze the radiation problem of a circular patch which is center fed by a coaxial-line driven probe over a ground plane and situated in an arbitrary layered medium. The current distribution on both the patch and the probe is rigorously formulated using a planar stratified medium approach. A set of three coupled integral equation is derived which governs the axial current distribution on the probe, the radial current distribution on the patch and the azimuthal magnetic current sheet across the aperture of the driving coaxial line. This set of equations is then solved using the method of moments. The resulting matrix equation is obtained in terms of Sommerfeld-type integrals that take into account the effect of the layered medium. These integrals are efficiently computed by a simple deformation in the complex wavenumber domain. The probe current distribution, input impedance and radiation pattern are presented and compared to the case of a uniform probe current distribution.

Microstrip antennas of stacked configurations have received attention in recent years for both wideband and dual frequency use, overcoming the narrow bandwidth of conventional single layer microstrip antennas. Although much experimental work has been performed, theoretical analyses of stacked microstrip patches is limited. Resonant frequencies of the stacked microstrip antennas have been rigorously calculated. Numerical methods have been used to calculate the current and radiation fields of a stacked microstrip antenna. The method of moments has been applied to analyze to the stacked microstrip structure when excited by an incident plane wave. A spectral domain iterative analysis for a stacked microstrip antenna where the antenna is described by a rectangular sampling grid has been used to calculate radiation patterns. This analysis does not allow for accurate modeling of the probe feed.

In our approach, the input impedance and radiation fields of a coaxial probe-fed microstrip antenna consisting of two circular microstrip disks in a stacked configuration are investigated. Using a dyadic Green's formulation, a rigorous analysis of the microstrip antenna is performed for two stacked configurations. Assuming uniform current along the probe, the mixed boundary value problem is reduced to a set of coupled vector integral equations using the vector Hankel transform and solved using Galerkin's method in the spectral domain. Due to the singular nature of the current on the driven disk in the vicinity of the probe, an additional term is included in the current expansion to account for the divergent nature of the current near the probe feed junction and insure continuity of the current at the junction.

The input impedance and radiation patterns of the stacked microstrip antenna is calculated as a function of the layered substrate, permittivities and thicknesses, and the ratio of the radii of the two disks. Both dual frequency and wideband operation is discussed.

Microstrip discontinuities, such as open end, gap and step in width, have been widely studied by many authors. There are different methods for analyzing microstrip discontinuities, such as quasi-static approach, planar waveguide model and integral equation formulation. As the frequrncy gets higher, the quasi-static assumption is not valid. In the planar waveguide model analyses, the thickness of the substrate is assumed much smaller than the wavelength so that a two-dimensional model may be applied. In this case, the effect of the radiation and the surface waves are not considered. The integral equation method has been applied to study the open end and gap dicontinuities on isotropic substrates. In applying the integral equation method, various approximation were introduced in the computation procedure. More recently, finite element expansion currents are used to formulate a full-wave analysis of micristrip discontinuities on isotropic substrates.

The open end, gap and step in width discontinuities placed on anisotropic substrates are rigorously analyzed. Both uniaxial and tilted uniaxial anisotropy are considered. The materials are assumed to be lossless and the metal strips to be infinitely thin. A dyadic Green's function for layered anisotropic media is used to formulate a set of vector integral equations for the current distribution. The fundamental hybrid mode is assumed to be propagating on the input and output of microstrip lines. In solving the set of vector integral equations, the method of moment is employed. The basis functions for the current on the metal strip consider the edge effect. Both logitudinal and transverse currents are considered in the calculation. The propagation constant for the infinitely long uniform microstrip line is first calculated. Then the propagation constant of the fundamental mode is used to formulate the excitation of the discontinuity problem. At the discontinuity, local basis functions are used to simulate the local currents near the discontinuity. The scattering matrix can then be obtained, and an equivalent circuit model can be proposed. The effect of the anisotropy is investigated and the results are discussed.

The leakage phenomenon is important in the area of millimeter-wave integrated circuits and integrated optics. Theoretical analyses and experiments have been performed to investigate this phenomenon. The leakage is due to the TE-TM coupling occurring at the geometrical discontinuities, and the leaky power in the form of surface wave propagates in the background medium.

There are different methods to analyze the dielectric strip waveguides, including the approximate field matching method, effective dielectric constant (EDC) method, mode matching method, etc. The first two methods are approximate, and can not be used to predict the imaginary part of the propagation constant. In the third one, ground planes have to be put at some distance away from the guiding structure, hence the effect of radiation loss is neglected.

An integral equation formulation using dyadic Green's function is derived to solve for the dispersion relation of single and coupled dielectric strip waveguides. A method to predict the leakage is presented, and the leakage properties are investigated.

Three different dielectric strip waveguides are investigated : optical rib waveguide, strip dielectric guide, and insulated image guide. Both single and coupled strip waveguides are studied. The cross section of the dielectric strips are assumed to have rectangular shape. Applying the Galerkin's method, the field distribution on the cross section are represented by a set of unit pulse basis functions. Substituting these basis functions into the integral equations, and choosing the same set of basis functions as the testing functions, we can obtain a determinant equation from which the propagation constant can be solved.

For single dielectric strip waveguide, it is observed that the leakage occurs when the effective refractive index is smaller than that of a surface wave mode in the background medium. It is also observed that if the lowest TE-like (TM-like) mode is leaky, the lowest TM-like (TE-like) mode is non-leaky. When the lowest order mode leaks, the surface wave mode of opposite polarization is excited. When the higher order mode leaks, the surface wave modes of both polarizations can be excited.

For two symmetrical dielectric strip waveguides, both the even and odd modes are investigated. For the leaky mode, the total leakage is due to the leakage from each individual strip waveguide. At the separation where the even mode has a maximum leakage, it implies that the surface wave modes excited by each waveguide add in phase. For the odd mode at about the same separation, these coaxial line feed, the reflection coefficient for the TEM mode is obtained which allows one to compute the input impedance at the terminals of the probe. Numerical results for the input impedance are presented.

A finite difference time domain technique for two dimensional time domain scattering of electromagnetic waves is derived. The triangular grids and the control region approximation are employed to discretize Maxwell's equations. The finite difference time domain techniques with uniform rectangular grids has been used in the past. The scatterers are modeled using staircases and, recently, the accuracy of this approximation has been investigated. Several types of other grids have been proposed to improve the staircase approximation. Generalized nonorthogonal grid can model scatterer without staircasing. It has been applied to spherical systems, yet they appear to be cumbersome for general scatterers. The "distorted rectangular grid" model approximates the computational domain using rectangular grids and distorts the boundary grids to fit the interfaces. The triangular

grid is used in this paper, which is very flexible in dealing with arbitrary scatterers and absorbing boundaries.

The control region approximation, which calls for Delaunay and Dirichlet tessellation, has been successfully applied to the frequency domain problems in the past. Two double integral terms are obtained by integrating the Helmholtz equation about the Delaunay tessellation. The term involving the Laplace operator can be converted to a closed loop integral of normal derivatives, which can easily be approximated in finite difference manner by utilizing the orthogonal property of Delaunay and Dirichlet tessellation. The remaining term can be approximated by multiplying the field at the node with the area. In the time domain problem, the same approximation is applied to the wave equation, except the term involving time derivatives is used in time marching scheme. Alternatively, as in Yee's algorithm, the first order Maxwell's equations are solved by spatially and temporally separating the electric and magnetic fields. In the case of electric polarization, the electric fields are placed at the nodes and the magnetic fields are placed at the center of triangular edges. The curl H equation is integrated by applying Stoke's theorem and convert it to a closed loop integral of tangential magnetic fields. This equation can be used to advance electric fields in time. To update magnetic fields, the second curl equation is used. This equation is approximated in the finite difference manner by utilizing the orthogonality property of the tessellation. The equations for the magnetic polarization case can also be derived following the similar procedure.

In order to limit the computation domain, the scatterers are enclosed with artificial outer boundaries. Continuous smooth outer boundaries, such as circles and ellipses, are chosen. The second-order time domain absorbing boundary conditions derived from the pseudo-differential operator approach is imposed at the outer boundaries. These boundary conditions are implemented with the control region approximation to determine necessary field quantities at the boundary. The results of the time domain control region approach are presented for simple scatterer geometries, such as conducting and coated cylinders and strips, by calculating both the transient and time-harmonic responses.

The Finite-Difference Time-Domain (FD-TD) method was first introduced by Yee who discretized Maxwell's time dependent curl equations with second-order accurate central-difference approximations in both the space and time derivatives. Since then, it has been applied extensively to scattering and wave absorption problems. Application of the FD-TD method to microstrip problems, in which frequency-domain approaches have dominated, has so far attracted little attention until recently it was used to obtain frequency characteristics of microstrip cavities. Also, it has been extended to the analyses of open microstrip line and microstrip discontinuity problems where absorbing boundary conditions are needed for the simulation of the unbounded domain. However, only isotropic or simple anisotropic media are considered in the above papers.

A new FD-TD grid model is used to solve microstrip problems in anisotropic media having tilted optical axes expressed by permittivity or permeability tensor with off-diagonal elements. This grid model is indeed a superposition of two conventional grids with some displacement which depends on the optical axes of anisotropy. Implementations of different boundary conditions are discussed. Using this model, the frequency-dependent characteristics of microstrip lines are investigated. The microstrips are assumed to be placed on top of anisotropic substrates with tilted optical axes. The case with superstrates is also investigated.

In the finite difference computation, the open-end termination is simulated by using the open-circuit, short-circuit technique. The source plane is implemented by using a magnetic wall with a Gaussian pulse excited on the surface under the strip. Because of the symmetry of the problem, the region under consideration can be reduced by half, using a magnetic-wall at the center plane.

The fields at different positions are first calulated. Then the Fourier Transform is taken to give the field spectra from which the voltage and current can also be obtained. Using these data, the effective permittivity and the characteristic impedance can be determined. The frequency characteristics of microstrip lines in anisotropic media obtained by this method are compared with the published results.

Finite difference time domain (FDTD) techniques show great promise in their ability to solve three dimensional problems with arbitrary geometry. Advantages of this method include the ability to model spatially or temporally varying media. These advantages are due to the complete discretization of both space and time. Considering the volume of information being calculated these techniques are very efficient and are well suited to calculation on future parallel processing computers. This method was first formulated by Yee in 1966 and his basic algorithm is still in use. Recent work has demonstrated the applicability of the FDTD technique to microstrip problems. The centered finite difference approximations used are second order accurate in both space and time yielding good results for reasonable mesh sizes. Numerical techniques used to solve electromagnetic problems must limit the domain over which the fields are to be calculated. This mandates the use of an absorbing boundary condition to simulate the outward propagation of waves incident on the walls of the mesh. An absorbing boundary condition has been developed by Mur based on the work of Enquist and Majda.

Our work in this area includes development of the algorithms mentioned above into a general purpose computer code which may be used to solve for the transient response of electromagnetic problems with an arbitrary geometry. In addition to the transient response, frequency domain parameters may be obtained by fourier transform of the time domain results. Since the fields are calculated throughout space and time all other desired parameters may be calculated from the field quantities. Specifically, we are analyzing rectangular microstrip structures with as many as two or more ports. Such structures may be used in MMIC filters or antennas. This problem is of interest for several reasons. First, there are existing frequency domain solutions to the resonance problem of a rectangular microstrip patch, which we may compare with the FDTD solution. Secondly, the FDTD technique may be used to analyze coupling of microstrip lines to the rectangular structure. This coupling may be either a direct connection or a gap coupled connection. Advantages of the FDTD solution of this problem are that it is a full wave solution which allows for radiation or surface wave loss and that no empirical values such as "effective" dimensions are needed for the analysis, also the geometry may be altered easily to allow for various connections or coupling to the patch. This is a significant improvement over methods which rely on a planar circuit approach in which the substrate thickness must be small

compared to wavelength and inherently three dimensional coupling problems are not easily handled. Comparison of our results with various planar circuit approaches will be made.

A new perturbation series, coupled integral equation approach for calculating the frequency dependent circuit parameters for quasi-TEM transmission lines with lossy conductors is presented. The method considers the addition of loss and dispersion to be perturbations on the lossless TEM case, and therefore the difference between the propagation constant and the wavenumber in free space is a small parameter. We obtain the lowest order term of the perturbation series by solving two quasistatic problems; the electrostatic problem to get the capacitance, and the magnetoquasistatic problem, with the distribution of current inside the wire considered, which gives the frequency-dependent inductance and resistance. Both of these problems are solved using one-dimensional integral equations for quantities on the surface of the conductor; this represents a significant improvement in efficiency over previous methods. For most cases of practical interest, the lowest order term of the series will suffice. If, however, the change in the propagation constant from the lossless case, due to the altered inductance and the addition of resistance, is significant, additional terms in the perturbation series can be calculated.

The method is illustrated with the case of one or more wires embedded in a uniform dielectric. In the original magnetoquasistatic problem, the current is entirely directed along the axis of propagation, and satisfies the frequency-domain diffusion equation. Outside the wire, the magnetic vector potential is in the same direction, and obeys Laplace's equation. The boundary conditions are the continuity of tangential and normal magnetic field at the interface, which can be expressed in terms of the current density and vector potential and their derivatives. Since we can express the ratio of the frequency-dependent resistance to the DC resistance in terms of the values of the volume current and its normal derivative on the surface of the wire only, we can use a pair of coupled integral equations to solve for these quantities alone, which we can solve by Galerkin's method or other finite element methods.

Results obtained using this technique are shown for some important cases, including rectangular wires, and are compared with earlier methods and with experimental data. Previous methods for calculating the resistance fall into three categories. First, for certain cases, exact analytical results can be obtained. Secondly, especially in the case of a rectangular wire, the cross-section can be divided into rectangular segments, each much smaller than a skin-depth, across which the current is assumed to be constant. Magnetoquasistatics gives simple answers for the resistance and self-inductance of each element, and the mutual inductance between elements. This leads to a matrix equation which is solved for the current distribution. The disadvantages of this technique are that it requires basis functions throughout the cross-section of the conductor, which is especially intensive as the frequency gets large. Also, closed form expressions for the matrix elements only exist when the elements are rectangular — other shapes, such as triangular patches, which might be used to fit a wire of arbitrary shape, lead to nested numerical integrals.

The third method used is a variational procedure. This is similar to the method presented here, except that the current and the magnetic vector potential are expanded in functions which span the entire cross-section. This has two drawbacks: first, it requires that there be a closed outer conductor, which is not physical in many important cases. Second, as in the previous method, using elements which fill the entire cross-section increases the computation time unnecessarily, since only the value of the current and its normal derivative at the surface of the wire are needed to calculate the resistance.

A new method for analyzing frequency-dependent transmission line systems with nonlinear terminations is presented. The generalized scattering matrix formulation is used as the foundation for the time domain iteration scheme. Compared to the admittance matrix approach proposed in a previous paper, it has the advantage of shorter impulse response which leads to smaller computer memory requirement and faster computation time. Examples of a microstrip line loaded with nonlinear elements are given to illustrate the efficiency of this method.

As the speeds of integrated circuits increase, the effect of interconnection lines becomes more and more important. Traditional lumped element circuit model must be supplemented by the transmission line model in order to account for propagation delays, dispersion and losses. This has created needs for new numerical procedures that can be easily incorporated into current CAD tools. To make matters more complicated, the interconnection lines are terminated with not only linear resistors but also nonlinear semiconductor devices, such as diodes and transistors.

Several techniques are now commonly used to deal with nonlinear circuit problems, for example, the direct time domain approaches, and the semi-frequency-domain approaches, such as the harmonic balance technique. The semi-frequency-domain approaches are useful for microwave and millimeter wave integrated circuits but become impractical for digital integrated circuits because of the latter's wide band nature. On the other hand, frequency-dependent parameters often make it awkward to apply the direct time domain approach to the interconnection line systems.

We propose a hybrid frequency-domain time-domain technique based on the generalized scattering matrix formulation. For an n line system, we define $2n$ scattering parameters according to the frequency-dependent characteristic impedances of individual lines ($Z_{0j} = \sqrt{L_{jj}(\omega)/C_{jj}(\omega)}$). The time-domain transfer matrix (impulse response) of this $2n$-port system is then obtained by the inverse Fourier Transform. Lastly, the nonlinear equations associated with terminal characteristics are incorporated and solved with iteration procedures such as the Newton-Ralphson method.

The key to efficient and stable solutions in this problem is shortening the duration of every transfer matrix element. With the generalized scattering parameters approach, we are able to achieve that yet eliminating the need for artificial matching networks adopted by a previous work. Furthermore, the use of individual characteristic impedances in the definition of scattering parameters enables us to generalize this method to coupled lines with distinct properties while keeping the duration of transfer matrix elements short. This cannot be realized if traditional scattering parameters are used. We shall illustrate the elegance and efficiency of our approach for a dispersive microstrip line with different nonlinear loads and excited with narrow Gaussian pulses. The elements of transfer matrix are found out to be either zero or single retarded delta-impulse accompanying a small

spike with very narrow spread. Typical computation time for a 1000 time-step iteration ranges from 4 to 27 seconds on a VAXStation 3500. The effects of line dispersion and load nonlinearity will be clearly delineated in the presentation.

The transient propagation characteristics of VLSI interconnects with discrete capacitive loads at various locations is analyzed based on a hybrid transmission lines-lumped element circuit model. Exact expressions of the Laplace transform of unit step responses are first obtained through the ABCD matrix formulation. We then apply the equivalent dominant pole approximation to the transfer function with the propagation delays factored out. The approximated transfer function can be inverted in closed form and quickly evaluated. These results provide efficient ways of finding approximately the effects on delays and rise time brought by VLSI off-chip interconnects.

Because of the dramatic increase in device densities on microelectronic chips, the propagation delay for off-chip interconnects has become the limiting factor to the speed of VLSI packages. Typical scales of these interconnects will be comparable or larger to the characteristic wavelength of high frequency components of the signal. Therefore, to calculate the delays caused by these interconnects properly, a hybrid circuit model containing transmission line sections as well as lumped elements must be used in place of the all-lumped element one. Most circuit simulation packages are nevertheless based on the latter and have to resort to subsection approximation when dealing with transmission lines. This scheme will undoubtedly lead to lengthy computation, which is not desirable when a quick, heuristic estimate of bounds are needed for the initial phase of the design cycle.

Two approaches have been developed for obtaining the approximate transient response without lengthy simulation. The first kind of solution techniques emphasize the calculation of bounds to voltage responses from the differential equations either by direct integration or by using the optimal control theory. On the other hand, the second kind of techniques analyze the properties of Laplace transform domain solution. Thus far, their applications are limited to all lumped-element and distributed RC networks, which can only take care of on-chip interconnects. We shall take the second approach by incorporating transmission line elements for off-chip delay estimation.

Our configuration includes a series of transmission line sections with arbitrary discrete capacitances and resistances loaded at junctions. The ABCD matrix formulation is used to obtain the Laplace transform of the unit step response. We express the latter in the form of $\exp(-sT)/Q(s)$, where $Q(s) = A_0(s) + A_1(s)\exp(s\tau_1) + A_2(s)\exp(s\tau_2) + \cdots$ with all $\{A_i(s)\}$ being rational functions in s. The factor $\{\exp(-sT)\}$ is identified with direct transmission delay over the total length of the line. For the rest part $(1/Q(s))$, we proceed to apply the equivalent dominant pole approximation technique[7]. Either a single negative real pole or second-order complex conjugate pair will be chosen for approximation depending upon the property of lumped loads at junctions as well as the source impedances. A phase-correction factor $\exp(-sT_m)$ is introduced to make up for the discrepancies caused by our low-order approximation. The first-order and second order approximations enable us to obtain closed-form solution to the transient response. Comparison of the approximated responses with those obtained from brute-force numerical Laplace inversion shows very good match when the propagation delay of an average transmission line section is less than half the product of junction load capacitance and transmission line characteristic impedance. Yet we only have to spend a fraction of the time for computations. The accuracy of this method will be discussed in detail with some examples of lossless transmission line networks in which lumped capacitors are loaded at regular intervals.

The propagation properties of single and coupled inhomogeneous slab waveguides are analyzed. An integral equation formulation using the dyadic Green's function which covers both the TE and TM modes is proposed. The dispersion relations are obtained by applying the Galerkin's method to solve the integral equation. The coupling between two symmetrical inhomogeneous slab waveguides is also investigated. This method is shown to be applicable to arbitrary dielectric constant profiles.

The guidance and leakage properties of single and coupled dielectric strip waveguides are analyzed using the dyadic Green's function and integral equation formulation. Galerkin's method is used to solve the integral equation for the dispersion relation. The effects of the geometrical and the electrical parameters on the dispersion relation are investigated. A method to predict the occurrence of leakage is proposed. The properties of the even and the odd leaky modes are also investigated. Results are compared with previous analysis and shown to be in good agreement.

A spectral domain dyadic Green's function for multilayered uniaxially anisotropic media containing three-dimensional sources is derived. Tractable forms are shown to be easily deduced from the physical picture of the waves radiated by the primary sources and the multiple reflections from the stratified medium. The formulation decomposes the dyadic Green's function into TE and TM waves. The dyadic Green's function in the source region is properly represented by extracting the delta function singularity. A simple proceedure to obtain the fields in any arbitrary layer is described. Recursion relations for appropriately defined reflection and transmission coefficients are presented. Forms suitable for transmission line applications in multilayered media are derived.

Full modal analysis is used to study the dispersion characteristics of microstrip lines periodically loaded with crossing strips in a stratified uniaxially anisotropic medium. Dyadic Green's functions in the spectral domain for the multilayered medium in conjunction with the vector Fourier transform (VFT) are used to formulate a coupled set of vector integral equations for the current distribution on the signal line and the crossing strips. Galerkin's procedure is applied to derive the eigenvalue equation for the propagation constant. The effect of anisotropy for both open and shielded structures on the stopband properties is investigated.

A direct three dimensional finite difference time domain (FDTD) method is applied to the full-wave analysis of various microstrip structures. The method is shown to be an efficient tool for modelling complicated microstrip circuit components as well as microstrip antennas. From the time domain results, the input impedance of a line-fed rectangular patch antenna and the frequency dependent scattering parameters of a low pass filter and a branch line coupler are calculated. These circuits are fabricated and the measurements are compared with the FDTD results and shown to be in good agreement.

A rigorous dyadic Green's function formulation in the spectral domain is used to study the dispersion characteristics of signal strip lines in the presence of metallic crossing strips. A set of coupled vector integral equations for the current distribution on the conductors is derived. Galerkin's method is then applied to derive the matrix eigenvalue equation for the propagation constant. The dispersion properties of the signal lines are studied for both cases of finite and infinite length crossing strips. The effects of the structure dimensions on the passband and stopband characteristics are investigated. For crossing strips of finite length, the stopband is mainly affected by the period, the crossing strip length, and the separation between the signal and the crossing strips. For crossing strips of infinite length carrying travelling waves, attenuation along the signal line exists over the whole frequency range of operation.

PUBLICATIONS SUPPORTED BY ONR CONTRACT N00014-89-J-1019 SINCE 1988

Integral equation solution to the guidance and leakage properties of coupled dielectric strip waveguides (J. F. Kiang, S. M. Ali, and J. A. Kong), *IEEE Transactions on Microwave Theory and Techniques,* Vol. 38, No. 2, 193–203, February 1990.

Application of the three dimensional finite difference time-domain method to the analysis of planar microstrip circuits (D. M. Sheen, S. M. Ali, M. D. Abouzahra, and J. A. Kong), *IEEE Transactions on Microwave Theory and Techniques,* Vol. 38, No. 7, 849–857, July 1990.

The propagation characteristics of signal lines with crossing strips in multilayered anisotropic media (C. W. Lam, S. M. Ali, and J. A. Kong), *Journal of Electromagnetic Waves and Applications,* Vol. 4, No. 10, 1005–1021, 1990.

Input impedance of a probe-fed stacked circular microstrip antenna (A. N. Tulintseff, S. M. Ali, and J. A. Kong), *IEEE Transactions on Antennas and Propagation,* Vol. 39, No. 3, 381-390, March 1991.

Analysis of diffraction from chiral gratings (S. H. Yueh and J. A. Kong), *Journal of Electromagnetic Waves and Applications,* Vol. 5, No. 7, 701-714, 1991.

Dyadic Green's functions in a planar stratified, arbitrarily magnetized linear plasma (T. M. Habashy, S. M. Ali, J. A. Kong, and M. D. Grossi), *Radio Science,* Vol. 26, No. 3, 701–716, May–June, 1991.

Current distribution, resistance, and inductance for superconducting strip transmission lines (D. M. Sheen, S. M. Ali, D. E. Oates, R. S. Withers, and J. A. Kong), *IEEE Transactions on Applied Superconductivity,* Vol. 1, No. 2, 108–115, June, 1991.

Resonant frequencies of stacked circular microstrip antennas (A. N. Tulintseff, S. M. Ali, and J. A. Kong), *IEEE AP-S International Symposium and URSI Radio Science Meeting,* San Jose, California, June 26–30, 1989.

Probe excitation of a center-fed circular microstrip antenna employing a stratified medium formulation (S. M. Ali, T. M. Habashy, and J. A. Kong), *IEEE AP-S International Symposium and URSI Radio Science Meeting,* San Jose, California, June 26–30, 1989.

Probe excitation of a center-fed circular microstrip antenna employing the Weber Transform (T. M. Habashy, S. M. Ali, and J. A. Kong), *IEEE AP-S International Symposium and URSI Radio Science Meeting,* San Jose, California, June 26–30, 1989.

Input impedance and radiation fields of a probe-fed stacked circular microstrip antenna, (A. N. Tulintseff, S. M. Ali, and J. A. Kong), *Progress in Electromagnetics Research Symposium,* 508-509 ston, Massachusetts, July 25–26, 1989.

Analysis of microstri ontinuities on anisotropic substrates, (J. Xia, S. M. Ali, and J. A. Kong), *Progress i. lectromagnetics Research Symposium,* 502-503, Boston, Massachusetts, July 25–26, 1989.

Analysis of dielectric strip waveguides using integral equation formulation, (J. F. Kiang, S. M. Ali, and J. A. Kong), *Progress in Electromagnetics Research Symposium,* 109-110, Boston, Massachusetts, July 25–26, 1989.

Input impedance of a circular microstrip antenna fed by an eccentric probe, (S. M. Ali, T. M. Habashy, and J. A. Kong), *Progress in Electromagnetics Research Symposium,* Boston, Massachusetts, 506-507, July 25–26, 1989.

Finite difference time domain techniques for two dimensional triangular grids, (C. F. Lee, R. T. Shin, J. A. Kong, and B. J. McCartin), *Progress in Electromagnetics Research Symposium,* 189-190, Boston, Massachusetts, July 25–26, 1989.

Absorbing boundary conditions on circular and elliptic boundaries, (C. F. Lee, R. T. Shin, J. A. Kong, and B. J. McCartin), *Progress in Electromagnetics Research Symposium,* 317-318, Boston, Massachusetts, July 25–26, 1989.

A new finite-difference time-domain grid model for microstrip problems in anisotropic media, (C. W. Lam, S. M. Ali, and J. A. Kong), *Progress in Electromagnetics Research Symposium,* 305-306, Boston, Massachusetts, July 25–26, 1989.

Analysis of multiport rectangular microstrip structures using a three dimensional finite difference time domain technique, (D. M. Sheen, S. M. Ali, M. D. Abouzahra, and J. A. Kong), *Progress in Electromagnetics Research Symposium,* 504-505, Boston, Massachusetts, July 25–26, 1989.

The frequency-dependent resistance of conductors with arbitrary cross-section, (M. J. Tsuk and J. A. Kong), *Progress in Electromagnetics Research Symposium,* 251-252, Boston, Massachusetts, July 25–26, 1989.

Transient analysis of frequency-dependent transmission lines with nonlinear terminations, (Q. Gu, Y. E. Yang and J. A. Kong), *Progress in Electromagnetics Research Symposium,* 239-240, Boston, Massachusetts, July 25–26, 1989.

Transient analysis of capacitively loaded VLSI off-chip interconnections, (Y. E. Yang and J. A. Kong), *Progress in Electromagnetics Research Symposium,* 241-242, Boston, Massachusetts, July 25–26, 1989.

Inversion of permittivity and conductivity profiles employing transverse-magnetic polarized monochromatic data (T. M. Habashy, M. Moldoveanu, and J. A. Kong), *SPIE's 1990 International Symposium on Optical and Optoelectronic Applied Science and Engineering,* San Diego, California, July 8–13, 1990.

Electro-magnetic calculation of soft X-ray diffraction from nanometer-scale gold structures (M. L. Schattenburg, K. Li, R. T. Shin, J. A. Kong, and H. I. Smith), submitted to *The 35th International Symposium on Electron, Ion, and Photon Beams,* Seattle, Washington, May 28–31, 1991.

Electromagnetic calculation of soft x-ray diffraction from 01.μm-scale gold structures (M. L. Schatenburg, K. Li, R. T. Shin, J. A. Kong, D. B. Olster, and H. I. Smith), *Journal of Vacuum Science and Technology* as part of the proceedings of *The 35th International Symposium on Electron, Ion, and Photon Beams,* (paper E84), Seattle, Washington, May 28–31, 1991.

Journal of Electromagnetic Waves and Applications, Vol. 4, No. 10, 1005–1021, 1990

The Propagation Characteristics of Signal Lines with Crossing Strips in Multilayered Anisotropic Media

C. W. Lam, S. M. Ali, and J. A. Kong

Department of Electrical Engineering and Computer Science
and Research Laboratory of Electronics
Massachusetts Institute of Technology
Cambridge, MA 02139, USA

Abstract— In this paper, full modal analysis is used to study the dispersion characteristics of microstrip lines periodically loaded with crossing strips in a stratified uniaxially anisotropic medium. Dyadic Green's functions in the spectral domain for the multilayered medium in conjunction with the vector Fourier transform (VFT) are used to formulate a coupled set of vector integral equations for the current distribution on the signal line and the crossing strips. Galerkin's procedure is applied to derive the eigenvalue equation for the propagation constant. The effect of anisotropy for both open and shielded structures on the stopband properties is investigated.

I. INTRODUCTION

In compact modules of high performance computers, signal transmission lines between integrated circuit chips are embedded in multilayered dielectric media. These signal lines are usually placed in different layers and run perpendicular to each other. The interaction between the orthogonal crossing lines and the signal line affects its propagation characteristics and may cause considerable signal distortion.

The interaction of a pair of crossing lines in an isotropic medium has been studied using a time-domain approach [1], where coupling is described qualitatively. This method becomes computationally expensive when the number of crossing lines increases. With many identical crossing strips uniformly distributed above the signal line, the transmission properties are characterized by stopbands due to the periodicity of the structure. Periodic structures have been investigated using frequency-domain methods. In [2], periodically nonuniform microstrip lines in an enclosure are analyzed on the basis of a numerical field calculation. A technique based on the network-analytical formulism of electromagnetic fields has been used to analyze striplines and finlines with periodic stubs [3]. The propagation characteristics of waves along a periodic array of parallel signal lines in a multilayered isotropic structure in the presence of a periodically perforated ground plane is studied in [4] and that in a mesh-plane environment is studied in [5]. More recently, the effect of the geometrical properties on the propagation characteristics of strip lines with periodic crossing strips embedded in a shielded one-layer isotropic medium have been investigated [6].

In this paper, both open and closed multilayered uniaxially anisotropic structures are considered. A full-wave analysis is used to study the propagation characteristics of a microstrip line in the presence of crossing strips. The signal line and the crossing strips are assumed to be located in two arbitrary layers of a stratified uniaxially anisotropic medium. An integral equation formulation using dyadic Green's functions in the periodically loaded structure is derived. Galerkin's method is then used to obtain the eigenvalue equation for the propagation constant. The effects of anisotropy on the stopband properties are investigated. Numerical results for open and shielded three-layer uniaxially anisotropic media are presented.

II. FORMULATION OF THE PROBLEM

In this section, we present a dyadic Green's function formulation of the problem shown in Fig. 1(a) where the microstrip line and the crossing strips are placed at two different interfaces of a uniaxially anisotropic multilayered medium. The crossing strips are assumed to be placed in a layer (i) and the signal line to be in a layer (j). The crossing strips are considered to be periodic with period p as shown in Fig. 1(b). In general, the permittivity and permeability tensors of an arbitrary layer (l) are assumed to be given by

$$\bar{\bar{\epsilon}}_l = \begin{pmatrix} \epsilon_l & 0 & 0 \\ 0 & \epsilon_l & 0 \\ 0 & 0 & \epsilon_{lz} \end{pmatrix} \tag{1}$$

and

$$\bar{\bar{\mu}}_l = \begin{pmatrix} \mu_l & 0 & 0 \\ 0 & \mu_l & 0 \\ 0 & 0 & \mu_{lz} \end{pmatrix} \tag{2}$$

where $l = 0, 1, 2, \ldots, n, \ldots, t$.

For the stratified medium, the electric fields in layers (i) and (j) due to current distributions $\bar{J}_i(\bar{r}')$ and $\bar{J}_j(\bar{r}')$ may be expressed as

$$\bar{E}_i(\bar{r}) = i\omega \iiint_V dV' \, \bar{\bar{G}}_{ii}(\bar{r}, \bar{r}') \cdot \bar{J}_i(\bar{r}') + i\omega \iiint_V dV' \, \bar{\bar{G}}_{ij}(\bar{r}, \bar{r}') \cdot \bar{J}_j(\bar{r}') \tag{3a}$$

$$\bar{E}_j(\bar{r}) = i\omega \iiint_V dV' \, \bar{\bar{G}}_{ji}(\bar{r}, \bar{r}') \cdot \bar{J}_i(\bar{r}') + i\omega \iiint_V dV' \, \bar{\bar{G}}_{jj}(\bar{r}, \bar{r}') \cdot \bar{J}_j(\bar{r}') \tag{3a}$$

where $\bar{\bar{G}}_{lm}(\bar{r}, \bar{r}')$ is the dyadic Green's function in layer (l) due to current sources in layer (m).

For the multilayered structure shown in Fig. 1(a), the current distributions on the conducting strips are assumed to be surface currents lying on planes transverse to z. Thus, if we are interested in the transverse electric fields $\bar{E}_i^{(s)}$ and $\bar{E}_j^{(s)}$ in layers (i) and (j), respectively, we can write

$$\bar{E}_i^{(s)}(\bar{r}) = \bar{E}_{ii}^{(s)}(\bar{r}) + \bar{E}_{ij}^{(s)}(\bar{r}) \tag{4a}$$

$$\bar{E}_j^{(s)}(\bar{r}) = \bar{E}_{ji}^{(s)}(\bar{r}) + \bar{E}_{jj}^{(s)}(\bar{r}) \tag{4b}$$

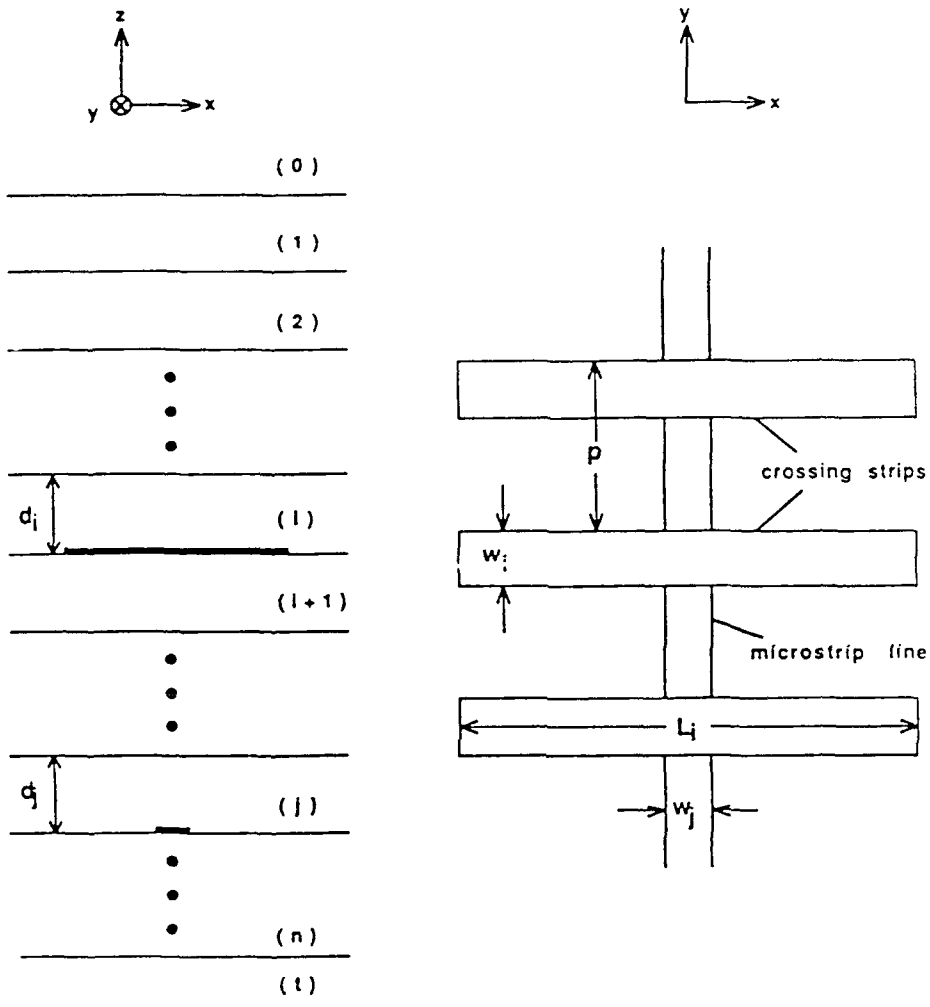

Figure 1. Geometrical configuration of a signal line in layer j loaded with crossing strips in layer i.

where $\overline{E}_{lm}^{(s)}$ is the transverse electric field in layer (l) due to current sources in layer (m), and is given by

$$\overline{E}_{lm}^{(s)}(\bar{r}) = i\omega \iiint_V dV' \overline{\overline{G}}_{lm}^{(s)}(\bar{r},\bar{r}') \cdot \overline{K}_m(\bar{r}') \tag{5}$$

$\overline{K}_m(\bar{r}')$ is the surface current distribution in layer (m), and $\overline{\overline{G}}_{lm}^{(s)}(\bar{r},\bar{r}')$ is the (2×2) transverse part of the dyadic Green's function $\overline{\overline{G}}_{lm}(\bar{r},\bar{r}')$.

Since the structure is assumed to be periodic in the y-direction, the electric field

$\overline{E}_l^{(s)}$ and the surface currents $\overline{K}_m$ can be expressed using the Floquet harmonic representation in the y-direction. In this case we can get

$$\overline{E}_{lm}^{(s)}(\bar{r}) = i\omega \int_{-\infty}^{\infty} dx' \int_{-p/2}^{p/2} dy' \, \overline{\overline{G}}_{lm}^{(s)}(\bar{r}, \bar{r}') \cdot \overline{K}_m(\bar{r}') \tag{6a}$$

where $l = i, j$, and

$$\overline{\overline{G}}_{lm}^{(s)}(\bar{r}, \bar{r}') = \frac{2\pi}{p} \sum_{n=-\infty}^{\infty} \int_{-\infty}^{\infty} dk_x \, e^{i\bar{k}_{sn}\cdot(\bar{r}_s - \bar{r}_s')} \overline{\overline{g}}_{lm}^{(s)}(\bar{k}_{sn}; z, z') \tag{6b}$$

$$\bar{r}_s = \hat{x}x + \hat{y}y, \quad \bar{k}_{sn} = \hat{x}k_x + \hat{y}\beta_n, \quad \beta_n = \beta_0 + \frac{2n\pi}{p}$$

Here p is the period, β_0 is the propagation constant of the dominant harmonic in the Floquet representation, and $\overline{\overline{g}}_{lm}^{(s)}(\bar{k}_{sn}; z, z')$ is the spectral dyadic Green's function.

Using the explicit expressions for the dyadic Green's functions $\overline{\overline{G}}_{ii}^{(s)}$, $\overline{\overline{G}}_{ij}^{(s)}$, $\overline{\overline{G}}_{ji}^{(s)}$ and $\overline{\overline{G}}_{jj}^{(s)}$ [7], the transverse electric fields on the surface of the conducting strips in layer (i) due to the currents in layer (j) can be expressed in the following form

$$\overline{E}_{ij}^{(s)}(\bar{r}_s) = -\frac{\pi}{p} \sum_{n=-\infty}^{\infty} \int_{-\infty}^{\infty} dk_x \, \overline{\overline{F}}(\bar{k}_{sn}, \bar{r}_s) \cdot \overline{\overline{\xi}}_{ij}(\bar{k}_{sn}) \cdot \tilde{\overline{K}}_j(\bar{k}_{sn}) \tag{7}$$

where $\overline{\overline{F}}(\bar{k}_{sn}, \bar{r}_s)$ is the kernel of the vector Fourier transform (VFT) given by [8]

$$\overline{\overline{F}}(\bar{k}_{sn}, \bar{r}_s) = \frac{1}{k_{sn}} \begin{bmatrix} k_x & \beta_n \\ \beta_n & -k_x \end{bmatrix} e^{i\bar{k}_{sn}\cdot\bar{r}_s} \tag{8}$$

and $\tilde{\overline{K}}_j(\bar{k}_{sn})$ is the vector Fourier transform of the surface current $\overline{K}_j(\bar{r}_s')$. It is given by

$$\tilde{\overline{K}}_j(\bar{k}_{sn}) = \frac{1}{(2\pi)^2} \iint_{-\infty}^{\infty} d\bar{r}_s' \, \overline{\overline{F}}(\bar{k}_{sn}, -\bar{r}_s') \cdot \overline{K}_j(\bar{r}_s') \tag{9}$$

The matrix $\overline{\overline{\xi}}_{ij}(\bar{k}_{sn})$ is given by

$$\overline{\overline{\xi}}_{ij}(\bar{k}_{sn}) = \begin{bmatrix} f_{ij}^{\mathrm{TM}} & 0 \\ 0 & f_{ij}^{\mathrm{TE}} \end{bmatrix} \tag{10}$$

whose elements for different i and j are given in Appendix A.

In the above, the transverse electric field expressions $\overline{E}_{lm}^{(s)}$ $(l, m = i, j)$ satisfy the boundary conditions at the dielectric interfaces of the layered medium. Applying the final boundary condition that the tangential electric field vanishes on the conducting strips, we can get the following set of dual vector integral equations for the currents on the metallic strips

$$\sum_{n=-\infty}^{\infty} \int_{-\infty}^{\infty} dk_x \, \overline{\overline{F}}(\bar{k}_{sn}, \bar{r}_s) \cdot \overline{\overline{\xi}}_{ii}(\bar{k}_{sn}) \cdot \overline{K}_i(\bar{k}_{sn})$$
$$+ \sum_{n=-\infty}^{\infty} \int_{-\infty}^{\infty} dk_x \, \overline{\overline{F}}(\bar{k}_{sn}, \bar{r}_s) \cdot \overline{\overline{\xi}}_{ij}(\bar{k}_{sn}) \cdot \overline{K}_j(\bar{k}_{sn}) = 0, \quad \bar{r}_s \in S_i \tag{11}$$

on the crossing strips, and

$$\sum_{n=-\infty}^{\infty}\int_{-\infty}^{\infty} dk_x\ \overline{\overline{F}}(\bar{k}_{sn},\bar{r}_s)\cdot\overline{\overline{\xi}}_{ji}(\bar{k}_{sn})\cdot\overline{K}_i(\bar{k}_{sn})$$
$$+\sum_{n=-\infty}^{\infty}\int_{-\infty}^{\infty} dk_x\ \overline{\overline{F}}(\bar{k}_{sn},\bar{r}_s)\cdot\overline{\overline{\xi}}_{jj}(\bar{k}_{sn})\cdot\overline{K}_j(\bar{k}_{sn})=0,\quad \bar{r}_s\in S_j \tag{12}$$

on the signal line.

The next step is to solve this coupled set of vector integral equations to find the dispersion relation for the signal line in the presence of the crossing strips.

III. GALERKIN'S METHOD AND THE EIGENVALUE EQUATION

The formulation up to this stage is exact. We now solve the set of vector integral equations (11) and (12) by using Galerkin's method. The unknown current distributions on the crossing strips $\overline{K}_i(\bar{r}_s)$ and on the signal line $\overline{K}_j(\bar{r}_s)$ are expanded in terms of the appropriate vector basis functions as follows:

$$\overline{K}_i(x,y)=\sum_{m=1}^{M}\sum_{r=1}^{R}\overline{\overline{\Phi}}_{mr}(x,y)\cdot\overline{A}_{mr} \tag{13}$$

$$\overline{K}_j(x,y)=\sum_{k=1}^{K}\sum_{q=-Q_1}^{Q_2}\overline{\overline{\Psi}}_k(x)e^{i\beta_q y}\cdot\overline{B}_{kq} \tag{14}$$

where $\overline{K}_i(x,y)$ and $\overline{K}_j(x,y)$ are the surface currents on the crossing strips and the signal line, respectively, $\overline{\overline{\Phi}}_{mr}$ and $\overline{\overline{\Psi}}_k e^{i\beta_q y}$ are the basis functions, $\overline{A}_{mr}$ and $\overline{B}_{kq}$ are the expansion coefficients.

Using (13) and (14), the vector Fourier transform (VFT) of the currents $\overline{K}_i(\bar{r}_s)$ and $\overline{K}_j(\bar{r}_s)$ are obtained as

$$\tilde{\overline{K}}_i(\bar{k}_{sn})=\sum_{m=1}^{M}\sum_{r=1}^{R}\overline{\overline{U}}_{(+)mr,n}(k_x,\beta)\cdot\overline{A}_{mr} \tag{15}$$

$$\tilde{\overline{K}}_j(\bar{k}_{sn})=\sum_{k=1}^{K}\sum_{q=-Q_1}^{Q_2}\overline{\overline{V}}_{(+)kq,n}(k_x,\beta)\cdot\overline{B}_{kq} \tag{16}$$

where

$$\overline{\overline{U}}_{(\pm)mr,n}(k_x,\beta)=\frac{1}{(2\pi)^2}\iint d\bar{r}_s\ \overline{\overline{F}}(\bar{k}_{sn},\mp\bar{r}_s)\cdot\overline{\overline{\Phi}}_{mr}(x,y) \tag{17}$$

and

$$\overline{\overline{V}}_{(\pm)kq,n}(k_x,\beta)=\frac{1}{(2\pi)^2}\iint d\bar{r}_s\ \overline{\overline{F}}(\bar{k}_{sn},\mp\bar{r}_s)\cdot\overline{\overline{\Psi}}_k(x)e^{\pm i\beta_q y} \tag{18}$$

Substituting (15) and (16) into (11) and (12), we obtain

$$\sum_{m=1}^{M}\sum_{r=1}^{R}\sum_{n=-\infty}^{\infty}\int_{-\infty}^{\infty} dk_x\ \overline{\overline{F}}(\bar{k}_{sn},\bar{r}_s)\cdot\overline{\overline{\xi}}_{ii}(\bar{k}_{sn})\cdot\overline{\overline{U}}_{(+)mr,n}(k_x,\beta)\cdot\overline{A}_{mr}$$

$$+\sum_{k=1}^{K}\sum_{q=-Q_1}^{Q_2}\sum_{n=-\infty}^{\infty}\int_{-\infty}^{\infty} dk_x\, \overline{\overline{F}}(\bar{k}_{sn},\bar{r}_s)\cdot\overline{\overline{\xi}}_{ij}(\bar{k}_{sn})\cdot\overline{\overline{V}}_{(+)kq,n}(k_x,\beta)\cdot\overline{B}_{kq}=0 \tag{19}$$

for $\bar{r}_s \in S_i$, and

$$\sum_{m=1}^{M}\sum_{r=1}^{R}\sum_{n=-\infty}^{\infty}\int_{-\infty}^{\infty} dk_x\, \overline{\overline{F}}(\bar{k}_{sn},\bar{r}_s)\cdot\overline{\overline{\xi}}_{ji}(\bar{k}_{sn})\cdot\overline{\overline{U}}_{(+)mr,n}(k_x,\beta)\cdot\overline{A}_{mr}$$
$$+\sum_{k=1}^{K}\sum_{q=-Q_1}^{Q_2}\sum_{n=-\infty}^{\infty}\int_{-\infty}^{\infty} dk_x\, \overline{\overline{F}}(\bar{k}_{sn},\bar{r}_s)\cdot\overline{\overline{\xi}}_{jj}(\bar{k}_{sn})\cdot\overline{\overline{V}}_{(+)kq,n}(k_x,\beta)\cdot\overline{B}_{kq}=0 \tag{20}$$

for $\bar{r}_s \in S_j$.

Multiplying (19) by $\overline{\overline{\Phi}}^{t}_{uv}(x,y)$ and integrating over the support of $\overline{K}_i(\bar{r}_s)$ for $u=1,2,\ldots,M$ and $v=1,2,\ldots,R$, we obtain

$$\sum_{m=1}^{M}\sum_{r=1}^{R}\sum_{n=-\infty}^{\infty}\int_{-\infty}^{\infty} dk_x\, \overline{\overline{U}}^{t}_{(-)uv,n}(k_x,\beta)\cdot\overline{\overline{\xi}}_{ii}(\bar{k}_{sn})\cdot\overline{\overline{U}}_{(+)mr,n}(k_x,\beta)\cdot\overline{A}_{mr}$$
$$+\sum_{k=1}^{K}\sum_{q=-Q_1}^{Q_2}\sum_{n=-\infty}^{\infty}\int_{-\infty}^{\infty} dk_x\, \overline{\overline{U}}^{t}_{(-)uv,n}(k_x,\beta)\cdot\overline{\overline{\xi}}_{ij}(\bar{k}_{sn})\cdot\overline{\overline{V}}_{(+)kq,n}(k_x,\beta)\cdot\overline{B}_{kq}=0 \tag{21}$$

Similarly, multiplying (20) by $\overline{\overline{\Psi}}^{t}_{s}(x)e^{-i\beta_t y}$ and integrating over the support of $\overline{K}_j(\bar{r}_s)$ for $s=1,2,\ldots,K$ and $t=-Q_1,\ldots,0,\ldots,Q_2$, we obtain

$$\sum_{m=1}^{M}\sum_{r=1}^{R}\sum_{n=-\infty}^{\infty}\int_{-\infty}^{\infty} dk_x\, \overline{\overline{V}}^{t}_{(-)st,n}(k_x,\beta)\cdot\overline{\overline{\xi}}_{ji}(\bar{k}_{sn})\cdot\overline{\overline{U}}_{(+)mr,n}(k_x,\beta)\cdot\overline{A}_{mr}$$
$$+\sum_{k=1}^{K}\sum_{q=-Q_1}^{Q_2}\sum_{n=-\infty}^{\infty}\int_{-\infty}^{\infty} dk_x\, \overline{\overline{V}}^{t}_{(-)st,n}(k_x,\beta)\cdot\overline{\overline{\xi}}_{jj}(\bar{k}_{sn})\cdot\overline{\overline{V}}_{(+)kq,n}(k_x,\beta)\cdot\overline{B}_{kq}=0 \tag{22}$$

Equations (21) and (22) constitute a system of $(S+T)$ linear algebraic equations with $S=MR$ and $T=K(Q_1+Q_2+1)$, and may be written in matrix form as

$$\overline{\overline{N}}\cdot\bar{c}=0 \tag{23a}$$

where

$$\overline{\overline{N}}=\begin{bmatrix}[N_{11}]_{S\times S} & [N_{12}]_{S\times T}\\ [N_{21}]_{T\times S} & [N_{22}]_{T\times T}\end{bmatrix} \tag{23b}$$

and

$$\bar{c}=\begin{bmatrix}[A_{mr}]_{S\times 1}\\ [B_{kq}]_{T\times 1}\end{bmatrix} \tag{23c}$$

Each element of the submatrices of $\overline{\overline{N}}$ is given by

$$[N_{11}]_{uv,mr} = \sum_{n=-\infty}^{\infty} \int_{-\infty}^{\infty} dk_x \, \overline{\overline{U}}'_{(-)_{uv,n}}(k_x,\beta) \cdot \overline{\overline{\xi}}_{ii}(\overline{k}_{sn}) \cdot \overline{\overline{U}}_{(+)_{mr,n}}(k_x,\beta) \tag{24a}$$

$$[N_{12}]_{uv,kq} = \sum_{n=-\infty}^{\infty} \int_{-\infty}^{\infty} dk_x \, \overline{\overline{U}}'_{(-)_{uv,n}}(k_x,\beta) \cdot \overline{\overline{\xi}}_{ij}(\overline{k}_{sn}) \cdot \overline{\overline{V}}_{(+)_{kq,n}}(k_x,\beta) \tag{24b}$$

$$[N_{21}]_{st,mr} = \sum_{n=-\infty}^{\infty} \int_{-\infty}^{\infty} dk_x \, \overline{\overline{V}}'_{(-)_{st,n}}(k_x,\beta) \cdot \overline{\overline{\xi}}_{ji}(\overline{k}_{sn}) \cdot \overline{\overline{U}}_{(+)_{mr,n}}(k_x,\beta) \tag{24c}$$

$$[N_{22}]_{st,kq} = \sum_{n=-\infty}^{\infty} \int_{-\infty}^{\infty} dk_x \, \overline{\overline{V}}'_{(-)_{st,n}}(k_x,\beta) \cdot \overline{\overline{\xi}}_{jj}(\overline{k}_{sn}) \cdot \overline{\overline{V}}_{(+)_{kq,n}}(k_x,\beta) \tag{24d}$$

For nontrivial solution to exist, the determinant of the coefficient matrix of (21) and (22) must be zero,

$$\det\left[\overline{\overline{N}}(\omega,\beta)\right] = 0 \tag{25}$$

This is the eigenvalue equation for the propagation constant β which describes the dispersion relation of the loaded microstrip line in the multilayered anisotropic medium.

The next step is to choose appropriate basis functions for the surface currents $\overline{K}_j(\overline{r}_s)$ and $\overline{K}_i(\overline{r}_s)$ on the signal line and the crossing strips, respectively. The expansion functions we use are

$$\overline{\overline{\Phi}}_{mr}(x,y) = \frac{p}{2\pi}\begin{bmatrix} P_m(x,L_i) & 0 \\ 0 & Q_m(x,L_i) \end{bmatrix}\begin{bmatrix} Q_r(y,w_i) & 0 \\ 0 & R_r(y,w_i) \end{bmatrix} \tag{26}$$

and

$$\overline{\overline{\Psi}}_k(x) = \frac{p}{2\pi}\begin{bmatrix} P_k(x,w_j) & 0 \\ 0 & Q_k(x,w_j) \end{bmatrix} \tag{27}$$

where

$$P_n(\alpha,\gamma) = \frac{1}{\gamma}\sin\frac{2n\pi\alpha}{\gamma} \tag{28}$$

$$Q_n(\alpha,\gamma) = \frac{\cos\frac{2(n-1)\pi\alpha}{\gamma}}{\sqrt{(\frac{\gamma}{2})^2-\alpha^2}} \tag{29}$$

$$R_n(\alpha,\gamma) = \frac{1}{\gamma}\sin\frac{n\pi(\alpha+\gamma/2)}{\gamma} \tag{30}$$

w_i and w_j are the widths of the crossing strips and the signal line, respectively, and L_i is the length of the crossing strips. When choosing the basis functions for the surface currents, it should be borne in mind that the current cannot have

a normal component to the strip edges. Futhermore, the edge condition for the parallel component should be considered. By substituting (26) and (27) into (17) and (18), respectively, we can get

$$\overline{\overline{U}}_{(\pm)mr,n}(k_x,\beta) = \frac{p}{(2\pi)^3 k_{sn}} \begin{bmatrix} \pm X_m(k_x,L_i) & 0 \\ 0 & Y_m(k_x,L_i) \end{bmatrix} \cdot \begin{bmatrix} Y_r(\beta_n,w_i) & 0 \\ 0 & Z_{(\pm)_r}(\beta_n,w_i) \end{bmatrix} \tag{31}$$

and

$$\overline{\overline{V}}_{(\pm)kq,n}(k_x,\beta) = \frac{p\delta_{qn}}{(2\pi)^3 k_{sn}} \begin{bmatrix} \pm X_k(k_x,w_j) & 0 \\ 0 & Y_k(k_x,w_j) \end{bmatrix} \tag{32}$$

where

$$X_n(\alpha,\gamma) = i(-1)^n \frac{4n\pi \sin\frac{\alpha\gamma}{2}}{4n^2\pi^2 - \alpha^2\gamma^2} \tag{33}$$

$$Y_n(\alpha,\gamma) = \frac{\pi}{2}\Big\{ J_0[(n-1)\pi + \frac{\alpha\gamma}{2}] + J_0[(n-1)\pi - \frac{\alpha\gamma}{2}]\Big\} \tag{34}$$

$$Z_{(\pm)_n}(\alpha,\gamma) = \frac{-i}{n^2\pi^2 - \alpha^2\gamma^2}\Big[e^{\frac{in\pi}{2}}(n\pi \pm \alpha\gamma)\sin(\frac{n\pi}{2} \mp \frac{\alpha\gamma}{2}) - e^{\frac{-in\pi}{2}}(n\pi \mp \alpha\gamma)\sin(\frac{n\pi}{2} \pm \frac{\alpha\gamma}{2})\Big] \tag{35}$$

Equations (31) and (32) are then substituted into the determinantal equation (25) for the calculation of the dispersion characteristics.

IV. NUMERICAL TREATMENT AND RESULTS

In this section, we present numerical results for open and closed three-layer structures with the crossing strips and the signal line embedded in two different layers as shown in Figs. 2(a) and (b). In numerical calculation, the infinite series of Floquet modes and the basis functions are truncated. The ranges of indices in (24) are chosen as: $-10 \le n \le 9$, $k = 1$, $-1 \le q \le 0$, $1 \le m \le 3$, $r = 1$, $s = 1$, $-1 \le t \le 0$, $1 \le u \le 3$, and $v = 1$. It can be seen that each element in the coefficient matrix can be reduced to a sum of TE and TM terms, a summation over n Floquet modes, and an integral over k_x. Due to the symmetrical properties of the Green's function, the basis functions and the test functions, all the integrands are found to be even functions of k_x. So the integration path can be reduced to an integral from 0 to ∞. In numerical computation, the path of integration in the complex k_x plane is deformed to avoid the singularities on the real axis [9].

In the following calculations, the parameters used for Fig. 2 are: $d_1 = d_2 = d_3 = 0.2$ mm, $p = 0.5$ mm, $w_1 = w_2 = 0.125$ mm, $L_1 = 1.7$ mm, and $\mu_j = \mu_{jz} = \mu_0$. Since the crossing strip length is much longer than the signal line width, the current near the crossing strip edges is relatively small so that the edge condition in the basis functions can be neglected.

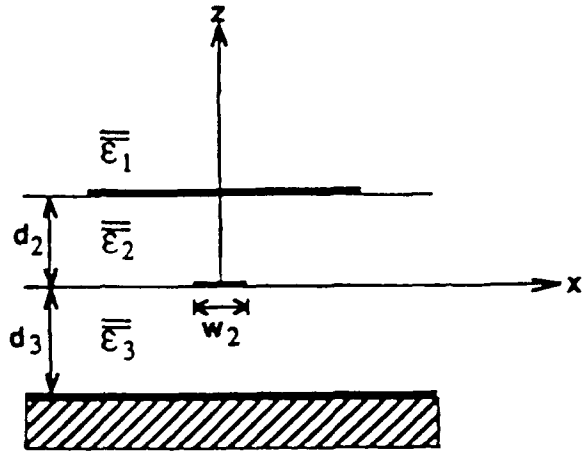

(a)

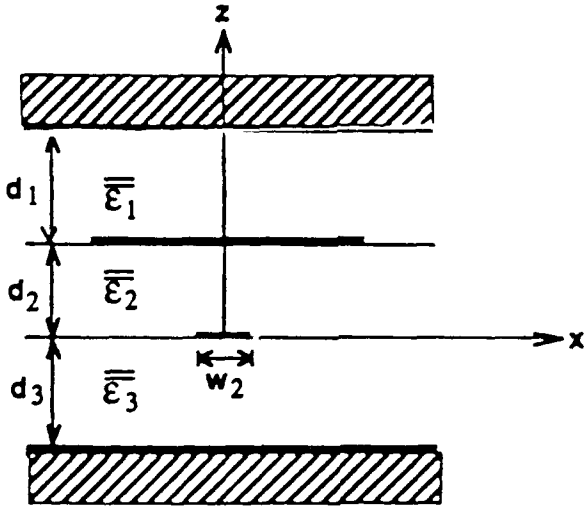

(b)

Figure 2. (a) Cross section of an open structure. (b) Cross section of a closed structure.

Figure 3 shows the dispersion characteristics of a closed microstrip line loaded with periodic crossing strips (Fig. 2(b)). The result shows that the first stopband appears due to the coupling between the Floquet modes $n = 0$ and $n = -1$ of the fundamental mode of the signal line. The upper and lower bounds of the stopband is denoted by ω_U and ω_L, respectively. At higher frequencies, higher order stopbands are encountered because of the interaction with the higher order modes of the signal line. However, we concentrate only on the first stopband which is in the region of practical interest.

In Fig. 4, the dispersion characteristics of an open and a shielded structure are plotted in solid and dashed lines, respectively. It can be seen that both the stopband position and width are close to those of each other. This is because the fields are mostly confined under the first layer where the coupling between signal line and crossing strips takes place. So removing the top conducting plate does not affect the stopband properties much in this case. This point is illustrated in Figs. 5(a) and (b) which shows the effect of changing d_1 on the stopband position and width, respectively. In the following, we are going to investigate the effect of anisotropy in the second and the third layer of a closed structure. It is believed that similar effects can be observed in an open structure.

The plot in Fig. 6 shows the effect of the anisotropy ratio ($AR = \epsilon_2/\epsilon_{2z}$) of the second layer on the stopband position and the stopband width. The center frequency of the stopband is not much affected by the anisotropy. However, the stopband width is quite sensitive to it. The width increases with $1/AR$. For fixed ϵ_2, it corresponds to an increase of ϵ_{2z}, which enhances coupling between the signal line and the crossing strips, resulting in the rise of stopband width. For $1/AR > 1$, it is found in the dispersion diagram that a high order stopband starts to merge with the first order stopband, resulting in a large stopband width. Fig. 6 is thus plotted up to that value only.

In Fig. 7, we investigate the effect of anisotropy in the third layer on the stopband properties. As we have expected, the stopband width is not so sensitive to the anisotropy in the third layer as it is in the second layer where coupling occurs. The change of stopband position with the anisotropy is close to that in the second layer. Both are due to the change of the dispersion characteristics of the signal line which results in the lowering of the intersecting point of the Floquet modes $n = 0$ and $n = -1$. A high order stopband is encountered for $1/AR > 1$.

Various combinations of substrate materials have been used to minimize the stopband width for the closed structure (Fig. 2(b)). The results are summarized in the following table:

Case	layer 1	layer 2	layer 3	$(k_0p/\pi)_c$	$\Delta(k_0p/\pi)$
1	$10\epsilon_0$	sapph.	$10\epsilon_0$	0.3093	5.93E-3
2	$10\epsilon_0$	$10\epsilon_0$	$10\epsilon_0$	0.3144	3.67E-3
3	$10\epsilon_0$	Eps-10	$10\epsilon_0$	0.3061	3.40E-3
4	$2.3\epsilon_0$	$10\epsilon_0$	$10\epsilon_0$	0.3194	0.80E-3
5	$2.3\epsilon_0$	$10\epsilon_0$	sapph.	0.3054	0.53E-3
6	ϵ_0	$10\epsilon_0$	sapph.	0.3058	0.87E-3

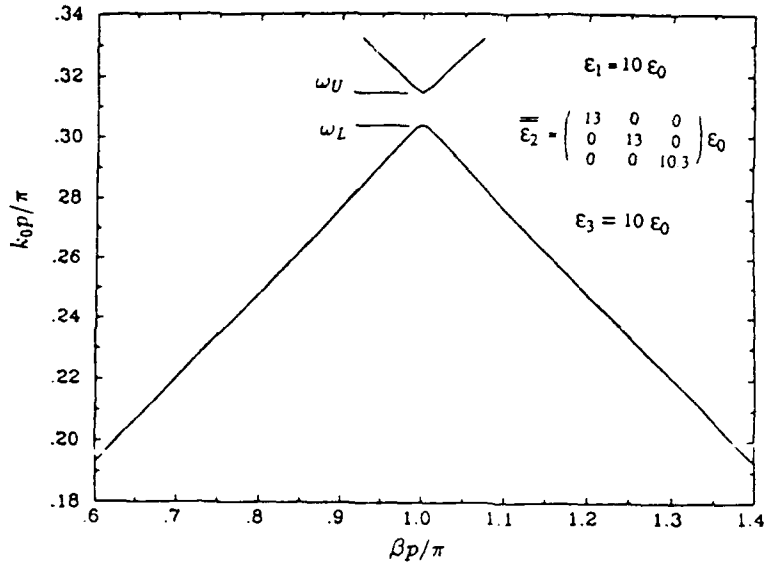

Figure 3. The dispersion characteristics of a closed structure with $\epsilon_1 = \epsilon_{1z} = 10\epsilon_0$, $\epsilon_2 = 13\epsilon_0$, $\epsilon_{2z} = 10.3\epsilon_0$, and $\epsilon_3 = \epsilon_{3z} = 10\epsilon_0$.

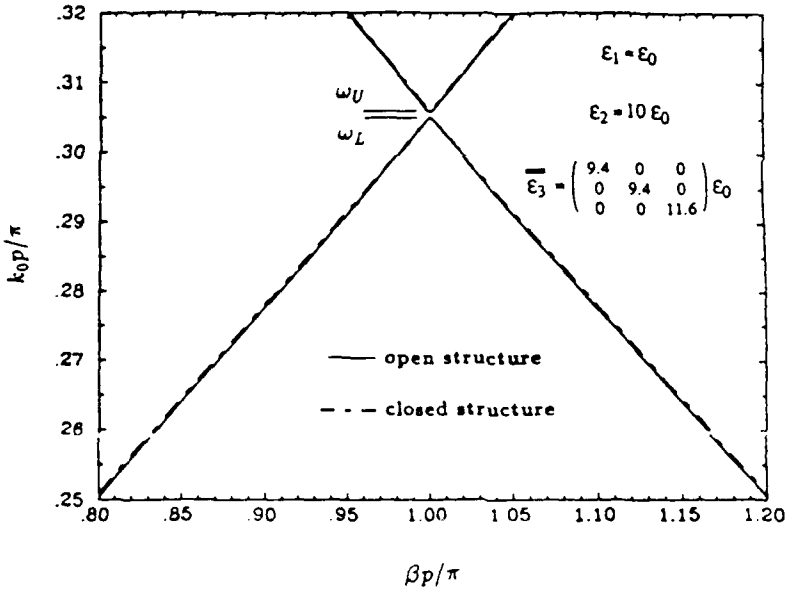

Figure 4. The dispersion characteristics of an open structure with $\epsilon_1 = \epsilon_{1z} = \epsilon_0$, $\epsilon_2 = \epsilon_{2z} = 10\epsilon_0$, $\epsilon_3 = 9.4\epsilon_0$, and $\epsilon_{3z} = 11.6\epsilon_0$.

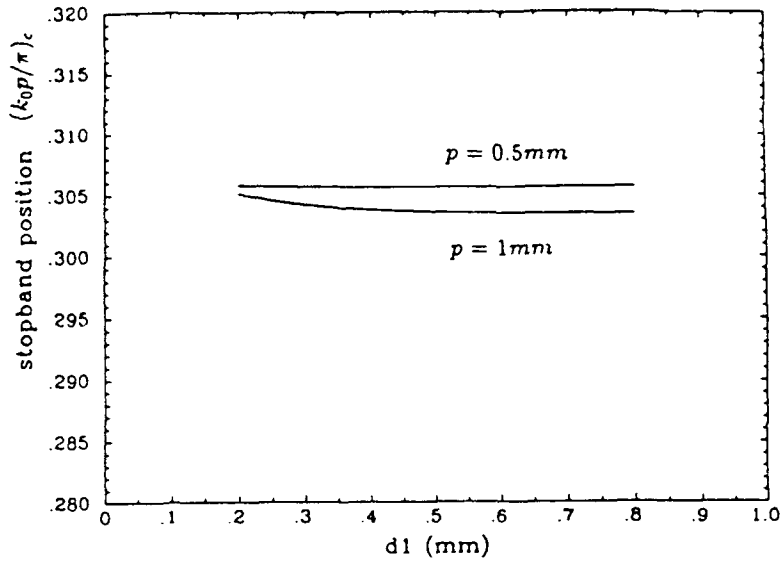

(a)

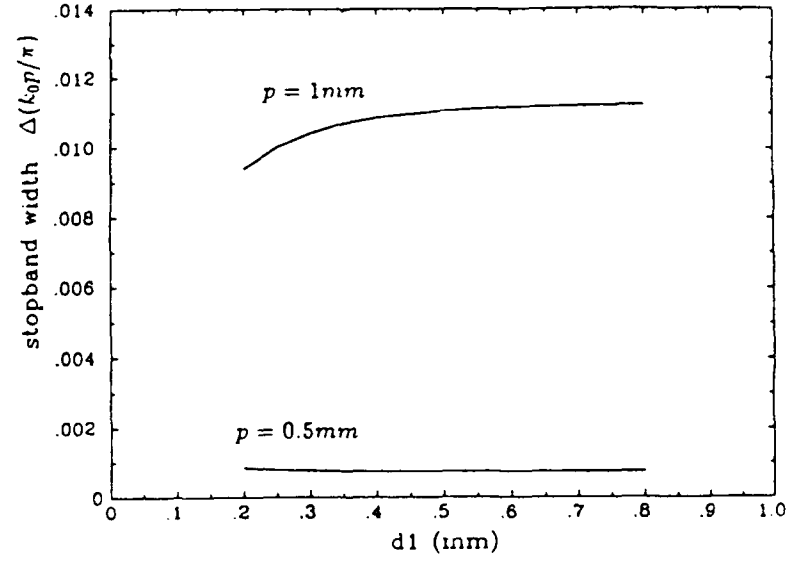

(b)

Figure 5. The effect of d_1 on the stopband: (a) position and (b) width. $\epsilon_1 = \epsilon_{1z} = \epsilon_0$, $\epsilon_2 = \epsilon_{2z} = 10\epsilon_0$, $\epsilon_3 = 9.4\epsilon_0$, and $\epsilon_{3z} = 11.6\epsilon_0$.

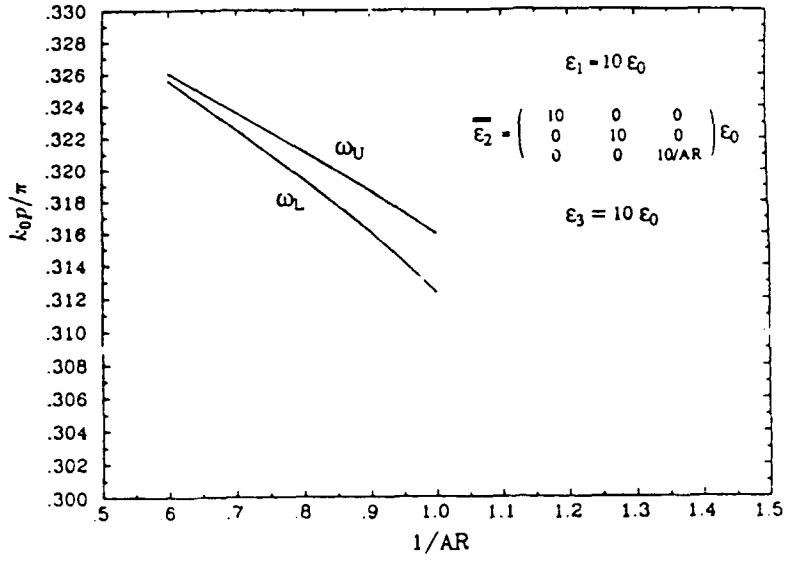

Figure 6. The effect of AR in the second layer on the upper and lower bounds of the stopband, $\epsilon_1 = \epsilon_{1z} = 10\epsilon_0$, $\epsilon_2 = 10\epsilon_0$, $\epsilon_3 = \epsilon_{3z} = 10\epsilon_0$.

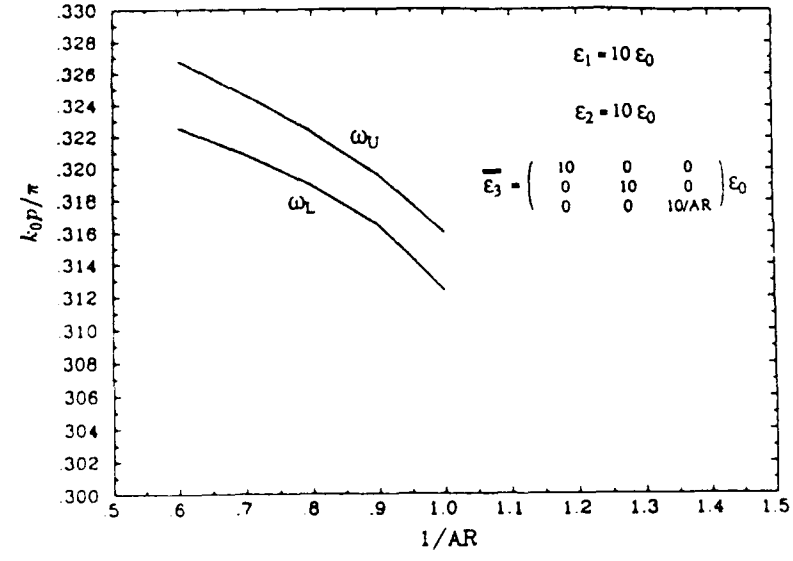

Figure 7. The effect of AR in the third layer on the upper and lower bounds of the stopband, $\epsilon_1 = \epsilon_{1z} = 10\epsilon_0$, $\epsilon_2 = \epsilon_{3z} = 10\epsilon_0$, $\epsilon_3 = 10\epsilon_0$.

where $(k_0 p/\pi)_c$ is the normalized center frequency of the stopband and $\Delta(k_0 p/\pi)$ is the normalized stopband width.

The two types of anisotropic substrates considered are Epsilam-10 ($\epsilon = 13\epsilon_0$, $\epsilon_z = 10.3\epsilon_0$) and sapphire ($\epsilon = 9.4\epsilon_0$, $\epsilon_z = 11.6\epsilon_0$). Comparison shows that the fifth case has the smallest stopband width. In fact, the stopband width is quite sensitive to the separation of the crossing strips due to the resonance effect [6]. Once the periodicity p is fixed, the stopband width can be minimized by a proper choice of substrate material.

V. CONCLUSIONS

A dyadic Green's function formulation for the analysis of open and closed microstrip lines in the presence of periodic crossing strips in a stratified uniaxially anisotropic medium is presented. The dispersion characteristics for a three-layer structure is studied. Numerical results illustrate the relationship between the stopband properties and the material parameters. The effect of anisotropy has also been investigated. It is found that the crossing strip separation and the anisotropy in the second layer are important factors affecting the stopband width. To achieve small stopband width, careful choice of anisotropy must be made to avoid the lowering of the high order stopband. It should also be noted that by the proper choice of substrate materials, the stopband width can be much reduced for fixed crossing strip separation.

APPENDIX A

Using the dyadic Green's function formulation [7], the elements of $\bar{\bar{\xi}}_{ij}(\bar{k}_{sn})$ can be obtained as follows:

For $i = j$, where the source and observation points are in the same layer, we have

$$f_{jj}^{\mathrm{TE}} = \frac{\omega\mu_j}{k_{jz}^{(h)}} \frac{1}{\left(1 - R_{\cup j}^{\mathrm{TE}} R_{\cap j}^{\mathrm{TE}} e^{2ik_{jz}^{(h)} d_j}\right)} \left(1 + R_{\cup j}^{\mathrm{TE}} e^{2ik_{jz}^{(h)} d_j}\right) \left(1 + R_{\cap j}^{\mathrm{TE}}\right) \tag{A1}$$

$$f_{jj}^{\mathrm{TM}} = \frac{1}{\omega\epsilon_j} k_{jz}^{(e)} \frac{1}{\left(1 - R_{\cup j}^{\mathrm{TM}} R_{\cap j}^{\mathrm{TM}} e^{2ik_{jz}^{(e)} d_j}\right)} \left(1 - R_{\cup j}^{\mathrm{TM}} e^{2ik_{jz}^{(e)} d_j}\right) \left(1 - R_{\cap j}^{\mathrm{TM}}\right) \tag{A2}$$

and for $j > i$, where the source is in layer (j) and observation point is in layer (i), we have

$$f_{ij}^{\mathrm{TE}} = \frac{\omega\mu_j}{k_{jz}^{(h)}} \frac{X_{\cup i,j}^{\mathrm{TE}}}{\left(1 - R_{\cap j}^{\mathrm{TE}} R_{\cup j}^{\mathrm{TE}} e^{2ik_{jz}^{(h)} d_j}\right)} e^{ik_{jz}^{(h)} d_j} \left(1 + R_{\cap j}^{\mathrm{TE}}\right) \left(1 + R_{\cup i}^{\mathrm{TE}} e^{2ik_{iz}^{(h)} d_i}\right) \tag{A3}$$

$$f_{ij}^{\mathrm{TM}} = \frac{1}{\omega\epsilon_j} k_{iz}^{(e)} \frac{k_j}{k_i} \frac{X_{\cup i,j}^{\mathrm{TM}}}{\left(1 - R_{\cap j}^{\mathrm{TM}} R_{\cup j}^{\mathrm{TM}} e^{2ik_{jz}^{(e)} d_j}\right)} e^{ik_{jz}^{(e)} d_j} (1 - R_{\cap j}^{\mathrm{TM}}) \left(1 - R_{\cup i}^{\mathrm{TM}} e^{2ik_{iz}^{(e)} d_i}\right) \tag{A4}$$

where $X_{\cup i,j}^{\mathrm{TE}}$ and $X_{\cup i,j}^{\mathrm{TM}}$ are, respectively, the TE and TM upward transmission coefficients from layer (j) to layer (i), given by

$$X_{\cup l,m}^{\mathrm{TE}} = X_{\cup(l+1),m}^{\mathrm{TE}} e^{ik_{(l+1)z}^{(h)} d_{(l+1)}} \frac{\left(1 + R_{\cup(l+1)}^{\mathrm{TE}}\right)}{\left(1 + R_{\cup l}^{\mathrm{TE}} e^{2ik_{lz}^{(h)} d_l}\right)} \tag{A5}$$

$$X_{\cup l,m}^{\mathrm{TM}} = X_{\cup(l+1),m}^{\mathrm{TM}} \frac{k_l}{k_{lz}^{(e)}} \frac{k_{(l+1)z}^{(e)}}{k_{(l+1)}} e^{ik_{(l+1)z}^{(e)} d_{(l+1)}} \frac{\left(1 - R_{\cup(l+1)}^{\mathrm{TM}}\right)}{\left(1 - R_{\cup l}^{\mathrm{TM}} e^{2ik_{lz}^{(e)} d_l}\right)} \tag{A6}$$

for $l = (m-2), (m-3), \ldots, 0$, and for $l = (m-1)$, we have

$$X_{\cup(m-1),m}^{\mathrm{TE}} = \frac{\left(1 + R_{\cup m}^{\mathrm{TE}}\right)}{\left(1 + R_{\cup(m-1)}^{\mathrm{TE}} e^{2ik_{(m-1)z}^{(h)} d_{(m-1)}}\right)} \tag{A7}$$

$$X_{\cup(m-1),m}^{\mathrm{TM}} = \frac{k_l}{k_{lz}} \frac{k_{mz}}{k_m} \frac{\left(1 - R_{\cup m}^{\mathrm{TM}}\right)}{\left(1 - R_{\cup(m-1)}^{\mathrm{TM}} e^{2ik_{(m-1)z}^{(e)} d_{(m-1)}}\right)} \tag{A8}$$

and

$$k_{jz}^{(h)} = \sqrt{k_j^2 - \frac{\mu_j}{\mu_{jz}} k_s^2} \tag{A9}$$

$$k_{jz}^{(e)} = \sqrt{k_j^2 - \frac{\epsilon_j}{\epsilon_{jz}} k_s^2} \tag{A10}$$

$$k_j^2 = \omega^2 \epsilon_j \mu_j \tag{A11}$$

Using the symmetrical properties of the dyadic Green's function in the layered media, it can be shown that $f_{ji}^{\alpha} = f_{ij}^{\alpha}$, where α denotes TE or TM. In the above equations, the superscripts (h) and (e) denote TE and TM fields, respectively. $R_{\cap l}^{\alpha}$ and $R_{\cup l}^{\alpha}$ are, respectively, the Fresnel reflection coefficients at the lower and upper boundaries of layer (l) and can be determined recursively by the following relations

$$R_{\cap l}^{\alpha} = \frac{R_{l(l+1)}^{\alpha} + R_{\cap(l+1)}^{\alpha} e^{2ik_{(l+1)z}^{\alpha} d_{l+1}}}{1 + R_{l(l+1)}^{\alpha} R_{\cap(l+1)}^{\alpha} e^{2ik_{(l+1)z}^{\alpha} d_{l+1}}} \tag{A12}$$

where $l = 0, \ldots, (n-1)$ and $R_{\cap n}^{\alpha} = R_{nt}^{\alpha}$.

$$R^{\alpha}_{\cup l} = \frac{R^{\alpha}_{l(l-1)} + R^{\alpha}_{\cup(l-1)} e^{2ik^{\alpha}_{(l-1)z} d_{l-1}}}{1 + R^{\alpha}_{l(l-1)} R^{\alpha}_{\cup(l-1)} e^{2ik^{\alpha}_{(l-1)z} d_{l-1}}} \tag{A13}$$

where $l = 2, 3, \ldots, t$ and $R^{\alpha}_{\cup 1} = R^{\alpha}_{10}$. $R^{\alpha}_{l(l-1)}$ and $R^{\alpha}_{l(l+1)}$ are the Fresnel reflection coefficients across the interface between layers (l) and $(l+1)$.

ACKNOWLEDGMENTS

This work was supported by the NSF under Grant 8620029-ECS, by the Joint Services Electronics Program under Contract DAAL03-89-C-0001, by the RADC under Contract F19628-88-K-0013, by the ARO under Contract DAAL03-88-J-0057, and by the ONR under Contract N00014-90-J-1002.

The Editor thanks T. M. Habashy, J. F. Kiang, and one anonymous Reviewer for reviewing the paper.

REFERENCES

1. Koike, S., N. Yoshida, and I. Fukai, "Transient analysis of coupling between crossing lines in three-dimensional space," *IEEE Trans. Microwave Theory Tech.*, Vol. MTT-35, No. 1, 67–71, Jan. 1987.
2. Glandorf, F. J., and I. Wolff, "A spectral-domain analysis of periodically non-uniform microstrip lines," *IEEE Trans. Microwave Theory Tech.*, Vol. MTT-35, No. 3, 336–343, Mar. 1987.
3. Kitazawa, T., and R. Mittra, "An investigation of striplines and fin lines with periodic stubs," *IEEE Trans. Microwave Theory Tech.*, Vol. MTT-32, No. 7, 684–688, July 1984.
4. Chan, C. H., and R. Mittra, "The propagation characteristics of signal lines embedded in a multilayered structure in the presence of a periodically perforated ground plane," *IEEE Trans. Microwave Theory Tech.*, Vol. MTT-36, No. 6, 968–975, June 1988.
5. Rubin, B. J., "The propagation characteristics of signal lines in a mesh-plane environment," *IEEE Trans. Microwave Theory Tech.*, Vol. MTT-32, No. 5, 522–531, May 1984.
6. Kiang, J. F., S. M. Ali, and J. A. Kong, "Propagation properties of strip lines periodically loaded with crossing strips," *IEEE Trans. Microwave Theory Tech.*, Vol. MTT-37, No. 4, 776–786, Apr. 1989.
7. Ali, S. M., T. M. Habashy, and J. A. Kong, "Dyadic Green's functions for multilayered uniaxially anisotropic media," submitted for publication.
8. Chew, W. C., and T. M. Habashy, "The use of vector transforms in solving some electromagnetic scattering problems," *IEEE Trans. Antennas Propagat.*, Vol. AP-34, No. 7, 871–879, July 1986.
9. Fache, N., and D. De Zutter, "Rigorous full-wave space-domain solution for dispersive microstrip lines," *IEEE Trans. Microwave Theory Tech.*, Vol. MTT-36, No. 4, 731–737, Apr. 1988.

Cheung-Wei Lam was born in Hong Kong on March 5, 1965. He received the B.S. degree (1987) in electronics from Chinese University of Hong Kong. In 1989 he obtained his S.M. degree in electrical engineering from the Massachusetts Institute of Technology where he is currently a graduate research assistant working towards the Ph.D degree. His main research interests include full-wave analyses of microstrip structures on anisotropic substrates and application of the finite-difference time-domain method to microstrip problems.

Sami M. Ali was born in Egypt on December 7, 1938. He received the B.Sc. degree from the Military Technical College, Cairo, Egypt, in 1965, and the Ph.D. degree from the Technical University of Prague, Prague, Czechoslovakia, in 1975, both in electrical engineering. In 1975 he joined the Department of Electrical Engineering, Military Technical College, Cairo. He spent the 1981–1982 academic year as a visiting scientist at the Research Laboratory of Electronics, MIT, Cambridge, Massachusetts. In 1985, he became a Professor and head of the Basic Electrical Engineering Department, Military Technical College, Cairo, Egypt. Since 1987, he is a visiting scientist at the Research Laboratory of Electronics, MIT, Cambridge, Massachusetts. His current research interests deal with microwave integrated circuits and microstrip antenna applications. He is currently serving as a member of the International Advisory Board of the book series Progress in Electromagnetics Research, published by Elsevier.

J. A. Kong is Professor of Electrical Engineering and Chairman of Area IV on Energy and Electromagnetic Systems in the Department of Electrical Engineering and Computer Science at the Massachusetts Institute of Technology in Cambridge, Massachusetts. His research interest is in the field of electromagnetic wave theory and applications. He has published 6 books and over 200 refereed journal and conference papers, and is the Editor of the Wiley Series in Remote Sensing, and Chief Editor of the Elsevier book series of Progress In Electromagnetics Research (PIER).

Input Impedance of a Probe-Fed Stacked Circular Microstrip Antenna

Ann N. Tulintseff, Sami M. Ali, *Senior Member, IEEE,* and Jin Au Kong, *Fellow, IEEE*

Abstract—**The input impedance of a microstrip antenna consisting of two circular microstrip disks in a stacked configuration driven by a coaxial probe is investigated. A rigorous analysis is performed using a dyadic Green's function formulation where the mixed boundary value problem is reduced to a set of coupled vector integral equations using the vector Hankel transform. Galerkin's method is employed in the spectral domain where two sets of disk current expansions are used. One set is based on the complete set of orthogonal modes of the magnetic cavity, and the other employs Chebyshev polynomials with the proper edge condition for the disk currents. An additional term is added to the disk current expansion to properly model the current in the vicinity of the probe/disk junction. The input impedance of the stacked microstrip antenna including the probe self-impedance is calculated as a function of the layered parameters and the ratio of the two disk radii. Disk current distributions and radiation patterns are also presented. The calculated results are compared with experimental data and shown to be in good agreement.**

I. Introduction

CONVENTIONAL microstrip antennas, consisting of a single conducting patch on a grounded dielectric substrate, have received much attention in recent years [1] due to their many advantages, including low profile, light weight, and easy integration with printed circuits. However, due to their resonant behavior, they radiate efficiently only over a narrow band of frequencies, with bandwidths typically only a few percent [1]. While maintaining the advantages of conventional single patch microstrip antennas, microstrip antennas of stacked configurations, consisting of one or more conducting patches parasitically coupled to a driven patch, overcome the inherent narrow bandwidth limitation by introducing additional resonances in the frequency range of operation, achieving bandwidths up to 10–20%. In addition, stacked microstrip configurations have achieved higher gains and offer the possibility of dual frequency operation.

Experimental work with multilayered microstrip elements has been abundant [2]–[9]. However, to date, theoretical work has been relatively limited, where the study of resonant frequencies, modes and radiation patterns have been investigated [10]–[13]. Recently, the finite-difference time-domain technique was applied to stacked rectangular microstrip patch configurations [14]. There is little or no theoretical analysis of the input impedance of coaxial probe-fed stacked circular microstrip patches. However, the input impedance for conventional single-layer coaxial probe-fed microstrip antennas of circular, rectangular, annular ring, and elliptic geometries has been investigated by many authors [15]–[19]. The impedance parameters of two planar coupled microstrip patches have also been studied [19], [20].

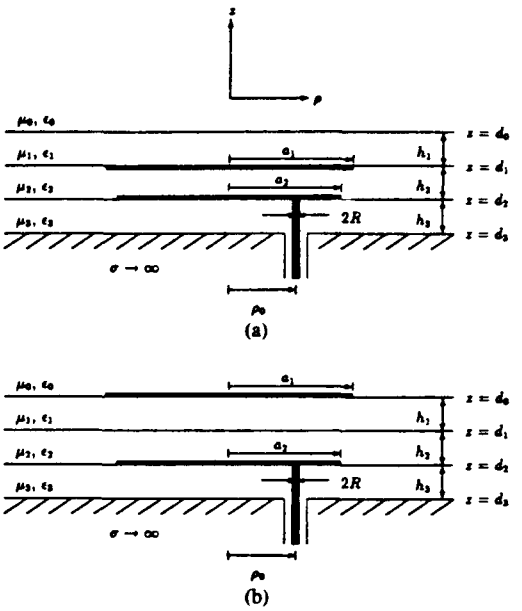

Fig. 1. Stacked microstrip antenna configurations.

In the calculation of the input impedance of probe-driven microstrip antennas on thin substrates, the effect of the probe results in an additional inductive component to the input impedance. This probe inductance has been accounted for by several authors through use of a simple formula [19], [21]. In more rigorous methods to include the effects of the probe, an "attachment mode" in the disk current expansion is used to account for the singular behavior of the disk current in the vicinity of the probe, ensure continuity of the current at the probe/disk junction, and speed up the convergence of the solution. An "attachment mode" which represented the disk current of a lossy magnetic cavity driven by a uniform cylindrical probe current was introduced in [16]. More recently, similar and other "attachment modes," with the $1/\rho$ dependence in the vicinity of the probe and the appropriate boundary condition on normal current, defined over the entire disk or locally over a portion of the disk, have also been used [22]–[25]. In a different approach, the effects of the probe were accounted for by expanding the currents on the disk and probe in terms of the modes of a cylindrical magnetic cavity satisfying boundary conditions on the eccentrically located probe [26].

Considered here is a microstrip antenna consisting of two circular microstrip disks in a stacked configuration driven by a coaxial probe. The two stacked configurations shown in Figs. 1(a) and 1(b), denoted configurations A and B, respectively, are investigated. The disks are assumed to be infinitesimally thin and

Manuscript received March 12, 1990; revised July 27, 1990. This work was supported by RADC under Contract F19628-88-K-0013, the ARO under Contract DAAL03-88-K-0057, the ONR under Contract N00014-90-J-1002, the Joint Services Electronics Program under Contract DAAL03-89-C-0001, and NSF Grant ECS86-20029.

The authors are with the Department of Electrical Engineering and Computer Science and Research Laboratory of Electronics, Massachusetts Institute of Technology, Cambridge, MA 02139.

IEEE Log Number 9041263.

0018-926X/91/0300-0381$01.00

perfectly conducting and the substrates are taken to be infinite in extent. A rigorous analysis of the two stacked circular disks in a layered medium is performed using a dyadic Green's function formulation. Using the vector Hankel transform, the mixed boundary value problem is reduced to a set of coupled vector integral equations and solved by employing Galerkin's method in the spectral domain. Two solutions using two different basis sets to expand the unknown disk currents are developed. The first set of basis functions used are the complete set of transverse magnetic (TM) and transverse electric (TE) modes of a cylindrical cavity with magnetic side walls. The second set of basis functions used employ Chebyshev polynomials and enforce the current edge condition. An additional term in the current expansion is taken to account for the singular nature of the current on the disk in the vicinity of the probe and to ensure continuity of current at the junction. This term, the "attachment mode," is taken to be the disk current of a magnetic cavity under a uniform cylindrical current excitation. It is shown here explicitly that continuity of the current at the probe/disk junction must be enforced to rigorously include the probe self-impedance. The convergence of the results is investigated and ensured by using a proper number of basis functions. The input impedance of the stacked microstrip antenna is calculated for different configurations of substrate parameters and disk radii. Disk current distributions and radiation patterns are also presented. Finally, the results are compared with experimental data and shown to be in good agreement. Throughout the analysis, the $\exp(-i\omega t)$ time dependence is used and suppressed.

II. Dyadic Green's Function and Integral Equation Formulation

For a general formulation which applies to both configurations A and B of Fig. 1, we consider two coaxial, circular perfectly conducting disks, of radii a_1 and a_2, carrying current distributions $\bar{J}_j(\bar{r}) = \bar{K}_j(\bar{\rho})\delta(z - z_j')$ where $j = (1, 2)$ and $\delta(\cdot)$ is the Dirac delta function. Configuration A is obtained when $z_1' = d_1$ and $z_2' = d_2$ and configuration B results when $z_1' = d_0$ and $z_2' = d_2$.

Using the induced EMF method [27], a stationary formula for the input impedance is obtained as

$$Z_{in} = -\frac{1}{I^2}\iiint dV \bar{E}(\bar{r}) \cdot \bar{J}_{probe}(\bar{r}) \tag{1}$$

where $\bar{J}_{probe}$ is the current distribution on the probe and $\bar{E}$ is the total electric field due to the probe current and induced disk currents.

The current on the probe, of radius R and at the position $\bar{\rho}_0 \equiv (\rho_0, \phi_0)$, is taken to be uniform and is given by

$$\bar{J}_{probe}(\bar{\rho}, z) = \hat{z}\frac{I}{2\pi R}\delta(\rho_p - R), \qquad d_2 < z < d_2 \tag{2}$$

with local coordinates defined as $\bar{\rho}_p = \bar{\rho} - \bar{\rho}_0 \equiv (\rho_p, \phi_p)$.

Using a dyadic Green's function formulation in cylindrical coordinates for horizontally stratified media [11], we obtain expressions for the transverse components of the electric fields due to the disk and probe current distributions. Boundary conditions require that the transverse components of the electric field vanish on the perfectly conducting disks and the currents vanish off the disks, to give the following set of coupled integral equations for the disk currents

$$\begin{aligned}\left[\bar{E}(\bar{\rho}, z = z_j')\right]_T = &\sum_{m=-\infty}^{\infty} e^{im\phi}\int_0^{\infty} dk_\rho\, k_\rho \bar{\bar{J}}_m(k_\rho\rho) \\ &\cdot \bar{\bar{\xi}}_{j,1}(k_\rho, z = z_j', z' = z_1') \cdot \bar{\kappa}_m^{(1)}(k_\rho) \\ &+ \sum_{m=-\infty}^{\infty} e^{im\phi}\int_0^{\infty} dk_\rho\, k_\rho \bar{\bar{J}}_m(k_\rho\rho) \\ &\cdot \bar{\bar{\xi}}_{j,2}(k_\rho, z = z_j', z' = z_2') \cdot \bar{\kappa}_m^{(2)}(k_\rho) \\ &+ \sum_{m=-\infty}^{\infty} e^{im\phi}\int_0^{\infty} dk_\rho\, k_\rho \bar{\bar{J}}_m(k_\rho\rho) \\ &\cdot \bar{\bar{\xi}}_{j,3}^{TM}(k_\rho, z = z_j') \cdot \bar{p}_m(k_\rho) \\ = 0, &\qquad \rho < a_j \end{aligned} \tag{3}$$

$$\begin{aligned}\bar{K}_m^{(j)}(\rho) = &\int_0^{\infty} d\rho\, \rho \bar{\bar{J}}_m(k_\rho\rho) \\ &\cdot \bar{\kappa}_m^{(j)}(k_\rho) = 0, \qquad \rho > a_j\end{aligned} \tag{4}$$

where $j = 1, 2$, and k_ρ is the transverse wavenumber satisfying the dispersion relation

$$k_\rho^2 + k_{lz}^2 = k_l^2 = \omega^2\mu_l\epsilon_l \tag{5}$$

in each region l. In (3), z and z' correspond to the longitudinal positions of observer and source, respectively. $\bar{\kappa}_m^{(1)}(k_\rho)$ and $\bar{\kappa}_m^{(2)}(k_\rho)$ are the vector Hankel transforms of the two disk currents $\bar{K}_m^{(1)}(\rho)$ and $\bar{K}_m^{(2)}(\rho)$, respectively, defined by

$$\bar{\kappa}_m^{(j)}(k_\rho) = \int_0^{\infty} d\rho\, \rho \bar{\bar{J}}_m^{\dagger}(k_\rho\rho) \cdot \bar{K}_m^{(j)}(\rho) \tag{6}$$

where $\bar{K}_m^{(j)}(\rho)$ is the Fourier coefficient

$$\bar{K}_m^{(j)}(\rho) = \frac{1}{2\pi}\int_0^{2\pi} d\phi\, e^{-im\phi}\bar{K}_j(\bar{\rho}) \tag{7}$$

and $\bar{\bar{J}}_m(k_\rho\rho)$ is the kernel of the vector Hankel transform (VHT) [28] given by

$$\bar{\bar{J}}_m(k\rho\rho) = \begin{bmatrix} J_m'(k_\rho\rho) & \dfrac{-im}{k_\rho\rho}J_m(k_\rho\rho) \\ \dfrac{im}{k_\rho\rho}J_m(k_\rho\rho) & J_m'(k_\rho\rho) \end{bmatrix}. \tag{8}$$

$J_m(\cdot)$ is the Bessel function of the first kind of order m and the prime denotes differentiation with respect to the argument. $\bar{\bar{J}}_m^{\dagger}(k_\rho\rho)$ is the complex conjugate transpose of $\bar{\bar{J}}_m(k_\rho\rho)$.

In the last term of (3), $\bar{p}_m(k_\rho)$ is associated with the probe current and is given by

$$\bar{p}_m(k_\rho) = \begin{bmatrix} p_m(k_\rho) \\ 0 \end{bmatrix} \tag{9}$$

where

$$p_m(k_\rho) = -\frac{I}{2\pi}\frac{k_\rho}{k_{3z}^2}J_m(k_\rho\rho_0)J_0(k_\rho R)e^{-im\phi_0}. \tag{10}$$

The matrix $\bar{\bar{\xi}}_{l,3}^{TM}(k_\rho, z)$ includes the effects of the stratified medium when relating the probe current to the transverse elec-

tric fields and is defined as

$$\bar{\bar{\xi}}_{l,3}^{\mathrm{TM}}(k_\rho, z) = \begin{bmatrix} \xi_{l,3}^{\mathrm{TM}} & 0 \\ 0 & 0 \end{bmatrix}. \tag{11}$$

It is clear that the assumed probe current excites TM modes only. The matrices $\bar{\bar{\xi}}_{l,j}(k_\rho, z, z')$ with $l, j = (1,2)$ in (3) include the effects of the stratified medium when relating the disk currents to transverse electric fields and are of the form

$$\bar{\bar{\xi}}_{l,j}(k_\rho, z, z') = \begin{bmatrix} \xi_{l,j}^{\mathrm{TM}} & 0 \\ 0 & \xi_{l,j}^{\mathrm{TE}} \end{bmatrix}. \tag{12}$$

The expressions for $\xi_{l,3}^{\mathrm{TM}}(k_\rho, z)$, $\xi_{l,j}^{\mathrm{TM}}(k_\rho, z, z')$, and $\xi_{l,j}^{\mathrm{TE}}(k_\rho, z, z')$ are given in the Appendix.

III. Galerkin's Method

Galerkin's method is employed to solve the coupled vector integral equations of (3) and (4). The currents on the circular disks are expanded in terms of a set of basis functions

$$\bar{K}_m^{(1)}(\rho) = \sum_n^N a_{mn}^{(1)} \bar{\Psi}_{mn}^{(1)}(\rho) + \sum_p^P b_{mp}^{(1)} \bar{\Phi}_{mp}^{(1)}(\rho) \tag{13a}$$

$$\bar{K}_m^{(2)}(\rho) = \sum_r^R a_{mr}^{(2)} \bar{\Psi}_{mr}^{(2)}(\rho) + \sum_s^S b_{ms}^{(2)} \bar{\Phi}_{ms}^{(2)}(\rho) + \bar{K}_{m,att}^{(2)}(\rho). \tag{13b}$$

N and P correspond to the number basis functions $\bar{\psi}_{mj}(\rho)$ and $\bar{\phi}_{mj}(\rho)$, respectively, taken for the upper disk and R and S correspond to those taken for the lower disk. $\bar{K}_{m,att}^{(2)}(\rho)$ is the "attachment mode."

The corresponding VHT of the currents is given by

$$\bar{\kappa}_m^{(1)}(k_\rho) = \sum_n^N a_{mn}^{(1)} \bar{\psi}_{mn}^{(1)}(k_\rho) + \sum_p^P b_{mp}^{(1)} \bar{\phi}_{mp}^{(1)}(k_\rho) \tag{14a}$$

$$\bar{\kappa}_m^{(2)}(k_\rho) = \sum_r^R a_{mr}^{(2)} \bar{\psi}_{mr}^{(2)}(k_\rho) + \sum_s^S b_{ms}^{(2)} \bar{\phi}_{ms}^{(2)}(k_\rho) + \bar{\kappa}_{m,att}^{(2)}(k_\rho). \tag{14b}$$

A. TM and TE Modes of Cylindrical Cavities with Magnetic Side Walls

One set of basis functions taken are those currents associated with the complete orthogonal set of TM and TE modes of a cylindrical cavity of radius a_j $(j = 1,2)$ with magnetic side walls and electric top and bottom walls. These current modes are given by

$$\bar{\Psi}_{mn}^{(j)}(\rho) = \begin{cases} \begin{bmatrix} J_m'(\beta_{mn}\rho/a_j) \\ \dfrac{ima_j}{\beta_{mn}\rho} J_m(\beta_{mn}\rho/a_j) \end{bmatrix}, & \text{for } \rho < a_j \\ 0, & \text{for } \rho > a_j \end{cases} \tag{15a}$$

$$\bar{\Phi}_{mp}^{(j)}(\rho) = \begin{cases} \begin{bmatrix} \dfrac{-ima_j}{\alpha_{mp}\rho} J_m(\alpha_{mp}\rho/a_j) \\ J_m'(\alpha_{mp}\rho/a_j) \end{bmatrix}, & \text{for } \rho < a_j \\ 0, & \text{for } \rho > a_j \end{cases} \tag{15b}$$

for $m = 0, \pm 1, \pm 2, \cdots$, $n = 1, 2, \cdots$, and $p = 1, 2, \cdots$ $\bar{\Psi}_{mn}^{(j)}(\rho)$ correspond to the TM cavity modes and $\bar{\Phi}_{mn}^{(j)}(\rho)$ correspond to the TE cavity modes. The constants β_{mn} and α_{mp} correspond to the nth and pth zeros of $J_m'(\beta_{mn}) = 0$ and $J_m(\alpha_{mp}) = 0$, respectively. The VHT of these basis functions is

$$\bar{\psi}_{mn}^{(j)}(k_\rho) = \beta_{mn} J_m(\beta_{mn}) \begin{bmatrix} \dfrac{J_m'(k_\rho a_j)}{(\beta_{mn}/a_j)^2 - k_\rho^2} \\ \dfrac{ima_j}{\beta_{mn}^2 k_\rho} J_m(k_\rho a_j) \end{bmatrix} \tag{16a}$$

$$\bar{\phi}_{mp}^{(j)}(k_\rho) = \frac{k_\rho a_j J_m'(\alpha_{mp})}{k_\rho^2 - (\alpha_{mp}/a_j)^2} \begin{bmatrix} 0 \\ J_m(k_\rho a_j) \end{bmatrix}. \tag{16b}$$

B. Chebyshev Polynomial Expansion with Edge Condition

The second set of basis functions taken includes the edge condition for the disk currents and is taken to be [23]

$$\bar{\Psi}_{mn}^{(j)}(\rho) = \begin{cases} \hat{\rho} T_n(\rho/a_j)\sqrt{1 - \rho^2/a_j^2}, & \text{for } \rho < a_j \\ 0, & \text{for } \rho > a_j \end{cases} \tag{17a}$$

$$\bar{\Phi}_{mn}^{(j)}(\rho) = \begin{cases} \hat{\phi} T_n(\rho/a_j)/\sqrt{1 - \rho^2/a_j^2}, & \text{for } \rho < a_j \\ 0, & \text{for } \rho > a_j \end{cases} \tag{17b}$$

for $m = 0, \pm 1, \pm 2, \cdots$ and $n = 0, 1, 2, \cdots$ $T_n(x)$ is the Chebyshev polynomial [29] and satisfies the recursion formula $T_{n+1}(x) - 2xT_n(x) + T_{n-1}(x) = 0$ with $T_0(x) = 1$ and $T_1(x) = x$. The term $\sqrt{1 - \rho^2/a_j^2}$ provides for the proper singular edge behavior for the azimuthally directed current and the zero edge condition for the normally directed current. Since the current basis functions must have continuous current distributions on the disk, the mode index m and the Chebyshev polynomial index n may not be both even or both odd when performing the current expansion.

The VHT of the above basis functions is given by

$$\bar{\psi}_{mn}^{(j)}(k_\rho) = \begin{bmatrix} I_{mn}^{\psi(j)}(k_\rho) - mJ_{mn}^{\psi(j)}(k_\rho) \\ imJ_{mn}^{\psi(j)}(k_\rho) \end{bmatrix} \tag{18a}$$

$$\bar{\phi}_{mn}^{(j)}(k_\rho) = \begin{bmatrix} -imJ_{mn}^{\phi(j)}(k_\rho) \\ I_{mn}^{\phi(j)}(k_\rho) - mJ_{mn}^{\phi(j)}(k_\rho) \end{bmatrix} \tag{18b}$$

for $m \geq 0$. The integrals, with $y_j = k_\rho a_j$, are defined by

$$\begin{aligned} I_{mn}^{\psi(j)} = \frac{a_j^2}{8}\frac{4}{y_j}\frac{\pi}{2}\Bigg[& -\left(\frac{m-n-2}{2}\right) \\ & \cdot J_{(m+n+2)/2}(y_j/2) J_{(m-n-2)/2}(y_j/2) \\ & -\left(\frac{m+n-2}{2}\right) J_{(m+n-2)/2}(y_j/2) \\ & \cdot J_{(m-n+2)/2}(y_j/2) \\ & + mJ_{(m+n)/2}(y_j/2) J_{(m-n)/2}(y_j/2)\Bigg] \end{aligned} \tag{19a}$$

$$J_{mn}^{\psi(j)} = \frac{a_j^2}{4}\frac{1}{y_j}\frac{\pi}{2}\left[-J_{(m+n+2)/2}(y_j/2)\,J_{(m-n-2)/2}(y_j/2) + 2\,J_{(m+n)/2}(y_j/2)\,J_{(m-n)/2}(y_j/2) - J_{(m+n-2)/2}(y_j/2)\,J_{(m-n+2)/2}(y_j/2)\right] \quad (19b)$$

$$I_{mn}^{\phi(j)} = \frac{a_j^2}{2}\frac{\pi}{2}\left[J_{(m+n)/2}(y_j/2)\,J_{(m-n-2)/2}(y_j/2) + J_{(m+n-2)/2}(y_j/2)\,J_{(m-n)/2}(y_j/2)\right] \quad (19c)$$

$$J_{mn}^{\phi(j)} = \frac{a_j^2}{y_j}\frac{\pi}{2}\left[J_{(m+n)/2}(y_j/2)\,J_{(m-n)/2}(y_j/2)\right]. \quad (19d)$$

In the above expressions, when m and n are not both even or both odd, the Bessel functions $J_{M/2}(\cdot)$ are of half-integer order [30].

C. Attachment Mode

The "attachment mode" term in the current expansion is taken to approximate the rapidly varying currents in the vicinity of the probe/disk junction, ensure continuity of the current, and speed up the convergence of the solution. This term is taken as the disk current of a magnetic cavity of radius a_2 due to a uniform cylindrical current source of radius R positioned at $\bar{\rho}_0$ and given by

$$\bar{K}_{alt}^{(2)}(\bar{\rho}) = \frac{I}{2\pi}\sum_{m=-\infty}^{\infty} e^{im(\phi-\phi_0)}\int_0^{\infty} dk_\rho \frac{k_\rho^2}{k_{3z}^2} \cdot J_0(k_\rho R)\,J_m(k_\rho\rho_0)\begin{bmatrix} J_m'(k_\rho\rho) \\ \dfrac{im}{k_\rho\rho}J_m(k_\rho\rho)\end{bmatrix} + \frac{ik_3 I}{4}\sum_{m=-\infty}^{\infty} e^{im(\phi-\phi_0)} \cdot \frac{J_0(k_3R)\,J_m(k_3\rho_0)\,H_m^{(1)\prime}(k_3a_2)}{J_m'(k_3a_2)} \cdot \begin{bmatrix} J_m'(k_3\rho) \\ \dfrac{im}{k_3\rho}J_m(k_3\rho)\end{bmatrix}, \quad 0 \le \rho \le a_2 \quad (20)$$

where $H_m^{(1)}(\cdot)$ is the Hankel function of the first kind of order m. The first term in (20) is the current induced on infinite parallel conducting planes by a uniform cylindrical current. The second term is a homogeneous solution to the wave equation added to satisfy the boundary condition $\bar{H}_{tan}(\rho = a_2) = 0$, providing for vanished normal current at the edge of the disk.

The VHT of the above attachment mode current distribution has a closed form analytic expression given by

$$\bar{\kappa}_{m,alt}^{(2)}(k_\rho) = \frac{I}{2\pi}e^{-im\phi_0}\frac{k_\rho}{k_{3z}^2}J_0(k_\rho R)\,J_m(k_\rho\rho_0)\begin{bmatrix}1\\0\end{bmatrix} - \frac{I}{2\pi}e^{-im\phi_0}\frac{J_0(k_3R)\,J_m(k_3\rho_0)}{J_m'(k_3a_2)} \cdot \begin{bmatrix} \dfrac{k_3}{k_{3z}^2}J_m'(k_\rho a_2) \\ \dfrac{im}{k_3a_2k_\rho}J_m(k_\rho a_2)\end{bmatrix}. \quad (21)$$

D. Matrix Equation

Substituting the current expansion of (14) into (3), and applying Parseval's theorem, we obtain a system of $N + P + R + S$ linear algebraic equations for each mode m which may be written in matrix form

$$\bar{\bar{A}}_m \cdot \bar{c}_m = \bar{d}_m \quad (22)$$

where

$$\bar{\bar{A}}_m = \begin{bmatrix} [A]_{N\times N}^{\psi^{(1)}\psi^{(1)}} & [A]_{N\times P}^{\psi^{(1)}\phi^{(1)}} & [A]_{N\times R}^{\psi^{(1)}\psi^{(2)}} & [A]_{N\times S}^{\psi^{(1)}\phi^{(2)}} \\ [A]_{P\times N}^{\phi^{(1)}\psi^{(1)}} & [A]_{P\times P}^{\phi^{(1)}\phi^{(1)}} & [A]_{P\times R}^{\phi^{(1)}\psi^{(2)}} & [A]_{P\times S}^{\phi^{(1)}\phi^{(2)}} \\ [A]_{R\times N}^{\psi^{(2)}\psi^{(1)}} & [A]_{R\times P}^{\psi^{(2)}\phi^{(1)}} & [A]_{R\times R}^{\psi^{(2)}\psi^{(2)}} & [A]_{R\times S}^{\psi^{(2)}\phi^{(2)}} \\ [A]_{S\times N}^{\phi^{(2)}\psi^{(1)}} & [A]_{S\times P}^{\phi^{(2)}\phi^{(1)}} & [A]_{S\times R}^{\phi^{(2)}\psi^{(2)}} & [A]_{S\times S}^{\phi^{(2)}\phi^{(2)}} \end{bmatrix} \quad (23)$$

and

$$\bar{c}_m = \begin{bmatrix} [a_m^{(1)}]_{N\times 1} \\ [b_m^{(1)}]_{P\times 1} \\ [a_m^{(2)}]_{R\times 1} \\ [b_m^{(2)}]_{S\times 1}\end{bmatrix} \quad (24)$$

$$\bar{d}_m = \begin{bmatrix} [d_m^{\psi^{(1)}}]_{N\times 1} \\ [d_m^{\phi^{(1)}}]_{P\times 1} \\ [d_m^{\psi^{(2)}}]_{R\times 1} \\ [d_m^{\phi^{(2)}}]_{S\times 1}\end{bmatrix}. \quad (25)$$

Each element of the submatrices of $\bar{\bar{A}}_m$ is given by

$$A_{mnp}^{\gamma^{(i)}\chi^{(j)}} = \int_0^{\infty} dk_\rho k_\rho \bar{\gamma}_{mn}^{(i)\dagger}(k_\rho)\cdot\bar{\bar{\xi}}_{i,j}(k_\rho, z_i', z_j')\cdot\bar{\chi}_{mp}^{(j)}(k_\rho) \quad (26)$$

where $\bar{\gamma}_{mn}^{(j)}(k_\rho)$ and $\bar{\chi}_{mm}^{(j)}(k_\rho)$ represent either $\bar{\psi}_{mn}^{(j)}(k_\rho)$ or $\bar{\phi}_{mn}^{(j)}(k_\rho)$. Each element of the excitation matrix $\bar{d}_m$ is given by

$$d_{mn}^{(i)} = -\int_0^{\infty} dk_\rho k_\rho \bar{\gamma}_{mn}^{(i)\dagger}(k_\rho)\cdot\bar{\bar{\xi}}_{i,3}^{\mathrm{TM}}(k_\rho, z_i')\cdot\bar{p}_m(k_\rho) - \int_0^{\infty} dk_\rho k_\rho \gamma_{mn}^{(i)\dagger}(k_\rho)\cdot\bar{\bar{\xi}}_{i,2}(k_\rho, z_i', z_2')\cdot\bar{\kappa}_m^{(2,\mathrm{alt})}(k_\rho). \quad (27)$$

IV. Input Impedance

Once the induced current distribution on the microstrip disks due to the coaxial probe excitation is solved for, the input impedance of the stacked microstrip antenna may be calculated. Applying (1), the input impedance for the stacked microstrip antenna is given by

$$Z_{in} = -\frac{1}{I^2}\int_{d_3}^{d_2} dz \int_0^{2\pi} d\phi_p \int_0^{\infty} d\rho_p \rho_p \left\{\left[\bar{E}_{3,1}(\bar{r})\right]_z + \left[\bar{E}_{3,2}(\bar{r})\right]_z + \left[\bar{E}_{self}(\bar{r})\right]_z\right\}\cdot\frac{I}{2\pi R}\delta(\rho_p - R) \quad (28)$$

where $\bar{E}_{3,j}(\bar{r})$ is the electric field due to disk current j and $\bar{E}_{\text{self}}(\bar{r})$ is the electric field due to the probe current. After integration over the cylindrical probe surface and some manipulation, we arrive at

$$\begin{aligned} Z_{\text{in}} &= -\frac{2\pi}{I^2}\sum_{m=-\infty}^{\infty}\int_0^{\infty} dk_\rho k_\rho p_m^*(k_\rho)\{\eta_{3,1}^{\text{TM}}(k_\rho) \\ &\quad\cdot\left[\bar{K}_m^{(1)}(k_\rho)\right]_\rho + \eta_{3,2}^{\text{TM}}(k_\rho)\left[\bar{K}_m^{(2)}(k_\rho)\right]_\rho\} + Z_{\text{in}}^{(\text{self})} \\ &= -\frac{2\pi}{I^2}\sum_{m=-\infty}^{\infty}\int_0^{\infty} dk_\rho k_\rho p_m^*(k_\rho)\Bigg\{\eta_{3,1}^{\text{TM}}(k_\rho) \\ &\quad\cdot\sum_{n}^{N} a_{mn}^{(1)}\left[\bar{\psi}_{mn}^{(1)}(k_\rho)\right]_\rho + \eta_{3,1}^{\text{TM}}(k_\rho)\sum_{p}^{P} b_{mp}^{(1)} \\ &\quad\cdot\left[\bar{\phi}_{mp}^{(1)}(k_\rho)\right]_\rho + \eta_{3,2}^{\text{TM}}(k_\rho)\sum_{r}^{R} a_{mr}^{(2)}\left[\bar{\psi}_{mr}^{(2)}(k_\rho)\right]_\rho \\ &\quad+\eta_{3,2}^{\text{TM}}(k_\rho)\sum_{s}^{S} b_{ms}^{(2)}\left[\bar{\phi}_{ms}^{(2)}(k_\rho)\right]_\rho\Bigg\} + Z_{\text{in}}^{(\text{self})} + Z_{\text{in}}^{(2,\text{att})} \end{aligned} \tag{29}$$

where

$$\begin{aligned} \eta_{3,1}^{\text{TM}}(k_\rho) &= -\frac{\eta_1}{2}\frac{k_{1z}}{k_1} \\ &\quad\cdot\frac{\left[1-R_{\cap 1}^{\text{TM}}\right]\left[1-R_{\cap 2}^{\text{TM}}\right]\left[1-R_{U1}^{\text{TM}}e^{i2k_{3z}(d_0-z_1')}\right]}{\left[1-R_{U1}^{\text{TM}}R_{\cap 1}^{\text{TM}}e^{i2k_{1z}h_1}\right]\left[1-R_{\cap 2}^{\text{TM}}e^{i2k_{2z}h_2}\right]} \\ &\quad\cdot e^{ik_{1z}(z_1'-d_1)}e^{ik_{2z}h_2} \end{aligned} \tag{30}$$

$$\eta_{3,2}^{\text{TM}}(k_\rho) = -\frac{\eta_3}{2}\frac{k_{3z}}{k_3}\frac{\left[1-R_{U3}^{\text{TM}}\right]\left[1-e^{i2k_{3z}h_3}\right]}{\left[1-R_{U3}^{\text{TM}}e^{i2k_{3z}h_3}\right]} \tag{31}$$

and $\eta_l = \sqrt{\mu_l/\epsilon_l}$. The expressions for the generalized reflection coefficients R_{Ul}^{α} and $R_{\cap l}^{\alpha}$ are given in the Appendix. $Z_{in}^{(\text{self})}$ represents the self-impedance of the probe and may be expressed as

$$\begin{aligned} Z_{\text{in}}^{(\text{self})} &= \frac{\eta_3}{4}k_3h_3J_0(k_3R)H_0^{(1)}(k_3R) - \frac{1}{2\pi}\int_0^{\infty} \\ &\quad\cdot dk_\rho k_\rho J_0^2(k_\rho R)\left(\frac{k_\rho^2}{k_{3z}^4}\right)\eta_{3,2}^{\text{TM}}(k_\rho) \end{aligned} \tag{32}$$

$Z_{in}^{(2,\text{att})}$ is the input impedance term due to the attachment mode and is given by

$$\begin{aligned} Z_{\text{in}}^{(2,\text{att})} &= \frac{1}{2\pi}\int_0^{\infty} dk_\rho k_\rho J_0^2(k_\rho R)\left(\frac{k_\rho^2}{k_{3z}^4}\right)\eta_{3,2}^{\text{TM}}(k_\rho) \\ &\quad-\frac{1}{I}\sum_{m=-\infty}^{\infty} e^{-im\phi_0}\frac{J_0(k_3R)J_m(k_3\rho_0)}{J_m'(k_3a_2)}\int_0^{\infty} \\ &\quad\cdot dk_\rho k_\rho p_m^*(k_\rho)J_m'(k_\rho a_2)\left(\frac{k_3}{k_{3z}^2}\right)\eta_{3,2}^{\text{TM}}(k_\rho). \end{aligned} \tag{33}$$

The first term of the probe self-impedance in (32) corresponds to the input impedance of a coaxial probe driven parallel-plate waveguide. In the small k_3R limit, this term reduces to

$$\begin{aligned} &\lim_{k_3R\to 0}\frac{\eta_3}{4}k_3h_3J_0(k_3R)H_0^{(1)}(k_3R) \\ &\quad= i\frac{\eta_0}{2\pi}k_0h_3\frac{\mu_3}{\mu_0}\ln(k_3R) = i60k_0h_3\frac{\mu_3}{\mu_0}\ln(k_3R) \end{aligned}$$

which is the formula used by some authors as the probe reactance [24]. Upon careful inspection of the expression for the probe self-impedance $Z_{in}^{(\text{self})}$, it is noted that the second term in (32) containing $\eta_{3,2}^{\text{TM}}(k_\rho)$ is zero when R_{U3}^{TM} is equal to one—the case of a probe-fed parallel plate waveguide. When R_{U3}^{TM} is not equal to one, this term diverges. This is because the uniform current on the probe leads to a singular charge accumulation at the probe end giving rise to a singular reactance. Thus, in the case of a microstrip disk excited by a probe, in order to account properly for the probe-self impedance, the continuity of the current at the probe-disk junction must be ensured. If we take the impedance due to the probe and the attachment mode current together, we arrive at the following:

$$\begin{aligned} &Z_{\text{in}}^{(\text{self})} + Z_{\text{in}}^{(2,\text{att})} \\ &\quad= \frac{\eta_3}{4}k_3h_3J_0(k_3R)H_0^{(1)}(k_3R) \\ &\quad\quad-\frac{1}{I}\sum_{m=-\infty}^{\infty} e^{-im\phi_0}\frac{J_0(k_3R)J_m(k_3\rho_0)}{J_m'(k_2a_2)} \\ &\quad\quad\cdot\int_0^{\infty} dk_\rho k_\rho p_m^*(k_\rho)J_m'(k_\rho a_2)\left(\frac{k_3}{k_{3z}^2}\right)\eta_{3,2}^{\text{TM}}(k_\rho) \end{aligned} \tag{34}$$

where the divergent term in the probe self-impedance $Z_{\text{in}}^{(\text{self})}$ has been cancelled by the contribution of the attachment mode which ensures continuity of the current.

V. Radiation Fields

The radiation field, or far field, components in region 0 may be obtained from the longitudinal components with

$$E_{0\phi} = \frac{\eta_0 H_{0z}}{\sin\theta} \quad E_{0\theta} = -\frac{E_{0z}}{\sin\theta}. \tag{35}$$

For large observation distances, the expressions for the field components may be evaluated using the saddle point method with the saddle point being $k_\rho = k_0\sin\theta$ where $\theta = \tan^{-1}(\rho/z)$. The longitudinal field components due to disk current $\bar{K}_j(\bar{\rho})$ are given by

$$\begin{aligned} E_{0z}^{(j)}(\bar{\rho},z) &= \sum_{m=-\infty}^{\infty} e^{im\phi}(-i)^m\{k_\rho e_{0,j}(k_\rho,z_j') \\ &\quad\cdot\left[\bar{\kappa}_m^{(j)}(k_\rho)\right]_\rho\}_{k_\rho=k_0\sin\theta}\frac{e^{ik_0r}}{r} \end{aligned} \tag{36a}$$

$$\begin{aligned} H_{0z}^{(j)}(\bar{\rho},z) &= \sum_{m=-\infty}^{\infty} e^{im\phi}(-i)^m\{k_\rho h_{0,j}(k_\rho,z_j') \\ &\quad\cdot\left[\bar{\kappa}_m^{(j)}(k_\rho)\right]_\phi\}_{k_\rho=k_0\sin\theta}\frac{e^{ik_0r}}{r} \end{aligned} \tag{36b}$$

where

$$e_{0,1}(k_\rho, z_1') = \frac{\eta_1}{2}\frac{k_{1z}}{k_1} \cdot \frac{\left[1 - R_{U1}^{TM}\right]\left[1 - R_{\cap 1}^{TM} e^{i2k_{1z}(z_1 - d_1)}\right]}{1 - R_{U1}^{TM} R_{\cap 1}^{TM} e^{i2k_{1z}h_1}} \cdot e^{ik_{1z}(d_0 - z_1')} e^{-ik_{0z}d_0} \quad (37a)$$

$$h_{0,1}(k_\rho, z_1') = -\frac{\mu_1}{\mu_0}\frac{k_{0z}}{k_{1z}} \cdot \frac{\left[1 + R_{U1}^{TE}\right]\left[1 + R_{\cap 1}^{TE} e^{i2k_{1z}(z_1 - d_1)}\right]}{1 - R_{U1}^{TE} R_{\cap 1}^{TE} e^{i2k_{1z}h_1}} \cdot e^{-ik_{0z}d_0} e^{ik_{1z}(d_0 - z_1')} \quad (37b)$$

$$e_{0,2}(k_\rho, z_2') = \frac{\eta_2}{2}\frac{k_{2z}}{k_2} \cdot \frac{\left[1 - R_{U1}^{TM}\right]\left[1 - R_{U2}^{TM}\right]\left[1 - R_{\cap 2}^{TM}\right]}{\left[1 - R_{U2}^{TM} R_{\cap 2}^{TM} e^{i2k_{2z}h_2}\right]\left[1 - R_{U1}^{TM} e^{i2k_{1z}h_1}\right]} \cdot e^{-ik_{0z}d_0} e^{ik_{1z}h_1} e^{ik_{2z}h_2} \quad (37c)$$

$$h_{0,2}(k_\rho, z_2') = -\frac{\mu_2}{\mu_0}\frac{k_{0z}}{k_{2z}} \cdot \frac{\left[1 + R_{U1}^{TE}\right]\left[1 + R_{U2}^{TE}\right]\left[1 + R_{\cap 2}^{TE}\right]}{\left[1 - R_{U2}^{TE} R_{\cap 2}^{TE} e^{i2k_{2z}h_2}\right]\left[1 + R_{U1}^{TE} e^{i2k_{1z}h_1}\right]} \cdot e^{-ik_{0z}d_0} e^{ik_{1z}h_1} e^{ik_{2z}h_2}. \quad (37d)$$

Likewise, the radiation field component due to the probe is given by

$$E_{0z}^{P}(\bar{\rho}, z) = \sum_{m=-\infty}^{\infty} e^{im\phi}(-i)^m \cdot \left\{\frac{k_\rho}{k_{3z}} e_{0,3}^{P}(k_\rho) p_m(k_\rho)\right\}_{k_\rho = k_0 \sin\theta} \frac{e^{ik_0 r}}{r} \quad (38)$$

where

$$e_{0,3}^{P}(k_\rho) = \frac{\eta_3}{2}\frac{k_{3z}}{k_3} \frac{\left[1 - R_{U1}^{TM}\right]\left[1 - R_{U2}^{TM}\right]\left[1 - R_{U3}^{TM}\right]\left[1 - e^{i2k_{3z}h_3}\right]}{\left[1 - R_{U3}^{TM} e^{i2k_{3z}h_3}\right]\left[1 - R_{U1}^{TM} e^{i2k_{1z}h_1}\right]\left[1 - R_{U2}^{TM} e^{i2k_{2z}h_2}\right]} e^{-ik_{0z}d_0} e^{ik_{1z}h_1} e^{ik_{2z}h_2}. \quad (39)$$

VI. Numerical Results and Discussion

The integrals of the matrix elements, (26) and (27), and in the impedance expression (29), are evaluated numerically along an integration path deformed below the real axis to avoid the singularities on the real axis which correspond to the radiating and guided modes of the layered medium. When using cavity mode basis functions, the integrands vary asymptotically as $1/k_\rho^3$ while those using the Chebyshev polynomial basis functions with the edge condition vary asymptotically as $1/k_\rho^2$. To enhance the convergence of the integrals when using the Chebyshev polynomial basis functions, the asymptotic values of the integrands are subtracted out and evaluated analytically.

For the stacked microstrip configurations discussed here, the following parameters are used: $a_2 = 1.3233$ cm, $h_3 = 2h_1 = 0.115a_2$, $\epsilon_1 = \epsilon_3 = 2.45\epsilon_0$, $\epsilon_2 = 1.22\epsilon_0$ (foam), $\rho_0 = 0.6a_2$, and $R = 0.048a_2$. Given these parameters, the antenna is characterized by varying the upper radius a_1 and the separation between the disks h_2. Convergent results for the input impedance and radiation fields using cavity mode basis functions are obtained with $(N = 4, P = 3)$, $(R = 4, S = 3)$, while those using the Chebyshev polynomial basis functions with the edge condition use $(N = 3, P = 3)$, $(R = 3, S = 3)$. For the calculation of the input impedance given by (29), very good results are obtained with $m = \pm 1$ for the terms associated with the disk current amplitudes, $a_{mn}^{(1)}$, $b_{mp}^{(1)}$, $a_{mr}^{(2)}$, and $b_{ms}^{(2)}$, and taking $m = 0, \pm 1, \pm 2$ for the probe self-impedance and attachment mode terms in (34). Additional modes produce only a 1 or 2 Ω difference in the input impedance calculations for the parameters considered here. It is found numerically that the probe self-impedance and attachment mode impedance terms taken together in (34) give rise to a primarily inductive reactance contribution. Computation time for the input impedance of the stacked structure is approximately a half-hour of CPU time per frequency on a VAXstation 3500.

Calculated and measured [6] reflection coefficients, $\Gamma = (Z_{in} - Z_0)/(Z_{in} + Z_0)$ where $Z_0 = 50$ Ω, are shown in Figs. 2(a) and 2(b) for the stacked configuration case A with $a_1/a_2 = 1.01$ and h_2/a_2 equal to 0.36 and 0.48, respectively. The agreement between the measured and calculated results is very good. The loop in the impedance locus of Fig. 2(a) reduces in size in Fig. 2(b) as h_2/a_2 is increased from 0.36 to 0.48, leading to the wide bandwidth behavior of this configuration. Especially off resonance, it is seen that the attachment mode and probe self-impedance terms are required for accurate results.

In Fig. 3, return loss calculations using both cavity mode and Chebyshev polynomial basis functions are compared with measured results [6] for the case of Fig. 2(b). The agreement between the calculated and measured results is very good. A frequency shift in the results on the order of 1–2% is observed for the two sets of basis functions. Due to the presence of the upper disk in the stacked configurations, two resonances associated with the two constitutive resonators of the stacked structure [11] are easily distinguished, giving rise to a 16 % −15 dB bandwidth in this case. One resonance is associated with the resonator formed by the lower disk and the ground plane and the second resonance is associated with the resonator formed by the two disks. Comparing the return loss of the stacked configuration to that of the single disk, when the upper disk and substrate are removed, it is shown that the input impedance of the single disk presents an impedance mismatch. When the probe position is changed from $0.6a_2$ to approximately $0.3a_2$ to obtain a match, a 2.3% −10 dB bandwidth is achieved.

Fig. 4 illustrates the effect of the separation h_2/a_2 on the input impedance for the cases $a_1/a_2 = 1.05$, where the impedance has been calculated using the Chebyshev polynomial basis functions including the probe self-impedance and attachment mode terms. While the position of the lower resonance remains essentially the same, the position of the upper resonance is a function of the height h_2, decreasing with increasing h_2. As seen in the figure, the excitation of the upper resonance increases with increasing h_2 (up to a certain h_2 beyond which there is little coupling [11]). This is due to the fact that the coupling interaction between the two modes increases as the

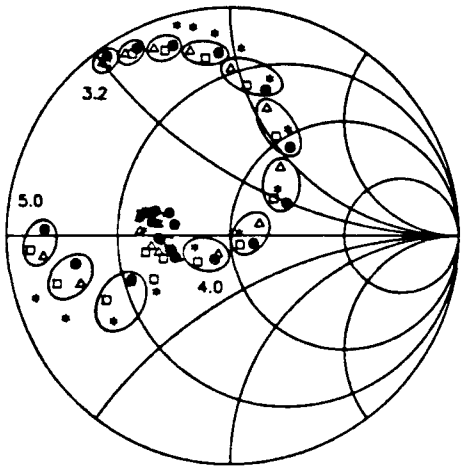

0.1 GHz increment 3.2 - 5.0 GHz

a_1/a_2 = 1.01 h_2/a_2 = 0.36

□ (3,3) Chebyshev (m=±1) with attachment mode (m=0,±1,±2)

▲ (4,3) Cavity modes (m=0,±1,±2) with attach. mode (m=0,±1,±2)

• (3,3) Chebyshev (m=±1) without attachment mode

● Measured [6]

(a)

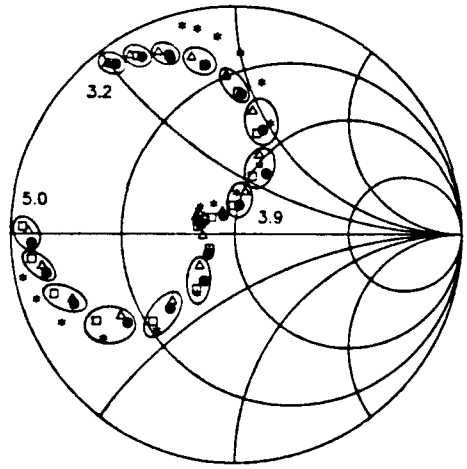

0.1 GHz increment 3.2 - 5.0 GHz

a_1/a_2 = 1.01 h_2/a_2 = 0.48

□ (3,3) Chebyshev (m=±1) with attachment mode (m=0,±1,±2)

▲ (4,3) Cavity modes (m=0,±1,±2) with attach. mode (m=0,±1,±2)

• (3,3) Chebyshev (m=±1) without attachment mode

● Measured [6]

(b)

Fig. 2. Γ of stacked configuration A. a_1/a_2 = 1.01. (a) h_2/a_2 = 0.36. (b) h_2/a_2 = 0.48.

upper resonant frequency approaches the lower resonant frequency, i.e., as the upper resonant frequency decreases with increasing h_2. Or, conversely, the coupling interaction decreases as the separation between the disks approaches zero. Calculated and measured [6] return loss results are compared in Fig. 5, where a 13% — 10 dB bandwidth is obtained in Fig. 5(a) and where dual frequency operation is observed in Fig. 5(b). Again, the agreement between the calculated and measured results is good.

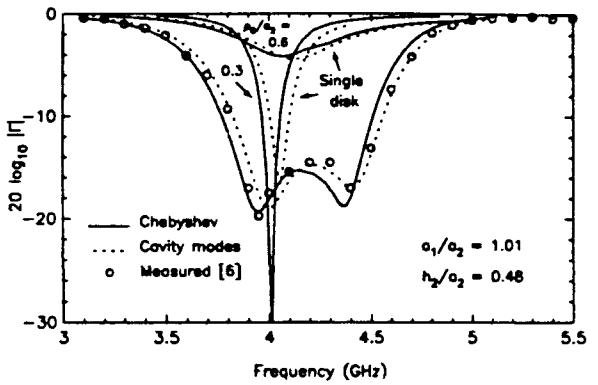

Fig. 3. Return loss of stacked configuration A. a_1/a_2 = 1.01 and h_2/a_2 = 0.48. Return loss of single disk with no upper substrate and ρ_0/a_2 = 0.3,0.6.

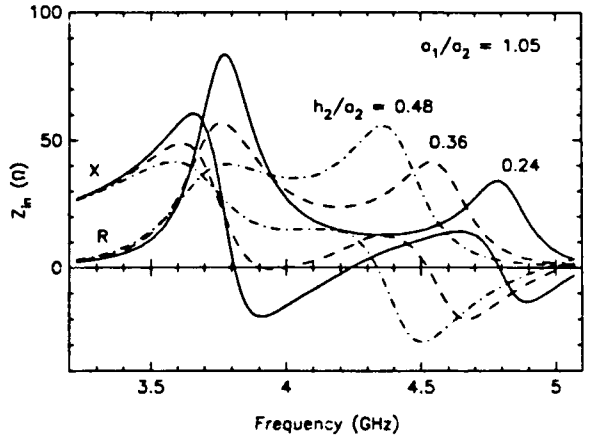

Fig. 4. Input impedance of stacked configuration A. a_1/a_2 = 1.05 and h_2/a_2 = 0.24 (—), 0.36 (- -), 0.48 (-·-).

Shown in Fig. 6 are the input impedance results of configurations A and B with parameters a_1/a_2 = 1.2 and h_2/a_2 = 0.24. Generally, the two configurations have similar characteristics. For configuration B, the increased distance between the two disks and the higher "effective" dielectric constant between the disks results in an upper resonance occurring at a lower frequency as compared with configuration A.

Illustrated in Fig. 7 are the disk current distributions for configuration A with a_1/a_2 = 1.01 and h_2/a_2 = 0.48 at the lower resonance, that is with k_3a_2 = 1.655 using (4,4) Chebyshev basis functions for each disk and k_3a_2 = 1.68 using (5,4) cavity mode basis functions for each disk. As the number of cavity mode basis functions is increased, the singular behavior at the disk edge of the $\hat{\phi}$ component of the current distribution is better characterized. The magnitude of the $\hat{\phi}$ component of the current for the upper disk is approximately uniform across the disk where the amplitude slightly increases toward the edges due to the parasitic effect of the upper disk excited by the fringing fields.

In Fig. 8, the radiation patterns of the stacked microstrip antenna configuration of Fig. 7 are compared with those of the single disk with no upper substrate. For the probe-fed single microstrip disk, the probe position is taken to be ρ_0/a_2 = 0.3, while ρ_0/a_2 = 0.6 for the stacked configuration. The E_ϕ component remains essentially the same for both the single disk and stacked configuration. The radiation pattern of the stacked con-

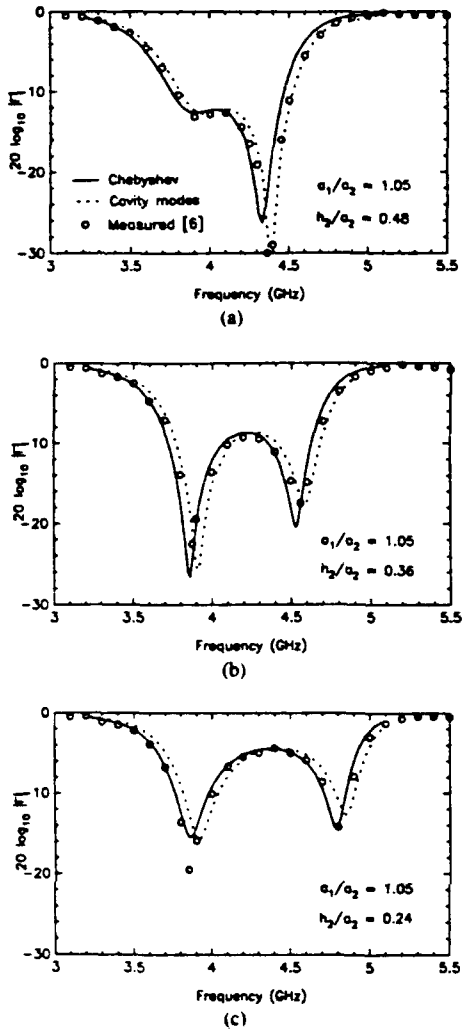

Fig. 5. Return loss of stacked configuration A. $a_1/a_2 = 1.05$. (a) $h_2/a_2 = 0.48$. (b) $h_2/a_2 = 0.36$. (c) $h_2/a_2 = 0.24$.

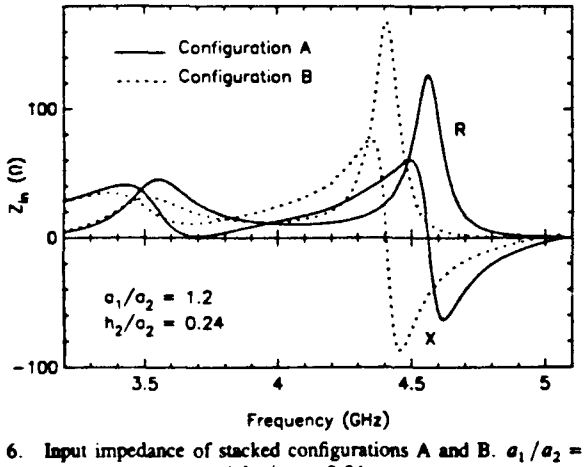

Fig. 6. Input impedance of stacked configurations A and B. $a_1/a_2 = 1.2$ and $h_2/a_2 = 0.24$.

figuration is more directive than that of the single disk, where the E_θ beamwidth is decreased in the stacked case.

VII. Conclusion

The input impedance of a microstrip antenna consisting of two circular microstrip disks in a stacked configuration driven by a coaxial probe is investigated. A rigorous analysis is performed using a dyadic Green's function formulation where the mixed boundary value problem is reduced to a set of coupled vector integral equations using the vector Hankel transform. Galerkin's method is employed in the spectral domain with an additional term used in the current expansion to account for the singular nature of the current in the vicinity of the probe, ensure continuity of the current, and to speed up convergence of the solution. Ensuring continuity of the current by means of the attachment mode is shown to be necessary for rigorously including the

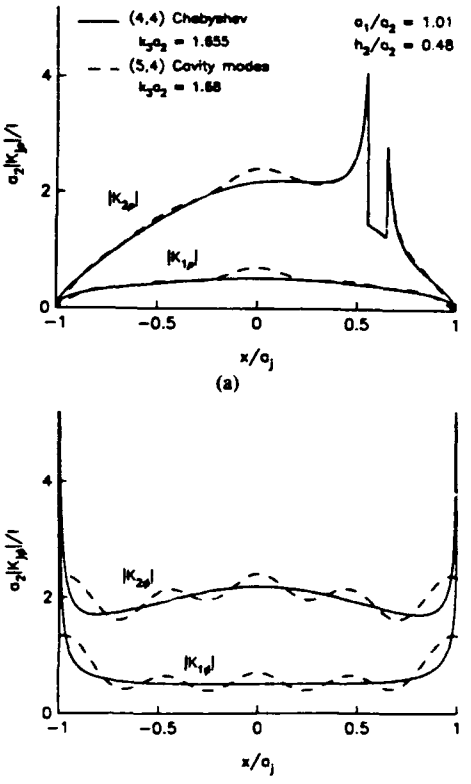

Fig. 7. Disk currents of stacked configuration A. $a_1/a_2 = 1.01$, $h_2/a_2 = 0.48$. (a) $a_2|K_{j\rho}/I|$. (b) $a_2|K_{j\phi}/I|$.

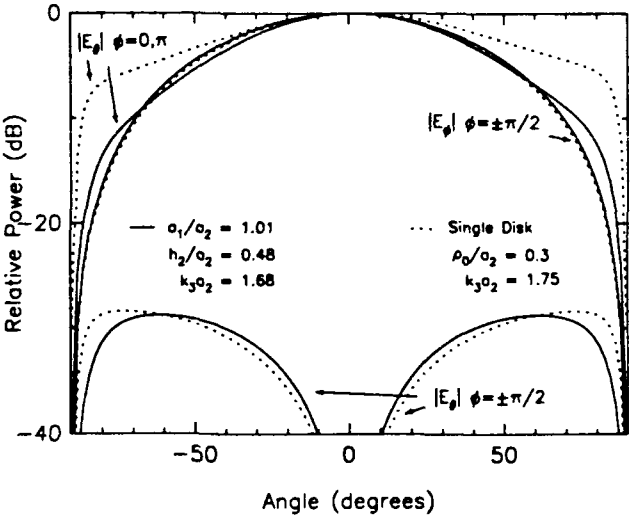

Fig. 8. Radiation pattern for stacked configuration A (—) with $a_1/a_2 = 1.01$, $h_2/a_2 = 0.48$, $k_3a_2 = 1.68$, and for single disk (· · ·) with $k_3a_2 = 1.75$ and $\rho_0/a_2 = 0.3$.

probe self-impedance and obtaining accurate results for the stacked microstrip configuration. The input impedance of the stacked microstrip antenna is calculated as a function of the layered parameters and the ratio of the two disks. Both wide bandwidth and dual frequency operation are shown. Disk current distributions and radiation patterns are also presented. Calculated results for the stacked microstrip configuration are shown to compare well with experimental data.

VIII. Appendix

The explicit expressions for $\xi_{l,3}^{TM}(k_\rho, z)$, $\xi_{l,j}^{TM}(k_\rho, z, z')$, and $\xi_{l,j}^{TE}(k_\rho, z, z')$ of (11) and (12) are given here. For the stacked configurations of Fig. 1, we have

$$\xi_{2,3}^{TM}(k_\rho, z_2') = -\frac{\eta_3}{2}\frac{k_{3z}}{k_3} \cdot \frac{\left[1 - R_{\cup 3}^{TM}\right]\left[1 + R_{\cap 3}^{TM} e^{ik_{3z}h_3}\right]\left[1 - e^{ik_{3z}h_3}\right]}{\left[1 - R_{\cup 3}^{TM} R_{\cap 3}^{TM} e^{i2k_{3z}h_3}\right]} \tag{40}$$

$$\xi_{1,3}^{TM}(k_\rho, z_1') = \xi_{2,3}^{TM}(k_\rho, z_2') \cdot \frac{\left[1 - R_{\cup 2}^{TM}\right]\left[1 - R_{\cup 1}^{TM} e^{i2k_{1z}(d_0 - z_1')}\right]}{\left[1 - R_{\cup 1}^{TM} e^{i2k_{1z}h_1}\right]\left[1 - R_{\cup 2}^{TM} e^{i2k_{2z}h_2}\right]} \cdot e^{ik_{1z}(z_1' - d_1)} e^{ik_{2z}h_2} \tag{41}$$

where $\eta_l = \sqrt{\mu_l/\epsilon_l}$ and $z_2' = d_2$.

For source and observer are in region 1 (assuming $z > z'$), the expressions are

$$\xi_{1,1}^{TM}(k_\rho, z, z') = -\frac{\eta_1}{2}\frac{k_{1z}}{k_1}\frac{\left[1 - R_{\cup 1}^{TM} e^{i2k_{1z}(d_0 - z)}\right]\left[1 - R_{\cap 1}^{TM} e^{i2k_{1z}(z' - d_1)}\right]}{1 - R_{\cup 1}^{TM} R_{\cap 1}^{TM} e^{i2k_{1z}h_1}} e^{ik_{1z}(z - z')} \tag{42a}$$

$$\xi_{1,1}^{TE}(k_\rho, z, z') = -\frac{\eta_1}{2}\frac{k_1}{k_{1z}}\frac{\left[1 + R_{\cup 1}^{TE} e^{i2k_{1z}(d_0 - z)}\right]\left[1 + R_{\cap 1}^{TE} e^{i2k_{1z}(z' - d_1)}\right]}{1 - R_{\cup 1}^{TE} R_{\cap 1}^{TE} e^{i2k_{1z}h_1}} e^{ik_{1z}(z - z')}. \tag{42b}$$

For an observer in region 2 and source in region 1, the expressions are

$$\xi_{2,1}^{TM}(k_\rho, z, z') = -\frac{\eta_1}{2}\frac{k_{1z}}{k_1}\frac{\left[1 - R_{\cap 1}^{TM}\right]\left[1 - R_{\cap 2}^{TM} e^{i2k_{2z}(z - d_2)}\right]\left[1 - R_{\cup 1}^{TM} e^{i2k_{1z}(d_0 - z')}\right]}{\left[1 - R_{\cup 1}^{TM} R_{\cap 1}^{TM} e^{i2k_{1z}h_1}\right]\left[1 - R_{\cap 2}^{TE} e^{i2k_{2z}h_2}\right]} e^{ik_{1z}(z' - d_1)} e^{ik_{2z}(d_1 - z)} \tag{43a}$$

$$\xi_{2,1}^{TE}(k_\rho, z, z') = -\frac{\eta_1}{2}\frac{k_1}{k_{1z}}\frac{\left[1 + R_{\cap 1}^{TE}\right]\left[1 + R_{\cap 2}^{TE} e^{i2k_{2z}(z - d_2)}\right]\left[1 + R_{\cup 1}^{TE} e^{i2k_{1z}(d_0 - z')}\right]}{\left[1 - R_{\cup 1}^{TE} R_{\cap 1}^{TE} e^{i2k_{1z}h_1}\right]\left[1 + R_{\cap 2}^{TE} e^{i2k_{2z}h_2}\right]} e^{ik_{1z}(z' - d_1)} e^{ik_{2z}(d_1 - z)} \tag{43b}$$

By reciprocity, $\xi_{1,2}^{\alpha}(k_\rho, z, z') = \xi_{2,1}^{\alpha}(k_\rho, z', z)$ (α = TM,TE). For source and observer in region 2 (assuming $z > z'$), the expressions are

$$\xi_{2,2}^{TM}(k_\rho, z, z') = -\frac{\eta_2}{2}\frac{k_{2z}}{k_2}\frac{\left[1 - R_{\cup 2}^{TM} e^{i2k_{2z}(d_1 - z)}\right]\left[1 - R_{\cap 2}^{TM} e^{i2k_{2z}(z' - d_2)}\right]}{1 - R_{\cup 2}^{TM} R_{\cap 2}^{TM} e^{i2k_{2z}h_2}} e^{ik_{2z}(z - z')} \tag{44a}$$

$$\xi_{2,2}^{TE}(k_\rho, z, z') = -\frac{\eta_2}{2}\frac{k_2}{k_{2z}}\frac{\left[1 + R_{\cup 2}^{TE} e^{i2k_{2z}(d_1 - z)}\right]\left[1 + R_{\cap 2}^{TE} e^{i2k_{2z}(z' - d_2)}\right]}{1 - R_{\cup 2}^{TE} R_{\cap 2}^{TE} e^{i2k_{2z}h_2}} e^{ik_{2z}(z - z')} \tag{44b}$$

The generalized reflection coefficients, $R_{\cup l}^{\alpha}$ and $R_{\cap l}^{\alpha}$, at the upper and lower boundaries, respectively, of layer l, are given by the following recursion relations

$$R_{\cup l}^{\alpha} = \frac{R_{l(l-1)}^{\alpha} + R_{\cup(l-1)}^{\alpha} e^{i2k_{(l-1)z}h_{l-1}}}{1 + R_{l(l-1)}^{\alpha} R_{\cup(l-1)}^{\alpha} e^{i2k_{(l-1)z}h_{l-1}}} \tag{45a}$$

$$R_{\cap l}^{\alpha} = \frac{R_{l(l+1)}^{\alpha} + R_{\cap(l+1)}^{\alpha} e^{i2k_{(l+1)z}h_{l+1}}}{1 + R_{l(l+1)}^{\alpha} R_{\cap(l+1)}^{\alpha} e^{i2k_{(l+1)z}h_{l+1}}} \tag{45b}$$

where $R_{\cup 0}^{TE} = R_{\cup 0}^{TM} = 0$ and $R_{\cap 3}^{TE} = -1$ and $R_{\cap 3}^{TM} = 1$. The Fresnel reflection coefficients $R_{l(l\pm1)}^{TE}$ and $R_{l(l\pm1)}^{TM}$ are defined by

$$R_{l(l\pm1)}^{TE} = \frac{\mu_{(l\pm1)}k_{lz} - \mu_l k_{(l\pm1)z}}{\mu_{(l\pm1)}k_{lz} + \mu_l k_{(l\pm1)z}} \tag{45a}$$

$$R_{(l\pm1)}^{TM} = \frac{\epsilon_{(l\pm1)}k_{lz} - \epsilon_l k_{(l\pm1)z}}{\epsilon_{(l\pm1)}k_{lz} + \epsilon_l k_{(l\pm1)z}}. \tag{46b}$$

Acknowledgment

The authors would like to acknowledge and express their gratitude to Dr. Robert M. Sorbello at COMSAT Laboratories for providing the opportunity to perform the experimental work. We would also like to thank Henry B. Williams for his laboratory assistance.

References

[1] K. R. Carver and J. W. Mink, "Microstrip antenna technology," *IEEE Trans. Antennas Propagat.*, vol. AP-29, pp. 2-23, Jan. 1981.

[2] H. G. Oltman, "Electromagnetically coupled microstrip dipole antenna elements," in *Proc. 8th European Microwave Conf.*, Paris, 1977, pp. 281-285.

[3] P. S. Hall, C. Wood, and C. Garrett, "Wide bandwidth microstrip antennas for circuit integration," *Electron. Lett.*, vol. 15, no. 15, p. 458-460, 19 July 1979.

[4] A. Sabban, "A new broadband stacked two-layer microstrip antenna," in *1983 IEEE Antennas Propagat. Soc. Int. Symp. Dig.*, June 1983, pp. 63-66.

[5] C. H. Chen, A. Tulintseff, and R. M. Sorbello, "Broadband two-layer microstrip antenna," in *1984 IEEE Antennas Propagat. Soc. Int. Symp. Dig.*, June 1984, pp. 251-254.

[6] A. N. Tulintseff, "Experiment and analysis of a circularly polarized electromagnetically coupled microstrip antenna," S.M. thesis, Massachusetts Inst. Technol., Cambridge, MA, Feb. 1985.

[7] R. Q. Lee, K. F. Lee, and J. Bobinchak, "Characteristics of a two-layer electromagnetically coupled rectangular patch antenna," *Electron. Lett.*, vol. 23, no. 20, pp. 1070-1073, Sept. 24, 1987.

[8] S. A. Long and M. D. Walton, "A dual-frequency stacked circular-disc antenna," *IEEE Trans. Antennas Propagat.*, vol. AP-27, pp. 270-273, Mar. 1979.

[9] J. S. Dahele, K.-F. Lee, and D. P. Wong, "Dual-frequency stacked annular-ring microstrip antenna," *IEEE Trans. Antennas Propagat.*, vol. AP-35, pp. 1281-1285, Nov. 1987.

[10] K. Araki, H. Ueda, and T. Masayuki, "Numerical analysis of circular disk microstrip antennas with parasitic elements," *IEEE Trans. Antennas Propagat.*, vol. AP-34, pp. 1390-1394, Dec. 1986.

[11] A. N. Tulintseff, S. M. Ali, and J. A. Kong, "Resonant frequencies of stacked circular microstrip antennas," submitted for publication.

[12] A. N. Tulintseff and R. M. Sorbello, "Current and radiation fields of electromagnetically coupled microstrip antennas," in *1987 IEEE Int. Symp. Dig., Antennas Propagat.*, vol. 2, June 1987, pp. 928-931.

[13] R. Kastner, E. Heyman, and A. Sabban, "Spectral domain iterative analysis of single- and double-layered microstrip antennas using the conjugate gradient algorithm," *IEEE Trans. Antennas Propagat.*, vol. 36, pp. 1204-1212, Sept. 1988.

[14] A. Reineix and B. Jecko, "Analysis of microstrip patch antennas using finite difference time domain method," *IEEE Trans. Antennas Propagat.*, vol. 37, pp. 1361-1369, Nov. 1989.

[15] S. Yano and A. Ishimaru, "A theoretical study of the input impedance of a circular microstrip disk antenna," *IEEE Trans. Antennas Propagat.*, vol. AP-29, pp. 77-83, Jan. 1981.

[16] W. C. Chew and J. A. Kong, "Analysis of a circular microstrip disk antenna with a thick dielectric substrate," *IEEE Trans. Antennas Propagat.*, vol. AP-29, pp. 68-76, Jan. 1981.

[17] S. M. Ali, W. C. Chew, and J. A. Kong, "Vector Hankel transform analysis of annular-ring microstrip antenna," *IEEE Trans. Antennas Propagat.*, vol. AP-30, pp. 637-644, July 1982.

[18] T. M. Habashy, J. A. Kong, and W. C. Chew, "Resonance and radiation of the elliptic disk microstrip structure, Part I: Formulation," *IEEE Trans. Antennas Propagat.*, vol. AP-35, pp. 877-886, Aug. 1987.

[19] D. M. Pozar, "Input impedance and mutual coupling of rectangular microstrip antennas," *IEEE Trans. Antennas Propagat.*, vol. AP-23, pp. 1191-1196, Nov. 1982.

[20] T. M. Habashy, S. M. Ali, and J. A. Kong, "Impedance parameters and radiation pattern of two coupled circular microstrip disk antennas," *J. Math. Phys.*, vol. 54, no. 2, pp. 493-506, Feb. 1983.

[21] K. R. Carver, "Input impedance to probe-fed microstrip antennas," in *1980 IEEE Int. Symp. Dig.—Antennas Propagat.*, vol. 2, June 1980, pp. 617-620.

[22] J. T. Aberle and D. M. Pozar, "Analysis of infinite arrays of probe-fed rectangular microstrip patches using a rigorous feed model," *Proc. Inst. Elec. Eng.*, vol. 136, pt. H, no 2, pp. 110-119, Apr. 1989.

[23] M. A. Blischke, E. J. Rothwell, and K. M. Chen, "Receiving and scattering characteristics of circular patch antenna array," *J. Electromagn. Waves Appl.*, vol. 2, no. 3/4, pp. 353-378, 1988.

[24] M. C. Bailey and M. D. Deshpande, "Analysis of elliptical and circular microstrip antennas using moment method," *IEEE Trans. Antennas Propagat.*, vol. AP-33, pp. 9054-9059, Sept. 1985.

[25] S. Pinhas, S. Shtrikman, and D. Treves, "Moment-method solution of the center-fed microstrip disk antenna invoking feed and edge current singularities," *IEEE Trans. Antennas Propagat.*, vol. 37, pp. 1516-1522, Dec. 1989.

[26] M. Davidovitz and Y. T. Lo, "Input impedance of a probe-fed circular microstrip antenna with thick substrate," *IEEE Trans. Antennas Propagat.*, vol. AP-34, pp. 905-911, July 1986.

[27] W. L. Weeks, *Antenna Engineering*. New York: McGraw-Hill, 1968.

[28] W. C. Chew and T. M. Habashy, "The use of vector transforms in solving some electromagnetic scattering problems," *IEEE Trans. Antennas Propagat.*, vol. AP-34, pp. 871-879, July 1986.

[29] I. S. Gradshteyn and I. M. Ryzhik, *Table of Integrals, Series, and Products*. New York: Academic, 1965.

[30] M. Abramowitz and I. A. Stegun, *Handbook of Mathematical Functions*. Nat. Bur. Stand., 1964.

Ann N. Tulintseff was born in Seattle, WA, on April 23, 1961. She received the S.B., S.M., and Ph.D. degrees from the Massachusetts Institute of Technology, Cambridge, in 1985 and 1990, respectively.

During her graduate work, she held both Teaching and Research Assistantships. In 1986, she received the Frederick C. Hennie III Award for *Excellence in Teaching* and was appointed the position Instructor-G in the Department of Electrical Engineering and Computer Science. Her area of interest is electromagnetic wave theory and applications, with particular interest in microstrip antennas, microwave and millimeter wave antennas and circuit components, and wave propagation in layered media.

Dr. Tulintseff is a member of Eta Kappa Nu and Tau Beta Pi.

Sami M. Ali (M'79-SM'86), for a photograph and biography please see page 731 of the May 1990 issue of this TRANSACTIONS.

Jin Au Kong (S'65-M'69-SM'74-F'85), for a photograph and biography please see page 1149 of the September 1989 issue of this TRANSACTIONS.

Journal of Electromagnetic Waves and Applications, Vol. 5, No. 7, 701-714, 1991

Analysis of Diffraction from Chiral Gratings

S. H. Yueh and J. A. Kong

Department of Electrical Engineering
and Computer Science
Research Laboratory of Electronics
Massachusetts Institute of Technology
Cambridge, MA 02139, USA

Abstract– The coupled-wave theory is generalized to analyze the diffraction of waves by chiral gratings for arbitrary angles of incidence and polarizations. Numerical results are illustrated for the Stokes parameters of diffracted Floquet modes versus the thickness of chiral gratings with various chiralities. Both horizontal and vertical incidences are considered for illustration. The diffracted waves from chiral gratings are in general elliptically polarized; and in some particular instances, it is possible for chiral gratings to convert a linearly polarized incident field into two nearly circularly polarized Floquet modes propagating in different directions.

I. INTRODUCTION

There has been considerable interest in the theoretical study of scattering from chiral media. A detailed account regarding the chiral medium (or optical activity) and some suggested applications can be found in [1–3]. Chiral medium characterized by a biisotropic constitutive relation is a special case of the bianisotropic medium whose electromagnetic properties have been extensively studied by Kong [4,5]. Jaggard et al. [6] studied the propagation of electromagnetic waves through a random collection of short helices and demonstrated the physical basis of chirality. Recently, Bassiri et al. [1] analyzed the reflection and transmission of waves from a half-space chiral medium. Viitanen et al. [7] solved the eigensolutions for the reflection of waves by the interface of two chiral half-spaces. Jaggard et al. [2] analyzed the propagation of electromagnetic waves in periodic chiral structures under the weak coupling approximation for the case that the wave is normally incident on a chiral slab with the fringes parallel to the interface.

Periodic gratings have also been the object of extensive research through the years because of its many applications in distributed feedback laser, integrated optics, acousto-optics, quantum electronics, and holography. For the analysis of wave diffraction by periodic surface gratings, methods including the method of moments [8,9] and extended boundary condition method [10] are rigorous and in general computationally efficient. For the analysis of periodic slanted dielectric gratings, a rigorous coupled-wave method has been developed [11] and generalized to anisotropic gratings by [12,13].

In this paper, we present a generalization of the coupled-wave method to investigate the diffraction of electromagnetic waves by a periodic chiral grating with

the fringes allowed to be slanted. The coupled-wave approach writes the fields inside the grating region by Fourier series expansions and converts the Maxwell's equations into a set of coupled first-order differential equations for the Fourier coefficients. This system of equations is solved by the state variable method which gives the eigenmodes of fields inside the grating. Subsequently, the fields inside the grating are expanded by these eigenmodes and the unknown coefficients of the diffracted Floquet modes outside the grating are solved by matching the boundary conditions on the interfaces.

II. COUPLED WAVE THEORY

Consider the configuration (Fig. 1) that a plane wave with the time harmonic dependence $[\exp(-i\omega t)]$ impinges on a periodic chiral grating. The electric field of the incident wave is given by

$$\overline{E}_i = \hat{e}_i \exp(\overline{k}_i \cdot \overline{r}) \tag{1}$$

having the incident wave vector $\overline{k}_i$ defined as

$$\overline{k}_i = \hat{x} k_{xi} + \hat{y} k_{yi} - \hat{z} k_{zi} \tag{2}$$

$$k_{xi} = k \sin\theta \cos\phi \tag{3a}$$

$$k_{yi} = k \sin\theta \sin\phi \tag{3b}$$

$$k_{zi} = k \cos\theta \tag{3c}$$

where k is the wavenumber in free space.

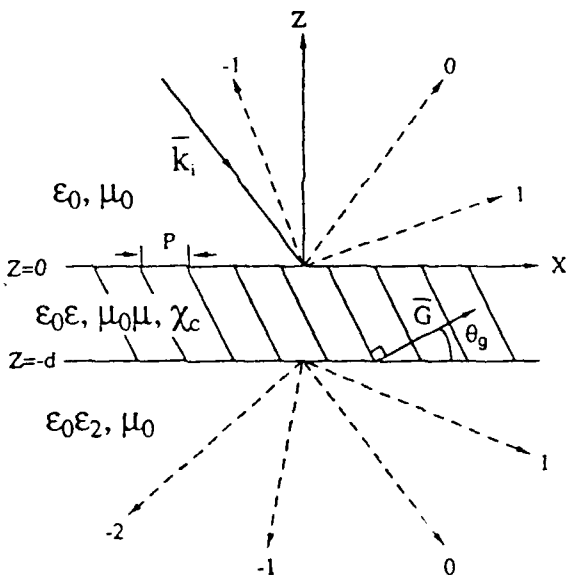

Figure 1. Configuration of the diffraction from a slanted modulated chiral grating.

Assuming that the periodicity of the grating is characterized by the grating vector

$$\overline{G} = \frac{2\pi}{p}(\hat{x} + \hat{z}\tan\phi_g), \quad -\pi/2 < \theta_g < \pi/2 \tag{4}$$

and expanding the diffracted fields outside of the grating region by the Floquet modes yield the following expressions for the total fields above and below the grating region, $\overline{E}$ and $\overline{E}_2$, respectively.

$$\overline{E} = \overline{E}_i + \sum_n \overline{R}_n \exp(i\overline{k}_n \cdot \overline{r}), \quad z > 0 \tag{5a}$$

$$\overline{E}_2 = \sum_n \overline{T}_n \exp(-inG_z d) \exp\left[i\overline{k}_{2n} \cdot (\overline{r} + d\hat{z})\right], \quad z < -d \tag{5b}$$

where

$$\overline{k}_n = \hat{x}k_{xn} + \hat{y}k_{yi} + \hat{z}k_{zn} \tag{6}$$

$$\overline{k}_{2n} = \hat{x}k_{xn} + \hat{y}k_{yi} - \hat{z}k_{2zn} \tag{7}$$

and k_{xn}, k_{zn}, and k_{2zn} are given by

$$k_{xn} = k_{xi} + nG_x \tag{8a}$$

$$k_{zn} = \sqrt{k^2 - k_{xn}^2 - k_{yi}^2} \tag{8b}$$

$$k_{2zn} = \sqrt{k_2^2 - k_{xn}^2 - k_{yi}^2} \tag{8c}$$

where the branch cut of the square root operation is chosen along the negative real axis of its argument.

Assuming that the medium in the grating region is characterized by the constitutive relations for chiral medium [14]

$$\overline{D} = \epsilon_0 \epsilon \overline{E} + i\chi_c \sqrt{\mu_0 \epsilon_0}\, \overline{H} \tag{9a}$$

$$\overline{B} = \mu_0 \mu \overline{H} - i\chi_c \sqrt{\mu_0 \epsilon_0}\, \overline{E} \tag{9b}$$

where ϵ and μ are the relative permittivity and permeability, and χ_c characterizes the chirality or handedness of the chiral medium. χ_c is a dimensionless quantity and $\chi_c \ll 1$ denotes small chirality. The constitutive relations given by (9) can be related to the constitutive relations [2] by the following transformations

$$\chi_c \to \xi_c \mu \sqrt{\mu_0/\epsilon_0}$$
$$\epsilon \to \epsilon + \xi_c^2 \mu \mu_0/\epsilon_0$$

where ξ_c is the chirality admittance.

In the constitutive relations given by (9), ϵ, μ, and ξ_c are all assumed to be periodic in the direction of grating vector $\overline{G}$ so that the following Fourier series expansion of the grating parameters can be defined as

$$\epsilon = \sum \epsilon_n \exp(in\overline{G} \cdot \overline{r}) \tag{10a}$$

$$\mu = \sum \mu_n \exp(in\overline{G} \cdot \overline{r}) \tag{10b}$$

$$\chi_c = \sum \chi_n \exp(in\overline{G} \cdot \overline{r}) \tag{10c}$$

$$\frac{\chi_c}{\chi_c^2 - \mu\epsilon} = \sum \xi_n \exp(in\overline{G} \cdot \overline{r}) \tag{10d}$$

$$\frac{\mu}{\chi_c^2 - \mu\epsilon} = \sum \gamma_n \exp(in\overline{G} \cdot \overline{r}) \tag{10e}$$

$$\frac{\epsilon}{\chi_c^2 - \mu\epsilon} = \sum \zeta_n \exp(in\overline{G} \cdot \overline{r}) \tag{10f}$$

Substituting the constitutive relations, (9a) and (9b), into Maxwell's equations yields

$$\nabla \times \overline{E} = ik\mu\eta\overline{H} + k\chi_c\overline{E} \tag{11}$$

$$\nabla \times \eta\overline{H} = -ik\epsilon\overline{E} + k\chi_c\eta\overline{H} \tag{12}$$

where $\eta = \sqrt{\mu_0/\epsilon_0}$ represents the free space impedance.

For the coupled wave theory, electromagnetic fields inside the grating region $(0 > z > -d)$ are assumed to have the following series expansions

$$\overline{E} = \sum \left[E_{xn}(z)\,\hat{x} + E_{yn}(z)\,\hat{y} + E_{zn}(z)\,\hat{z}\right] \exp(i\overline{\beta}_n \cdot \overline{r}) \tag{13a}$$

$$\overline{H} = \sum \left[H_{xn}(z)\,\hat{x} + H_{yn}(z)\,\hat{y} + H_{zn}(z)\,\hat{z}\right] \exp(i\overline{\beta}_n \cdot \overline{r}) \tag{13b}$$

where

$$\overline{\beta}_n = \hat{x}k_{xn} + \hat{y}k_{yi} + \hat{z}nG_z \tag{14}$$

Substituting (10) and (13) into (11) and (12) yields the following coupled wave equations

$$\frac{dE_{xn}}{dz} = -inG_zE_{xn} + ik\sum_m \mu_{n-m}\eta H_{ym} + k\sum_m \chi_{n-m}E_{ym} + ik_{xn}E_{zn} \tag{15a}$$

$$\frac{dE_{yn}}{dz} = -inG_zE_{yn} - ik\sum_m \mu_{n-m}\eta H_{xm} - k\sum_m \chi_{n-m}E_{xm} + ik_{yi}E_{zn} \tag{15b}$$

$$\frac{d\eta H_{xn}}{dz} = -inG_z\eta H_{xn} - ik\sum_m \epsilon_{n-m}E_{ym} + k\sum_m \chi_{n-m}\eta H_{ym} + ik_{xn}\eta H_{zn} \tag{15c}$$

$$\frac{d\eta H_{yn}}{dz} = -inG_z\eta H_{yn} + ik\sum_m \epsilon_{n-m}E_{xm} - k\sum_m \chi_{n-m}\eta H_{xm} + ik_{yi}\eta H_{zn} \tag{15d}$$

and

$$E_{zn} = \sum_m \left[i\xi_{n-m}\left(\frac{k_{xm}}{k}E_{ym} - \frac{k_{yi}}{k}E_{xm}\right) + \gamma_{n-m}\left(\frac{k_{xm}}{k}\eta H_{ym} - \frac{k_{yi}}{k}\eta H_{xm}\right)\right] \tag{16a}$$

$$\eta H_{zn} = \sum_m \left[-\zeta_{n-m}\left(\frac{k_{xm}}{k}E_{ym} - \frac{k_{yi}}{k}E_{xm}\right) + i\xi_{n-m}\left(\frac{k_{xm}}{k}\eta H_{ym} - \frac{k_{yi}}{k}\eta H_{xm}\right)\right] \tag{16b}$$

In deriving (16), the z components of $\overline{E}$ and $\overline{H}$ are first solved in terms of the z components of $\nabla \times \overline{E}$ and $\nabla \times \overline{H}$ using (11) and (12). Subsequently, (16) is obtained by substituting (13) into the resulting equations. Note that the chirality of the gratings can be considered small in (15a)–(15d) if

$$\epsilon,\ \mu \sim O(1) \gg \chi_c$$

On the other hand, if χ_c is of the order of one, then it would have significant amount of contribution.

By substituting (16) into (15), (15a)–(15d) can be recast into a matrix form as

$$\frac{d}{dz}V = AV \tag{17}$$

where

$$V = \begin{bmatrix} E_{zn} \\ E_{yn} \\ \eta H_{xn} \\ \eta H_{yn} \end{bmatrix} \tag{18}$$

and matrix A is the coupling matrix. Note that in the above equation vector V should be realized as containing the modes with all indices n's and in fact is an infinite dimensional vector.

The solutions to the coupled-wave equations can be expressed as

$$V = \sum_m c_m P_m \exp(\lambda_m z) = \sum_m c_m \begin{bmatrix} P_{1,nm} \\ P_{2,nm} \\ P_{3,nm} \\ P_{4,nm} \end{bmatrix} \exp(\lambda_m z) \tag{19}$$

where P_m is the eigenvector corresponding to the eigenvalue λ_m for the matrix A. $P_{1,nm}$, $P_{2,nm}$, $P_{3,nm}$, and $P_{4,nm}$ correspond to E_{xn}, E_{yn}, ηH_{xn}, and ηH_{yn}, respectively. In practice, the series expansions will be truncated so that matrix A becomes a finite matrix. Eigenvalues and eigenvectors of the truncated matrix are solved by using a computer library program EIGCC in the International Mathematics and Statistics Library (IMSL). c_m's are the unknown coefficients to be determined from boundary conditions.

Note that Gauss' law for the source-free region gives two additional equations

$$\bar{k}_n \cdot \bar{R}_n = 0 \tag{20a}$$

$$\bar{k}_{2n} \cdot \bar{T}_n = 0 \tag{20b}$$

Furthermore, the continuity of the tangential components of electric and magnetic fields on the upper and lower interfaces of gratings yields the following equations:

$$E_{xn}(0) = e_x \delta_{n0} + R_{xn} \tag{21}$$

$$E_{yn}(0) = e_y \delta_{n0} + R_{yn} \tag{22}$$

$$k\eta H_{xn}(0) = \delta_{n0}(k_{yi} e_z + k_{zi} e_y) + (k_{yi} R_{zn} - k_{zn} R_{yn}) \tag{23}$$

$$k\eta H_{yn}(0) = \delta_{n0}(-k_{xi} e_z - k_{zi} e_x) + (k_{zn} R_{xn} - k_{xn} R_{zn}) \tag{24}$$

$$E_{xn}(-d) = T_{xn} \tag{25}$$

$$E_{yn}(-d) = T_{yn} \tag{26}$$

$$k\eta H_{xn}(-d) = k_{yi} T_{xn} + k_{2zn} T_{yn} \tag{27}$$

$$k\eta H_{yn}(-d) = -k_{2zn}T_{xn} - k_{xn}T_{zn} \tag{28}$$

where δ_{nm} is the Kronecker delta and e_x, e_y, and e_z are the x, y, and z components of $\hat{e}_i$ which defines the polarization of the incident electric field given by (1).

The above equations (20)–(28) can be used to solve all the unknowns. For example, if N modes are kept, there are $4N$ eigenvectors inside the grating region and $3N$ components for each of $\overline{R}_n$ and $\overline{T}_n$. Note that the total number of unknowns is $10N$ which equals the total number of equations. For the efficiency of numerical computation, the components of $\overline{R}_n$ and $\overline{T}_n$ are first expressed analytically in terms of c_m's. Thus (20)–(28) reduce to $4N$ equations for c_m's.

After $\overline{T}_n$ is solved, the horizontal and vertical components of the nth transmitted Floquet mode are defined as

$$E_h = \hat{h} \cdot \overline{T}_n \tag{29a}$$

$$E_v = \hat{v} \cdot \overline{T}_n \tag{29b}$$

where

$$\hat{h} = \frac{-k_{yi}\hat{x} + k_{xn}\hat{y}}{k_\rho} \tag{30a}$$

$$\hat{v} = \frac{k_{2zn}}{k_2}\frac{k_{xn}\hat{x} + k_{yi}\hat{y}}{k_\rho} + \frac{k_\rho}{k_2}\hat{z} \tag{30b}$$

$$k_\rho = \sqrt{k_{xn}^2 + k_{yi}^2} \tag{31}$$

and k_2 is the wavenumber of lower half-space.

Similarly, the horizontal and vertical components of the nth reflected Floquet mode are defined as

$$E_h = \hat{h} \cdot \overline{R}_n \tag{32a}$$

$$E_v = \hat{v} \cdot \overline{R}_n \tag{32b}$$

where $\hat{h}$ is still defined by (30a) and $\hat{v}$ is given as

$$\hat{v} = -\frac{k_{zn}}{k}\frac{k_{xn}\hat{x} + k_{yi}\hat{y}}{k_\rho} + \frac{k_\rho}{k}\hat{z} \tag{33}$$

The diffraction efficiency is defined as the ratio of the z component of the power carried by Floquet modes to the z component of the power of the incident wave.

$$DE_{rn} = \mathrm{Re}(k_{zn}/k_{zi})|R_n|^2 \tag{34a}$$

$$DE_{tn} = \mathrm{Re}(k_{2zn}/k_{zi})|T_n|^2 \tag{34b}$$

For lossless gratings, the sum of the efficiencies for all the propagating modes should be unity. For the numerical examples illustrated in this paper, the coupled wave method gives highly convergent results where the computed total diffraction efficiency deviates from 1 by 0.02% for the worst case. Note that a VAX workstation is used for our numerical computation.

III. NUMERICAL RESULTS AND DISCUSSIONS

In this section, numerical examples for the effects of chirality are illustrated for the polarization states of the waves diffracted by gratings with rectangular grooves (Fig. 2), even though the theory developed in Section II can be applied for much more general cases. However, gratings with sinusoidal modulation have also been analyzed but the features observed are essentially the same as those of rectangular modulations presented in this paper.

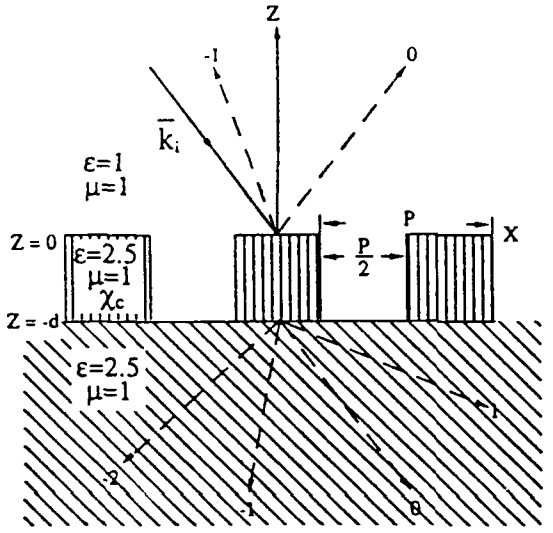

Figure 2. Wave diffraction from a rectangular chiral grating.

Figure 2 shows the geometry of the rectangular grating for the cases presented. For all the cases considered, P equals λ which is the electromagnetic wavelength in free space. The relative permittivity of the substrate below the corrugated region is $\epsilon_2 = 2.5$, and the relative permeability is one for all regions. The chirality parameter (χ_c) is chosen as 0, 0.188, and 0.377 to illustrate the effects of chirality.

Two sets of incident angles (θ, ϕ) are selected: (30 deg, 0 deg) and (35.26 deg, 30 deg). The former one corresponds to the situation that the incident direction is perpendicular to the ruling direction; whereas the latter one is not. In either case the incident angle is chosen such that

$$k_{zn}\Big|_{n=-1} = -k_{zi} \tag{35}$$

In other words, the wave is incident at the first Bragg angle. For the cases studied in this paper, most of the power are carried by the -1 and 0 transmitted Floquet modes.

Hence only the diffraction efficiency and polarization state of these two dominant modes are illustrated. In order to present the polarization state of diffracted Floquet modes in a compact format, orientation (α) and ellipticity (β) angles (Fig. 3) are utilized to express the transmitting and receiving polarization states. Here, the definitions from [1] are adopted. Therefore, horizontal (H) and vertical (V) polarization states will have zero degree ellipticity angles, with orientation angles of 0 deg and 90 deg. Right and left polarization states are orientation independent with ellipticity angles of 45 deg and -45 deg, respectively. In addition, $0\,\text{deg} \leq \alpha \leq 180\,\text{deg}$ and $-45\,\text{deg} \leq \beta \leq 45\,\text{deg}$.

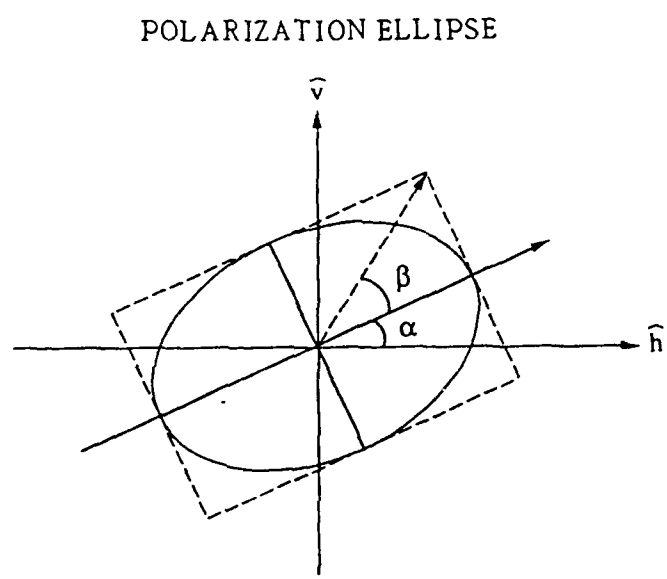

Figure 3. Polarization ellipse. α and β represent orientation and ellipticity angles, respectively.

A general polarization vector,

$$\overline{P} = \begin{bmatrix} E_h \\ E_v \end{bmatrix} = \begin{bmatrix} |E_h| \exp(i\phi_h) \\ |E_v| \exp(i\phi_v) \end{bmatrix} \tag{36}$$

written in terms of horizontal ($\hat{h}$) and vertical ($\hat{v}$) vector components, can be transformed into a normalized Stokes vector as follows

$$\begin{bmatrix} S_0 \\ S_1 \\ S_2 \\ S_3 \end{bmatrix} = \begin{bmatrix} |E_h|^2 + |E_v|^2 \\ |E_h|^2 - |E_v|^2 \\ 2|E_h||E_v| \cos\phi \\ 2|E_h||E_v| \sin\phi \end{bmatrix} = (|E_h|^2 + |E_v|^2) \begin{bmatrix} 1 \\ \cos 2\beta \cos 2\alpha \\ \cos 2\beta \sin 2\alpha \\ \sin 2\beta \end{bmatrix} \tag{37}$$

where $\phi = \phi_v - \phi_h$. Using this equation, the angles α and β are obtained.

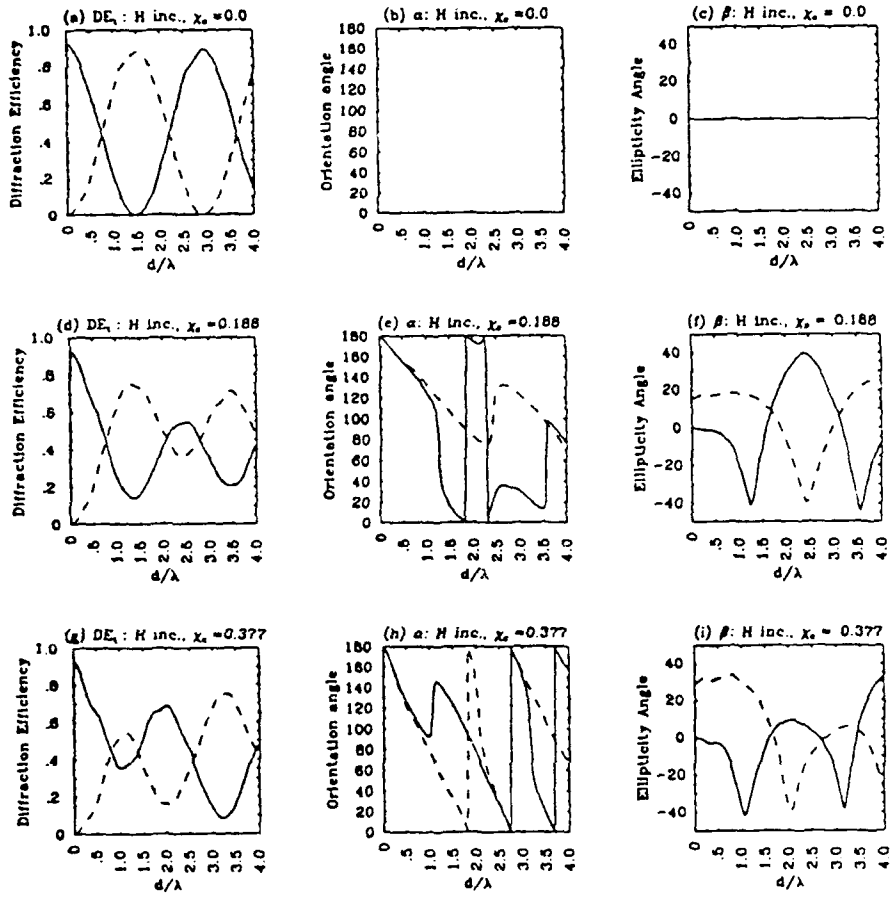

Figure 4. Diffraction efficiencies and Stokes parameters of transmitted Floquet modes 0 and -1 for horizontal polarization incidence. $\theta = 30\,\text{deg}$ and $\phi = 0\,\text{deg}$. (a)-(c): $\chi_c = 0$; (d)-(f): $\chi_c = 0.188$; (g)-(i): $\chi_c = 0.377$. Solid and dashed lines correspond to Floquet mode 0 and -1, respectively.

Figures 4 and 5 illustrate the Stokes parameters of the transmitted 0 and -1 Floquet modes versus the thickness of rectangular gratings (d), respectively, for horizontally and vertically polarized incidences. The incident angle is $\theta = 30\,\text{deg}$ and $\phi = 0\,\text{deg}$. For the case of zero chirality (achiral grating) and horizontal incidence [Fig. 4(a)-(c)] which has been studied in [15], the diffraction efficiencies oscillate when the thickness of the grating increases. Note that for $\chi_c = 0$ the diffracted polarizations remain horizontally polarized ($\alpha = 0\,\text{deg}$ and $\beta = 0\,\text{deg}$) in Figs. 4(a)-(c) and vertically polarized ($\alpha = 0\,\text{deg}$ and $\beta = 0\,\text{deg}$) in Figs. 5(a)-(c). When the grating material becomes chiral ($\chi_c \neq 0$), the diffracted Floquet modes are in general elliptically polarized.

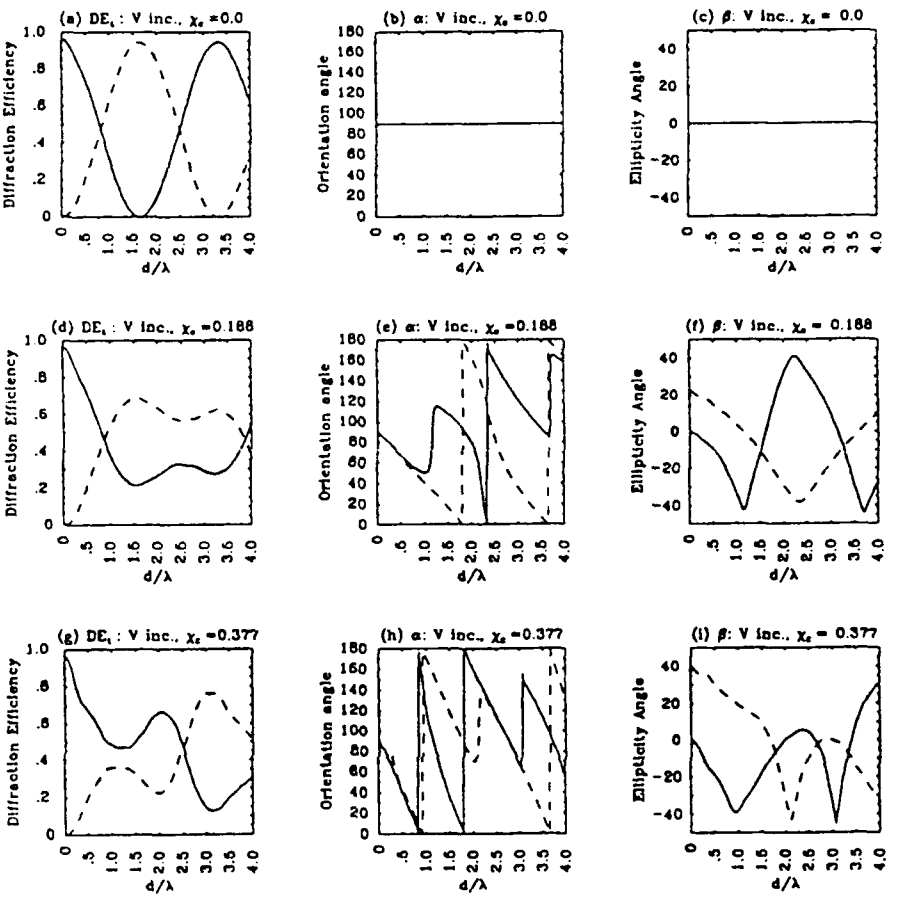

Figure 5. Diffraction efficiencies and Stokes parameters of transmitted Floquet modes 0 and -1 for vertical polarization incidence. $\theta = 30\,\text{deg}$ and $\phi = 0\,\text{deg}$.(a)-(c): $\chi_c = 0$; (d)-(f): $\chi_c = 0.188$;(g)-(i): $\chi_c = 0.377$. Solid and dashed lines correspond to Floquet mode 0 and -1, respectively.

Figures 6 and 7 represent the cases that the incident direction is not perpendicular to the ruling direction ($\phi = 30\,\text{deg}$ and $\theta = 35.26\,\text{deg}$), respectively, for horizontal and vertical incidence. All the diffracted modes are generally elliptically polarized. In contrast to the cases of $\phi = 0\,\text{deg}$ [Figs. 4 and 5 (a)-(c)], Figs. 6(c) and 7(c) show that the Floquet modes are elliptically polarized for achiral gratings. This is due to the fact that horizontal and vertical polarizations are coupled for an oblique incidence ($\phi \neq 0$).

Several features regarding the effects of chirality can be observed in all cases. The chirality introduces more coupling between 0 and -1 modes, thus resulting in

more even distribution of the power between these two modes, therefore, smaller fluctuation for the diffraction efficiencies as a function of thickness d. In addition, like the diffraction efficiencies, the ellipticity angles also show oscillations [(f) and (i) of Figs. 4–7] as the chirality is introduced. Moreover, at some particular instances, it is possible for chiral gratings to convert a linearly polarized incident field into two nearly circularly polarized Floquet modes propagating in different directions. For example, for the case of $\chi_c = 0.188\,(\xi_c = 0.0005\,\text{mho})$, when the depth of the grating is about $2.4\,\lambda$, both modes are nearly circularly polarized ($\beta = \pm 45\,\text{deg}$).

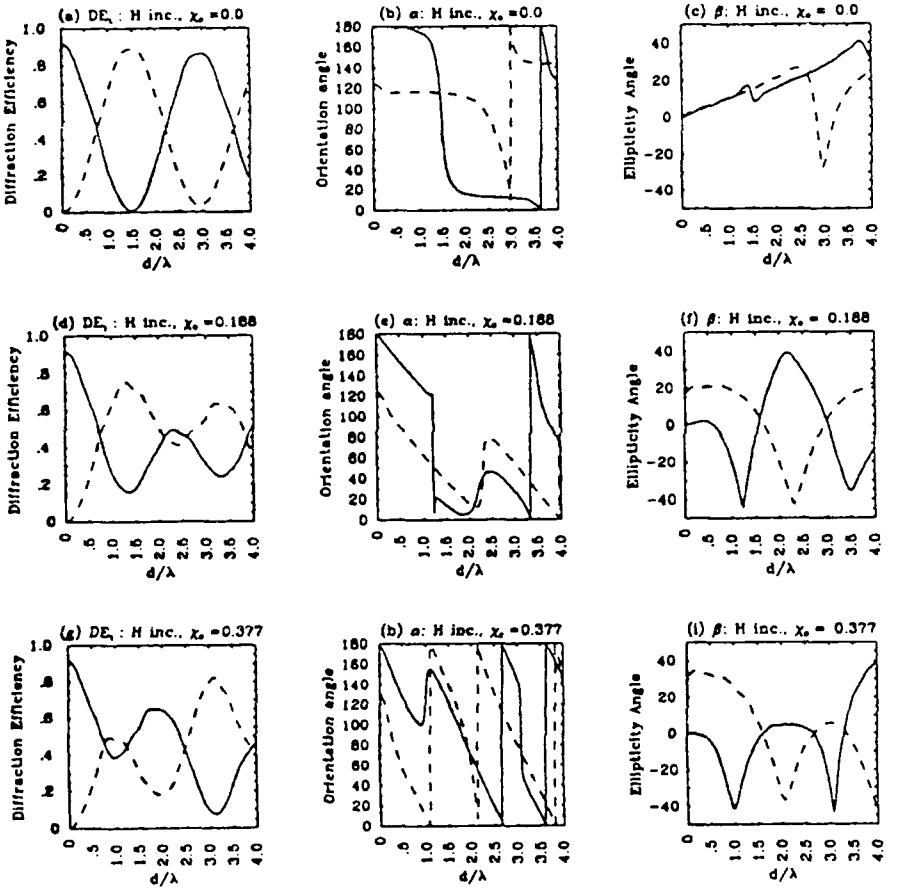

Figure 6. Diffraction efficiencies and Stokes parameters of transmitted Floquet modes 0 and -1 for horizontal polarization incidence. $\theta = 35.26\,\text{deg}$ and $\phi = 30\,\text{deg}$. (a)-(c): $\chi_c = 0$; (d)-(f): $\chi_c = 0.188$; (g)-(i): $\chi_c = 0.377$. Solid and dashed lines correspond to Floquet mode 0 and -1, respectively.

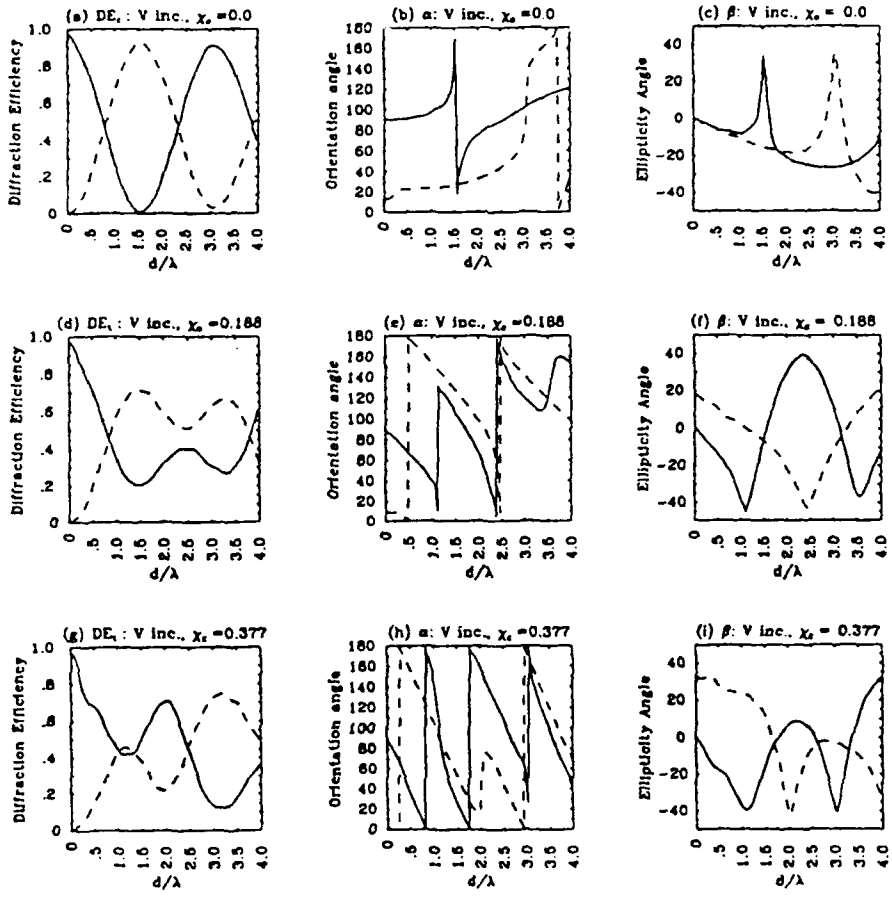

Figure 7. Diffraction efficiencies and Stokes parameters of transmitted Floquet modes 0 and -1 for vertical polarization incidence. $\theta = 35.26\,\text{deg}$ and $\phi = 30\,\text{deg}$. (a)-(c): $\chi_c = 0$; (d)-(f): $\chi_c = 0.188$; (g)-(i): $\chi_c = 0.377$. Solid and dashed lines correspond to Floquet mode 0 and -1, respectively.

Note that the orientation angle of the diffracted waves in general has a neg ative slope versus thickness d of the grating in the cases studied ($\chi_c > 0$ right-hand chiral). In fact when chirality χ_c becomes negative (left-hand chiral the curves of orientation angles become the mirror images of the correspondi right-hand chiral cases with respective to $\alpha = 90\,\text{deg}$. The phenomenon observ can be explained by studying how the orientation of waves rotates as it propagat through a chiral slab [3]. Neglecting the reflection from the boundaries, a linea polarized wave impinging on a chiral slab can be divided into two circularly pol

ized waves of opposite handedness. For the case of right-hand chiral medium, the right-hand-circularly polarized wave travels slower than the left-hand-circularly polarized wave. If we trace the polarization of the total field along the propagation path at any given time, then the resulting polarization trajectory would circulate in the clockwise direction. In other words, the orientation of the transmitted wave will decrease if the thickness of the chiral slab increases. For the case of a wave diffracted by a chiral grating, the same argument applies for each Floquet mode. When the wave enters gratings, Bragg diffraction will split it into Floquet modes propagating in several directions, the orientation of each mode will rotate in the clockwise direction for the case of right-hand chirality. However, it should be noticed that for some particular thickness, the orientation of some Floquet mode has a fast transition [Figs. 4–7(e)] and may show an opposite trend, such as in Fig. 5(e) where the orientation of Floquet mode 0 increases instead of decreases near $d = 1.2\lambda$. Nevertheless, it can be observed that whenever there is a fast transition in the plots of the orientation angle versus depth, the corresponding Floquet mode is nearly circularly polarized, for example, Floquet mode 0 at d near 1.2λ in Figs. 4–7(f). It is known that the orientation of a circularly polarized wave can be arbitrary or undefined. Hence, it should not be surprised that the orientation exhibits a fast transition around the thickness where the waves are nearly circularly polarized. Also some of the fast jumps shown in the plots of orientation angles from 0 deg to 180 deg or the opposite are not important because 0 deg and 180 deg orientations represent essentially the same orientation.

IV. SUMMARY

In this paper, the diffraction of waves from chiral gratings is analyzed. The problem is formulated by the coupled wave method which gives highly convergent results for all the cases studied where the computed total diffraction efficiency is different from 1 by 0.02% for the worst case. It is shown that a grating of chiral medium is capable of not only dividing the power into different Floquet modes, but sometimes also making both dominant modes nearly circularly polarized in the cases studied.

ACKNOWLEDGMENTS

This work was supported by ARO Contract DAAL03-88-J-0057, NAVY-ONR N00014-90-J-1002, RADC Contract F19628-88-K-0013, ONR Contract N00014-89-J-1019, and the Joint Services Electronics Program under the Contract DAAL03-89-C-0001.

The Editor thanks N. Engheta, D. L. Jaggard, and A. Sihvola for reviewing the paper.

REFERENCES

1. Bassiri, S., C. H. Papas, and N. Engheta, "Electromagnetic wave propagation through a dielectric-chiral interface and through a chiral slab," *J. Opt. Soc. Am. A.*, Vol. 5, No. 9, 1450–1459, 1988.

2. Jaggard, D. L., N. Engheta, M. W. Kowarz, P. Pelet, J. C. Liu, and Y. Kim, "Periodic chiral structures," *IEEE Trans. Antennas Propagat.*, Vol. AP-37, No. 11, 1447–1452, 1989.
3. Engheta, N., and D. L. Jaggard, "Electromagnetic chirality and its applications," *IEEE Antennas Propagat. Society Newsletter*, Vol. 30, No. 5, 6–12, Oct. 1988.
4. Kong, J. A., *Electromagnetic Wave Theory*, Wiley Interscience, New York, 1986.
5. Kong, J. A., "Theorems of bianisotropic media," *Proc. IEEE*, Vol. 60, 1036–1046, 1972.
6. Jaggard, D. L., A. R. Mickelson, and C. H. Papas, "On electromagnetic waves in chiral media," *Applied Phys.*, Vol. 18, 211–216, 1979.
7. Viitanen, A. J., I. V. Lindell, A. H. Sihvola, and S. A. Tretyakov, "Eigensolutions for the reflection problem of the interface of two chiral half-space," *J. Opt. Soc. Am. A.*, Vol. 7, No. 4, 683–692, 1990.
8. Zaki, K. A., and A. R. Neureuther, "Scattering from a perfectly conducting surface with a sinusoidal height profile: TE polarization," *IEEE Trans. Antennas Propagat.*, Vol. AP-19, 208–214, 1971a.
9. Zaki, K. A., and A. R. Neureuther, "Scattering from a perfectly conducting surface with a sinusoidal height profile: TM polarization," *IEEE Trans. Antennas Propagat.*, Vol. AP-19, 747–751, 1971b.
10. Chuang, S. L., and J. A. Kong, "Wave scattering from a periodic dielectric surface for a general angle of incidence," *Radio Science*, 545–557, 1982.
11. Moharam, M. G., and T. K. Gaylord, "Three-dimensional vector coupled-wave analysis planar-grating diffraction," *J. Opt. Soc. Am.*, Vol. 73, No. 9, 1105–1112, 1983.
12. Rokushima, K., and J. Yamakito, "Analysis of anisotropic dielectric gratings," *J. Opt. Soc. Am.*, Vol. 73, No. 7, 901–908, 1983.
13. Glytsis, E. G., and T. K. Gaylord, "Rigorous three-dimensional coupled-wave diffraction analysis of single and cascaded anisotropic gratings," *J. Opt. Soc. Am.*, Vol. 4, No. 11, 2061–2080, 1987.
14. Sihvola, A. H., and I. V. Lindell, "Chiral Maxwell-Garnett mixing formula," *Electronics Letters*, Vol. 26, No. 2, 118–119, 1990.
15. Moharam, M. G., and T. K. Gaylord, "Diffraction analysis of dielectric surface-relief gratings," *J. Opt. Soc. Am.*, Vol. 72, No. 10, 1385–1392, 1982.

S. H. Yueh received the SB (1982) and SM (1984) from the Electrical Engineering Department of National Taiwan University, Taiwan, and the Ph.D. degree in electrical engineering in 1991 from Massachusetts Institute of Technology, Cambridge. His fields of interest are electromagnetics and remote sensing.

J. A. Kong is Professor of Electrical Engineering and Chairman of Area IV on Energy and Electromagnetic Systems in the Department of Electrical Engineering and Computer Science at the Massachusetts Institute of Technology in Cambridge, Massachusetts. His research interest is in the field of electromagnetic wave theory and applications. He has published 7 books and over 300 refereed journal and conference papers, and is the Editor of the Wiley Series in Remote Sensing, and Chief Editor of the Elsevier book series of Progress In Electromagnetics Research (PIER).

PROCEEDINGS REPRINT

SPIE—The International Society for Optical Engineering

Reprinted from

Digital Image Synthesis and Inverse Optics

9-13 July 1990
San Diego, California

Volume 1351

Inversion of permittivity and conductivity profiles employing transverse-magnetic polarized monochromatic data

T. M. Habashy*, M. Moldoveanu+, and J. A. Kong+

*Schlumberger-Doll Research
Old Quarry Road, Ridgefield, CT 06877-4108

+Department of Electrical Engineering and Computer Science
Massachusetts Institute of Technology, Cambridge, MA 02139

ABSTRACT

We present an inversion algorithm based on a recently developed inversion method referred to as the Renormalized Source-Type Integral Equation approach. The objective of this method is to overcome some of the limitations and difficulties of the iterative Born technique. It recasts the inversion, which is nonlinear in nature, in terms of the solution of a set of linear equations; however, the final inversion equation is still nonlinear. The derived inversion equation is an exact equation which sums up the iterative Neuman (or Born) series in a closed form and; thus, is a valid representation even in the case when the Born series diverges; hence, the name *Renormalized* Source-Type Integral Equation Approach.

1. INTRODUCTION

Most of the monochromatic profile inversion methods that exist in literature utilize an iterative Born approach in the implementation of the reconstruction process[1-8]. This approach does not work well at high frequencies or for the transverse-magnetic (TM) polarization, but appears to be useful only for the low frequency transverse-electric (TE) case. This is attributed to the fact that at high frequencies or in the case of the TM polarization, the inversion problem becomes highly nonlinear rendering perturbative approaches inappropriate.

In this paper we present an inversion algorithm based on a recently developed inversion method referred to as the Renormalized Source-Type Integral Equation approach[9,10]. The objective of this method is to overcome some of the limitations and difficulties of the above-mentioned iterative Born technique. This approach can be summarized in three simple steps. In the first step, the induced currents in the probed medium are determined from the known data on the surface of the medium by use of the source-type integral equation. Next, the field induced in the medium is computed from the induced currents. In the final step, the medium parameters are reconstructed from the induced currents and fields which were obtained in the previous two steps. This method recasts the inversion, which is nonlinear in nature, in terms of the solution of a set of linear equations; however, the final inversion equation is still nonlinear.

There are a number of apparent advantages to this scheme: i) it is applicable to TE, TM and hybrid polarizations, ii) there is no explicit frequency limitations, iii) by pre-storing the elements of the inversion operator (which depend only on the background medium and are independent of the unknown profile), the method does not require the solution to the full forward problem repeatedly as in the case of the Distorted Born approach and is therefore faster to implement, iv) it can be generalized to two-dimensional cases where the previous property becomes an attractive feature of the inversion, v) it allows, in some cases, the rigorous study of the degree of nonuniqueness involved in the inversion, a point of great importance in the design problem, and vi) it provides an inversion equation which has an

explicit dependence on the unknowns to be obtained in the inversion. This explicit dependence allows one to compute the derivatives of the response with respect to the unknowns in a closed form.. Associated with this approach, however, is the need to incorporate *a priori* information, such as the type of likely profiles, that are derived from means other than those supplied by measurement. The judicious use of such information allows us to overcome the non-uniqueness which is characteristic of all inversion problems.

Another advantage of this approach is that the inversion equation obtained is an exact equation. If approximations are to be made they will occur in the numerical methods employed in the solution of this inversion equation. Thus, the major virtue of our method is that the approximations to be used can be under good control and may be improved upon to an arbitrary degree. This is to be distinguished from other methods, e.g., Born inversion, ray tracing, etc., which are inherently approximate, often unstable and hard to improve when they give inaccurate results.

In this paper, the inversion scheme is demonstrated for the cases where the exciting source is of the dipole-type that generates only TE or TM polarized waves. The data required for inversion are the tangential components of the electric or magnetic fields at various locations on the probed medium's surface performed at a number of frequencies.

2. FORMULATION

We limit our analysis to the problem of profile inversion of a one-dimensional layered medium whose permittivity can vary as a function of depth in a planar stratified medium or as a function of radial distance in a cylindrically layered medium. For the sake of simplifying the analysis, we restrict ourselves to the planar stratified case where the medium is assumed to be z-stratified, i.e., the permittivity ε and the conductivity σ of the medium are functions of z only. The geometrical configuration of the problem is depicted in figure 1.

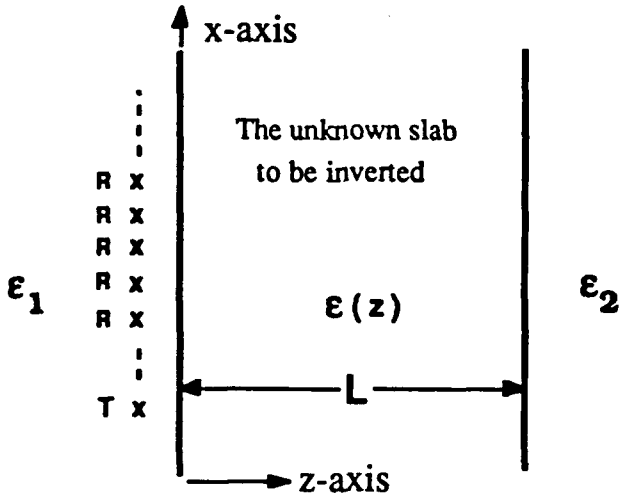

Figure 1. Geometrical configuration of the inversion problem.

The source is assumed to be localized, and without any loss of generality, the source characteristics can be chosen such that they excite either a purely transverse electric (TE) or transverse magnetic (TM) type of field. For the sake of further simplifying the analysis, we assume that the exciting TE source is an electric line current, situated at $x = 0$, $z = z_s$ and extending from $y = -\infty$ to $y = +\infty$. In this case, the nonvanishing field components are H_x, H_z and E_y which are functions of x and z only. For the TM

case, we assume the source to be a magnetic line current and, in this case, the nonvanishing field components are E_x, E_z and H_y.

In formulating the problem using the source-type integral equation, one assumes that the unknown inhomogeneous slab (extending from z = 0 to z = L) is embedded inside a known background medium ($\varepsilon_b(z)$) which is not necessarily homogeneous. The scattering from this inhomogeneous slab is then assumed to be produced by a volume distribution of currents induced inside the slab. The field can thus be decomposed into a superposition of two parts. The first part (E_{yb} for TE and H_{yb} for TM) is produced by the exciting source in the background medium. The second (E_{ys} for TE and H_{ys} for TM) represents the field scattered by the inhomogeneous slab and is given by the field produced by the volume currents induced inside the slab. Thus, for the TE polarization we have:

$$E_y = E_{yb} + E_{ys} \tag{1}$$

$$\nabla^2 E_{yb} + k_0^2 \varepsilon_b E_{yb} = 0 \tag{2a}$$

$$\nabla^2 E_{ys} + k_0^2 \varepsilon_b E_{ys} = -k_0^2 \delta\varepsilon E_y \tag{2b}$$

and for the TM polarization, we have:

$$H_y = H_{yb} + H_{ys} \tag{3}$$

$$\nabla^2 H_{yb} - \frac{\varepsilon_b'}{\varepsilon_b} \frac{\partial H_{yb}}{\partial z} + k_0^2 \varepsilon_b H_{yb} = 0 \tag{4a}$$

$$\nabla^2 H_{ys} - \frac{\varepsilon_b'}{\varepsilon_b} \frac{\partial H_{ys}}{\partial z} + k_0^2 \varepsilon_b H_{ys} = -k_0^2 \delta\varepsilon H_y + \left[\frac{\varepsilon'}{\varepsilon} - \frac{\varepsilon_b'}{\varepsilon_b} \right] \frac{\partial H_y}{\partial z} \tag{4b}$$

where

$$\delta\varepsilon = \varepsilon(z) - \varepsilon_b(z) \tag{5}$$

Using the Green's function formulation, eqs. (2b) and (4b) can be cast in the following integral form:

$$E_{ys}(x,z) = k_0^2 \int_0^L dz' \, \delta\varepsilon \int_{-\infty}^{\infty} dx' \, G_{TE}(x,z,x',z') \, E_y(x',z') \tag{6}$$

for the TE polarization. For the TM polarization, we get:

$$H_{ys}(x,z) = k_0^2 \int_0^L dz' \, \delta\varepsilon \int_{-\infty}^{\infty} dx' \, G_{TM}(x,z,x',z') \, H_y(x',z') - \int_0^L dz' \left[\frac{\varepsilon'}{\varepsilon} - \frac{\varepsilon_b'}{\varepsilon_b} \right] \int_{-\infty}^{\infty} dx' \, G_{TM}(x,z,x',z') \frac{\partial}{\partial z'} H_y(x',z') \tag{7}$$

where G_{TE} and G_{TM} are the Green's functions for the TE and TM polarizations, respectively, and are given as the solution of:

$$\nabla^2 G_{TE} + k_0^2 \varepsilon_b G_{TE} = -\delta(x-x') \delta(z-z') \tag{8a}$$

$$\nabla^2 G_{TM} - \frac{\varepsilon_b'}{\varepsilon_b} \frac{\partial}{\partial z} G_{TM} + k_0^2 \varepsilon_b G_{TM} = -\delta(x-x') \delta(z-z') \tag{8b}$$

The source-type integral equation is then solved by applying successive iterations where a Distorted-Born approximation is applied at each iteration step. For the iteration scheme to converge, $|E_{ys}|$ and $|H_{ys}|$ have to be small. It is clear that the term on the right-hand side of eq. (6) and the first term on the right-hand side of eq. (7) can be made arbitrarily small by either lowering the frequency of operation k_0 or making $|\delta\varepsilon|$ small. However, the second term on the right-hand side of eq. (7) can only be made small by making $|\delta\varepsilon|$ small, i.e., if $\varepsilon_b(z)$ is sufficiently close to $\varepsilon(z)$. Thus, one can conclude that by choosing a frequency of operation that is sufficiently low, the iteration can be made to converge in the case of the TE polarization even for fairly large values of $|\delta\varepsilon|$, whereas in the case of the TM polarization, the only way the iteration will converge is when the initial guessed profile $\varepsilon_b(z)$ is chosen to be very close to the true profile $\varepsilon(z)$. It is interesting to note that the presence of the second term on the right-hand side of eq. (7), causes the TM measurement to be more sensitive to abrupt changes in the permittivity profile. Thus, the TM measurement is a better candidate than the TE case for imaging applications where one can delineate boundaries.

Another difference between the TE and TM polarizations lies in the degree of nonlinearity associated with each case. It is clear that eqs. (6) and (7) are nonlinear integral equations in the unknown profile $\varepsilon(z)$ due to the nonlinear dependence of the field (E_y or H_y) on $\varepsilon(z)$. Using a Born-type approximation in carrying out the iteration is in effect linearizing the problem. This linearization is expected to work better in the case of the TE polarization than in the TM case because the TM case is highly nonlinear compared to the TE case. This can be seen by transforming eqs. (2) and (4) into a canonical form for comparison. This is done by first carrying out a Fourier transform along the x-direction (assuming k_x to be the transform variable) and then introducing the field transformations

$$u(k_x, z) = \tilde{E}(k_x, z) \ , \qquad \text{for TE} \tag{9a}$$

$$u(k_x, z) = \varepsilon^{1/2} \tilde{H}(k_x, z) \ , \qquad \text{for TM} \tag{9b}$$

This yields the Schroedinger-type equation in the field variable u

$$\frac{\partial^2 u}{\partial z^2} + \gamma^2 u = -q u \tag{10}$$

where γ is given by

$$\gamma^2 = k_0^2 \varepsilon_b - k_x^2 \tag{11}$$

and

$$q = k_0^2 (\varepsilon - \varepsilon_b) , \qquad \text{for TE} \qquad (12a)$$

$$q = k_0^2 (\varepsilon - \varepsilon_b) - \frac{3}{4} \left[\frac{\varepsilon'}{\varepsilon} \right]^2 + \frac{1}{2} \frac{\varepsilon''}{\varepsilon} , \qquad \text{for TM} \qquad (12b)$$

Note that the right-hand side of eq. (10) can be interpreted as a source term resulting from the medium inhomogeneities in the region $z > 0$. From eq. (12), it is thus clear that for the TE polarization, $\varepsilon(z)$ is directly calculable from q; however, it is necessary to solve a second-order nonlinear differential equation to obtain $\varepsilon(z)$ for the TM case. Thus, the TM case is relatively nonlinear compared to the TE case.

3. THE RENORMALIZED SOURCE-TYPE INTEGRAL EQUATION APPROACH

The Renormalized Source-Type Integral Equation approach[9,10] can be summarized in the following three simple steps:

Step 1. The Inverse Source Problem: From the collected data on the surface of the probed medium ($\mathbf{r} \in S_m$), the currents induced inside the medium, $\mathbf{J}(\mathbf{r})$, are solved for from the following equation:

$$\int d\bar{r}' \, \bar{\bar{G}}_b(\bar{r}, \bar{r}') \cdot \bar{J}(\bar{r}') = \bar{E}(\bar{r}) - \bar{E}_b(\bar{r}) \big|_{\bar{r} \in S_m} \qquad (13)$$

Step 2. The Forward Problem: From the knowledge of the currents induced inside the slab (obtained from step 1), the electric field, $\mathbf{E}(\mathbf{r})$, can be calculated everywhere (inside as well as outside the slab) from the following equation:

$$\bar{E}(\bar{r}) = \bar{E}_b(\bar{r}) + \int d\bar{r}' \, \bar{\bar{G}}_b(\bar{r}, \bar{r}') \cdot \bar{J}(\bar{r}') \qquad (14)$$

Step 3. The Inversion Equation: From the knowledge of the currents induced inside the slab (obtained from step 1) and the electric field inside the slab (computed from step 2), the unknown difference profile $Q(\mathbf{r}) = \omega^2 \mu_0 [\varepsilon(\mathbf{r}) - \varepsilon_b]$ is obtained from the following constitutive relation:

$$Q(\bar{r}) \, \bar{E}(\bar{r}) = \bar{J}(\bar{r}) \qquad (15)$$

Thus, this method recasts the inversion, which is nonlinear in nature, in terms of the solution of a set of linear equations; however, the final inversion equation is still nonlinear. In this paper, the inversion scheme is demonstrated for the cases where the exciting source is of the dipole type that generates only TE or TM polarized waves. The data required for inversion are the tangential components of the electric and/or magnetic fields at various locations on the surface of the probed medium performed at a number of frequencies. In the next section this inversion approach is tested on a one-dimensional profile where data are generated by exciting the medium once by a horizontal magnetic dipole (exciting TE-polarized waves) and a second time by a horizontal electric dipole (exciting TM-polarized waves).

4. RESULTS

In this section we apply the inversion algorithm described in the previous section to the problem depicted in figure 2.

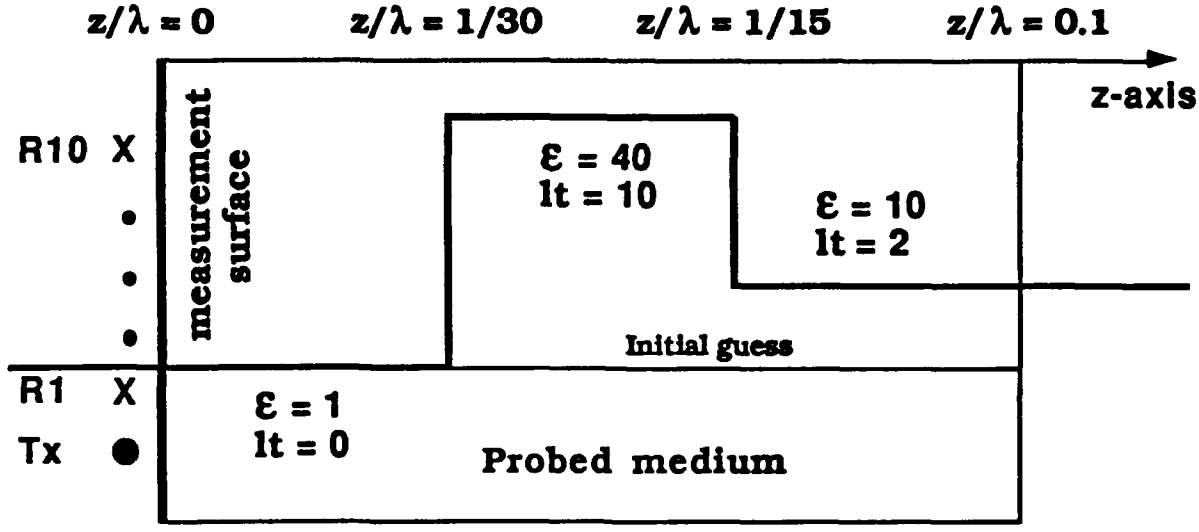

Figure 2. Permittivity profile used in the inversion

The data used in the inversion are generated by exciting the medium once by a horizontal magnetic dipole (exciting TE-polarized waves) and a second time by a horizontal electric dipole (exciting TM-polarized waves). The data are collected at ten receiver locations with the appropriate type and orientation. A single electric field component (E_ϕ) is measured for the TE case whereas two electric field components (E_z and E_ρ) are measured for the TM case. Note that the dimensions of the slab is normalized to the free space wavelength.

Figure 3a shows the result of inversion using only TE-polarized data whereas figure 3b shows the result of inversion using only TM-polarized data. From figure 3a, it is clear that the reconstructed profile employing TE data is a filtered (or a smoothed) version of the true profile and hence TE-polarized data offer poorer resolution in delineating abrupt changes in the permittivity profile. On the other hand TM-polarized data offer a higher resolution, however, the inverted profile exhibits nonlinear effects depicted by the presence of horn-type features in the reconstructed profile. From figure 3, it is also clear that TE-inversion offers higher accuracy than TM in retrieving the permittivity values around the peak of the profile. It is also interesting to note that the TM-inversion has a shallow depth of investigation which is manifested by the lower resolution at the further edge of the profile compared to the higher resolution at the near edge. Finally, the TE-based inversion converged after 8 iterations whereas the TM-based inversion converged after 33 iterations. Hence, faster convergence can be achieved by employing TE-polarized data.

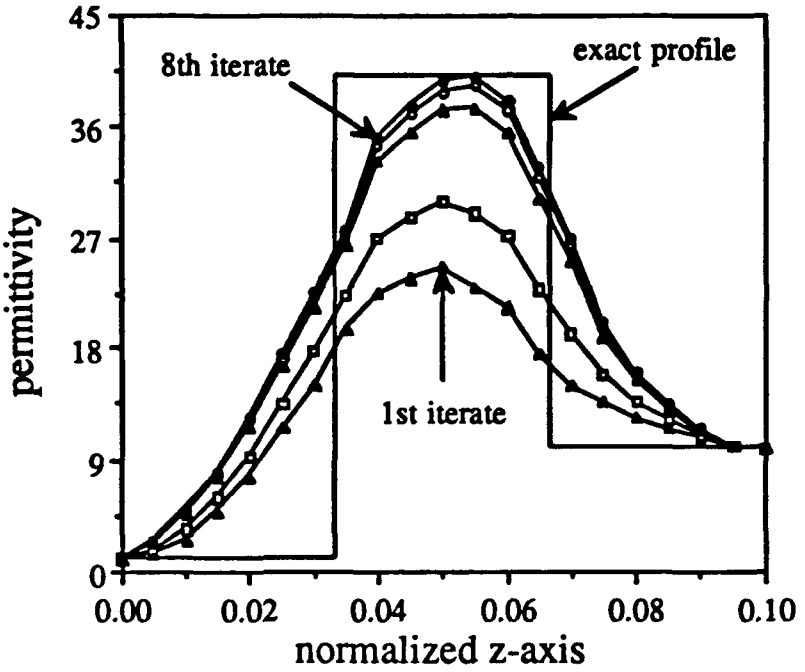

Figure 3a. Inversion result employing TE-polarized CW data

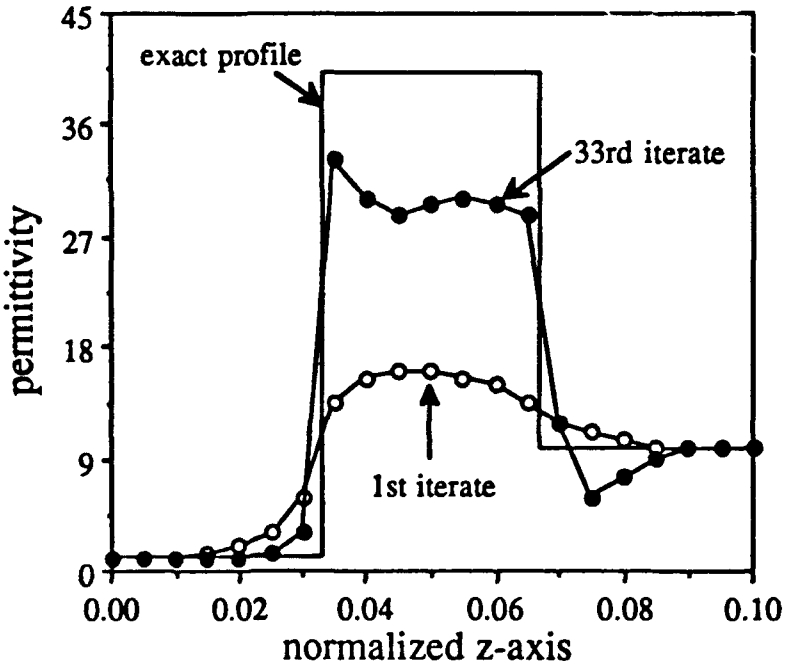

Figure 3b. Inversion result employing TM-polarized CW data.

Figure 4 shows the result of inversion combining both TE and TM polarized data where improved resolution and accuracy has been achieved.

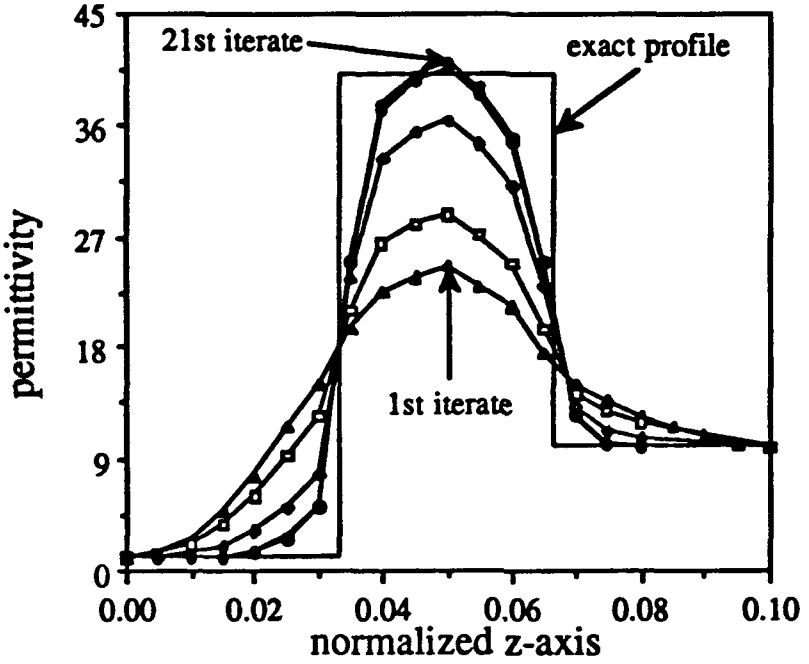

Figure 4. Inversion result employing the combined TE and TM polarized CW data.

5. CONCLUSIONS

In this paper we have presented a new and exact inversion equation which is applicable to data of TE, TM or hybrid polarization. If approximations are to be made they will occur in the numerical methods employed in the solution of this inversion equation. This is to be distinguished from other methods, e.g., Born inversion, ray tracing, etc., which are inherently approximate and are hard to improve when they give inaccurate results. The inversion equation is a closed form summation of the iterative (or perturbative) Neumann (or Born) series of the Source-Type Integral Equation. This equation is a valid representation even in the case when the Born series diverges.

6. REFERENCES

1. A. Roger, D. Maystre, and M. Cadilhac, "On a Problem of Inverse Scattering in Optics: The Dielectric Inhomogeneous Medium," *J. Optics (Paris)*, vol. 9, pp. 83-90, 1978.

2. S. Coen, K.K. Mei, and D.J. Angelakos, "Inverse Scattering Technique Applied to Remote Sensing of Layered Media," *IEEE Trans. Antennas Propagat.*, vol. AP-29, pp. 298-306, 1981.

3. A.G. Tijhuis and C. Van Der Worm, "Iterative Approach to the Frequency-Domain Solution of the Inverse-Scattering Problem for an Inhomogeneous Lossless Dielectric Slab," *IEEE Trans. Antennas Propagat.*, vol. AP-32, pp. 711-716, 1984.

4. D. Lesselier, "Optimization Techniques and Inverse Problems: Reconstruction of Conductivity Profiles in the Time Domain," *IEEE Trans. Antennas Propagat.*, vol. AP-30, pp. 59-65, 1982.

5. A.G. Tijhuis, "Iterative Determination of Permittivity and Conductivity Profiles of a Dielectric Slab in the Time Domain," *IEEE Trans. Antennas Propagat.*, vol. AP-29, pp. 239-245, 1981.

6. W. Tabbara, "Reconstruction of Permittivity Profiles from a Spectral Analysis of the Reflection Coefficient," *IEEE Trans. Antennas Propagat.*, vol. AP-27, pp. 241-248, 1979.

7. T.M. Habashy, W.C. Chew, and E.Y. Chow, "Simultaneous Reconstruction of Permittivity and Conductivity Profiles in a Radially Inhomogeneous Slab", *Radio Science*, vol. 21, pp. 635-645, 1986.

8. T.M. Habashy and R. Mittra, "On Some Inverse Methods in Electromagnetics," *Journal of Electromagnetic Waves and Applications (JEWA)*, vol. 1, pp. 25-58, 1987.

9. T.M. Habashy, E.Y. Chow, and D.G. Dudley, URSI meeting, Blacksburg, Virginia, June 15-19, 1987.

10. T.M. Habashy, E.Y. Chow, and D.G. Dudley, "Profile Inversion Using the Renormalized Source-Type Integral Equation Approach," *IEEE Trans. Antennas Propagat.*, vol. AP-38, pp. 668-682, 1990.

Paper submitted to the *Journal of Vacuum Science and Technology* as part of the proceedings of the *35th International Symposium on Electron, Ion, and Photon Beams* (paper E84), Seattle, Washington, May 28-31, 1991.

Electromagnetic calculation of soft x-ray diffraction from 0.1 μm-scale gold structures

M. L. Schattenburg

Center for Space Research, Massachusetts Institute of Technology, 77 Massachusetts Avenue, Cambridge, MA 02139, USA

K. Li, R. T. Shin, J. A. Kong, D. B. Olster, and Henry I. Smith

Research Laboratory of Electronics, Massachusetts Institute of Technology, 77 Massachusetts Avenue, Cambridge, MA 02139, USA

Because the effects of diffraction during proximity-print x-ray lithography are of critical importance, a number of previous researchers have attempted to calculate the diffraction patterns and minimum achievable feature sizes as a function of wavelength and gap. Work to date has assumed that scalar diffraction theory is applicable—as calculated, for example, by the Rayleigh-Sommerfeld formulation—and that Kirchhoff boundary conditions can be applied. Kirchhoff boundary conditions assume that the fields (amplitude and phase) are constant in the open regions between absorbers, and a different constant in regions just under the absorbers (i.e., that there are no fringing fields). An x-ray absorber is, however, best described as a lossy dielectric that is tens or hundreds of wavelengths tall, and hence Kirchhoff boundary conditions are unsuitable. In this report we use two numerical techniques to calculate (on a Cray 2 supercomputer) accurate diffracted fields from gold absorbers for two cases: a 30 nm-wide line at λ = 4.5 nm, and a 100 nm-wide line at λ = 1.3 nm. We show that the use of Kirchhoff boundary conditions introduces unphysically high spatial frequencies into the diffracted fields. The suppression of these frequencies—which occurs naturally without the need to introduce an extended source or broad spectrum—improves exposure latitude for mask features near 0.1 μm and below.

I. INTRODUCTION

The limits and practicality of proximity-print x-ray lithography continues to be a topic of discussion and debate. Of particular concern are the limits of resolution imposed by the effects of diffraction. Because the mechanical limits imposed on the mask-substrate gap during the volume manufacturing of ULSI circuits are not presently certain, it remains prudent to ask: what is the minimum practical feature size that can be printed at a given gap?

In order to resolve these issues, a series of papers have appeared in the literature which present theoretical calculations for the diffraction of x rays from mask absorbers. Early papers simply considered absorption [1-3], but later papers also included the effects of phase-shift [4-8]. Most recently, authors have included the effects of source spatial and temporal coherence, and have generated exposure "trees" which allow the determination of exposure latitude versus gap for various types of mask features [9-15].

The method most commonly used to calculate the diffraction pattern is to apply a Fresnel-Kirchhoff or Rayleigh-Sommerfeld diffraction integral [16,17], or a more sophisticated formulation (Hopkin's formula) which takes into account source partial coherence [18]. These calculations can be carried out either in the spatial or the spatial-frequency domain. In any of these cases, approximate boundary conditions known as Kirchhoff boundary conditions (KBC) are generally applied. KBC assume that the field (amplitude and phase) is constant in the open regions between absorbers, and also constant (but attenuated and phase shifted) in regions just under the absorbers—in other words, that there are no fringing fields at the boundary between the two regions.

In general, KBC apply when the wavelength, λ, is much smaller than the lateral size, d, of the feature being printed—which is the case in most x-ray lithography (e.g., d = 0.1 μm, λ = 1 nm). However, what is not generally recognized is that KBC will not necessarily apply when the absorbers are lossy dielectrics that are tens or hundreds of wavelengths tall.

Work to date concerning the printability of 0.25 μm features is probably reasonably accurate. However, in this report we show that the assumption of KBC for features near 0.1 μm and below is not tenable. In particular, we show that the suppression of the undesirable high-spatial-frequency components—

which some authors note an extended source and/or a broad spectrum achieves—occurs naturally in the absorber due to the "lossy dielectric" effect.

II. CALCULATIONS

We used two different methods to calculate the diffraction from gold absorbers: the Method of Moments (MoM) and the Finite Difference-Time Domain (FD-TD) method. (We used two algorithms in order to check for consistency.) The only approximations inherent in these methods are in the discretization of the object space and Maxwell's equations. Because the discretization can performed on a scale that is small compared to the wavelength, and furthermore the discretization scale can be reduced until convergence is achieved, accuracy is assured.

Of these two techniques, the MoM is typically faster and uses less memory for single-frequency calculations. On the other hand, the FD-TD method is simpler to code and therefore less likely to have errors. In practice we ran small test cases using both methods and then increased the spatial resolution (reduced discretization scale) until both methods converged to the same solution. Then the computationally-intensive cases reported here were calculated with the MoM.

A. METHOD OF MOMENTS

The Method of Moments (MoM) is a numerical technique useful in the solution of steady-state electromagnetic wave scattering and radiation problems [19,20]. The method calculates steady-state fields on the surface of a closed dielectric object in free space, which is impinged upon by a known exciting wave. The surface of the object is broken up into small patches which are small compared to the wavelength. The surface currents at each patch and thus the tangential surface fields are then calculated. Computation time was up to two hours on a Cray 2. Once the fields are known on the boundary of the object they can readily be propagated to any desired point or plane [16,17].

B. FINITE DIFFERENCE-TIME DOMAIN METHOD

The Finite Difference-Time Domain (FD-TD) method is a numerical technique useful in the solution of time-dependent electromagnetic wave scattering and radiation problems [21-24]. The method involves the formation of a computational domain which encompasses the object of interest and is typically several times larger. The entire domain inside the boundary—including the object—is discretized on a rectangular grid. The spacing between adjacent nodes on the grid is small compared to the wavelength. A clock is started and incremented in time steps that are small compared to the light-travel time between adjacent nodes. Then discretized forms of Maxwell's equations are used to calculate the fields at each node from the fields at nearby nodes which were in effect at the previous time step. Absorbing boundary conditions are imposed at the edges of the computational domain in order to simulate unbounded space. Also, a boundary condition is typically imposed on a surface surrounding the object to simulate an incoming plane wave. The result can be displayed as a video image of the fields inside the domain. Computation time was up to one hour on a Cray 2. In practice the calculation is run until steady state is achieved, and the fields at nodes along a line just under the absorber are saved for comparison with the MoM results.

III. RESULTS

Calculations were performed using MoM and FD-TD on single gold parallelepiped absorbers, infinite in length and rectangular in cross-section, which were impinged upon by a monochromatic plane wave. The electric-field polarization was used (E-field perpendicular to the page). (The magnetic-field polarization yielded results similar to the electric-field polarization.) These were compared to the results of a Rayleigh-Sommerfeld-Kirchhoff (RSK) calculation [16]. We considered two cases (see Table I), which were selected in order to explore a range of spatial frequencies: Case 1, which is a 30x100 nm absorber with the 4.5 nm (C_K) x ray, and Case 2, which is a 100x250 nm absorber with the 1.3 nm (Cu_L) x ray. Note that the attenuation of the absorber in both cases is roughly equivalent. (~12 dB).

A. CASE 1 (λ = 4.5 nm)

Figs. 1 (a) to (d) show the resulting intensities or irradiance distributions for both the MoM and RSK methods calculated for α from 0-1.5 (gap G from 0-0.3 μm). Here α is a dimensionless gap given by $\alpha = G\lambda/W^2$, where G is the gap, λ is the wavelength, and W is the linewidth. Note the suppression of high spatial frequencies in the MoM calculation, and the "fuzzy edge" of a few tens of nanometers in extent. Figs. 2 (a) and (b) show the beneficial effects of the suppression of high spatial frequencies on exposure latitude in the form of exposure "trees" [9-12] which plot ±10 % linewidth contours versus α. Here we have used a line bias of 33 % (40 nm resist line). (A line bias is the use of a smaller-than-desired feature size in the mask than on the wafer in order to compensate for diffractive broadening.) An enlightening way to view the suppression of high spatial frequencies is to plot the intensity of the waves at $\alpha = 0$ (gap G = 0) as a function of spatial frequency, as shown in Fig. 3. Note that at low spatial frequencies the RSK and MoM calculations agree, but the MoM calculation "rolls off" at around 0.05 nm^{-1}.

B. CASE 2 (λ = 1.3 nm)

The results for the intensities versus α for Case 2 are shown in Figs. 4 (a) to (d). Note that even though the wavelength is much smaller, the "fuzzy edge" length is roughly the same—a few tens of nanometers. This may be due to the smaller wavelength (3.3× smaller) being partially compensated by a taller absorber (2.5× taller). The exposure trees are shown in Figs. 5 (a) and (b). Here we have used a line bias of 50% (150 nm resist line). The intensity versus spatial frequency is shown in Fig. 6. Note that the roll-off in this case is still around 0.05 nm^{-1}, but that this represents a higher spatial frequency *relative* to the information content in the larger-line/smaller-wavelength case.

IV. CONCLUSION

We have shown that the use of Kirchhoff boundary conditions introduces unphysically high spatial frequencies into the diffracted fields. The natural suppression of these frequencies by the electromagnetic properties of x-ray

absorbers tremendously improves exposure latitude for mask features near 0.1 μm and below.

ACKNOWLEDGEMENTS

We would like to thank E. Gullikson, K. Early, and F. Davis for useful discussions. This work was sponsored in part by the National Science Foundation (Grant ECS-8709806), the Office of Naval Research (Contract N00014-90-K-2108), the Joint Services Electronics Program (DAAL03-89-C-0001), and NASA (Contract NAS8-36748).

1) K. Heinrich, H. Betz, A. Heuberger, and S. Pongratz, J. Vac. Sci. Technol. 19, 1254 (1981).
2) N. Atoda, H. Kawakatsu, H. Tanino, S. Ichimura, M. Hirata, and K. Hoh, J. Vac. Sci. Technol. B 1, 1267 (1983).
3) H. Betz, K. Heinrich, A. Heuberger, H. Huber, and H. Oertel, J. Vac. Sci. Technol. B 4, 248 (1986).
4) R. Redealli, R. Tatchyn, and P. Pianetta, in *Electron-Beam, X-ray & Ion-Beam Techniques for Submicrometer Lithographies V* (Proc. SPIE **632**), ed. P. D. Blais (SPIE, Bellingham WA), 264 (1986).
5) Y. Yamakoshi, H. Atoda, K. Shimizu, T. Sato, and Y. Shimizu, Appl. Optics 25, 928 (1986).
6) M. Weiss, H. Oertel, and H.-L. Huber, Microelec. Engin. 6, 265 (1987).
7) Y.-C. Ku, E. H. Anderson, M. L. Schattenburg, and Henry I. Smith, J. Vac. Sci. Technol. B 6, 150 (1988).
8) S. Hasegawa, J. Itoh, and N. Atoda, Microelec. Engin. 8, 127 (1988).
9) B. J. Lin, in *Electron-Beam, X-ray, and Ion-Beam Technology: Submicrometer Lithographies IX* (Proc. SPIE **1263**), ed. D. J. Resnick (SPIE, Bellingham WA, 1990), p. 80.
10) B. J. Lin, Microelec. Engin. **11**, 137 (1990).
11) B. J. Lin, J. Vac. Sci. Technol. B 8, 1539 (1990).
12) J. Z. Y. Guo, G. Chen, V. White, P. Anderson, and F. Cerrina, J. Vac. Sci. Technol. B 8, 1551 (1990).
13) T. Horiuchi, K. Deguchi, S. Hirota, and A. Yoshikawa, Microelec. Engin. **13**, 315 (1991).
14) H. K. Oertel, M. Weiß, and H.-L. Huber, Microelec. Engin. **13**, 339 (1991).

15) Y. Vladimirsky and J. R. Maldonado, Microelec. Engin. **13**, 343 (1991).
16) J. W. Goodman, *Introduction to Fourier Optics* (McGraw-Hill, San Francisco, 1968).
17) M. Born and E. Wolf, *Principles of Optics, Sixth Edition* (Pergamon, Oxford, 1980), Chap. VIII.
18) M. Born and E. Wolf, *ibid.*, Chap. X.
19) R. F. Harrington, *Field Computation by Moment Methods* (Macmillan, New York, 1968).
20) J. J. H. Wang, *Generalized Moment Methods in Electromagnetics* (Wiley, New York, 1991).
21) K. S. Yee, IEEE Trans. Antennas Propagat. **AP-14**, 302 (1966).
22) A. Taflove and M. E. Brodwin, IEEE Trans. Microwave Theory Tech. MTT-23, 623 (1975).
23) G. Mur, IEEE Trans. Electromagn. Compat. EMC-23, 377 (1981).
24) K. Li, M. A. Tassoudji, R. T. Shin, and J. A. Kong, in *Conference Proceedings of the 7th Annual Review of Progress in Applied Computational Electromagnetics at the Naval Postgraduate School, Monterey, CA, March 18-22, 1991*, ed. F. Walker (The Applied Computational Electromagnetics Society, 1991), p. 38.
25) B. L. Henke, P. Lee, T.J. Tanaka, R. L. Shimabukuro, and B. K. Fujikawa, Atomic Data and Nuclear Data Tables 27, 1 (1982); private comm. (1989).

Figure Captions

FIG. 1. Intensity vs. lateral position for Case 1. (a) $\alpha = 0$ (gap = 0), (b) $\alpha = 0.5$ (gap = 0.1 μm), (c) $\alpha = 1.0$ (gap = 0.2 μm), (d) $\alpha = 1.5$ (gap = 0.3 μm).

FIG. 2. Exposure trees vs. α (dimensionless gap) for Case 1. (Gaps range from 0-0.3 μm.) The line is biased 33% (40 nm resist line). (a) MoM solution, (b) Rayleigh-Sommerfeld-Kirchhoff approximation.

FIG. 3 Intensity vs. spatial frequency for Case 1. Note roll-off at 0.05 nm^{-1}.

FIG. 4 Intensity vs. lateral position for Case 2. (a) $\alpha = 0$ (gap = 0), (b) $\alpha = 0.5$ (gap = 3.7 μm), (c) $\alpha = 1.0$ (gap = 7.5 μm), (d) $\alpha = 1.5$ (gap = 11.2 μm).

FIG. 5 Exposure trees vs. α (dimensionless gap) for Case 2. (Gaps range from 0-11.2 μm.) The line is biased 50% (150 nm resist line). (a) MoM solution, (b) Rayleigh-Sommerfeld-Kirchhoff approximation.

FIG. 6 Intensity vs. spatial frequency for Case 2. Note roll-off at 0.05 nm^{-1}.

TABLE I. Computational cases considered.

	Case 1	Case 2
Wavelength λ (nm)	4.48	1.334
Refractive Index [25]	$1 - 7.54\times10^{-3} + j1.04\times10^{-2}$	$1 - 2.31\times10^{-3} + j1.19\times10^{-3}$
Width W (nm)	30	100
Height (nm)	100	250
Transmission	0.0541	0.0607
Phase Shift (rad)	1.058	2.72
Patch Size (nm)	~0.64	~0.19

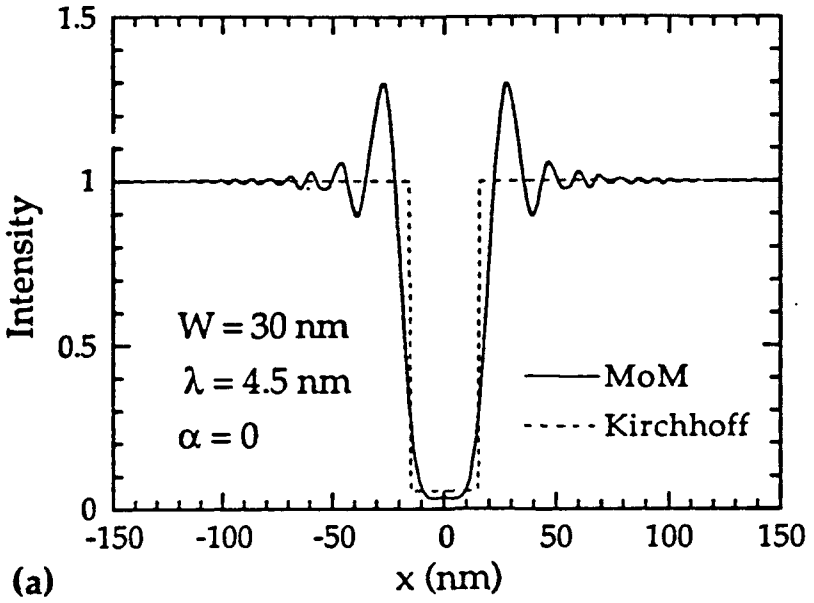
1.5
1
0.5
0
Intensity
W = 30 nm
λ = 4.5 nm
α = 0
MoM
Kirchhoff
-150
-100
-50
0
50
100
150
x (nm)
(a)

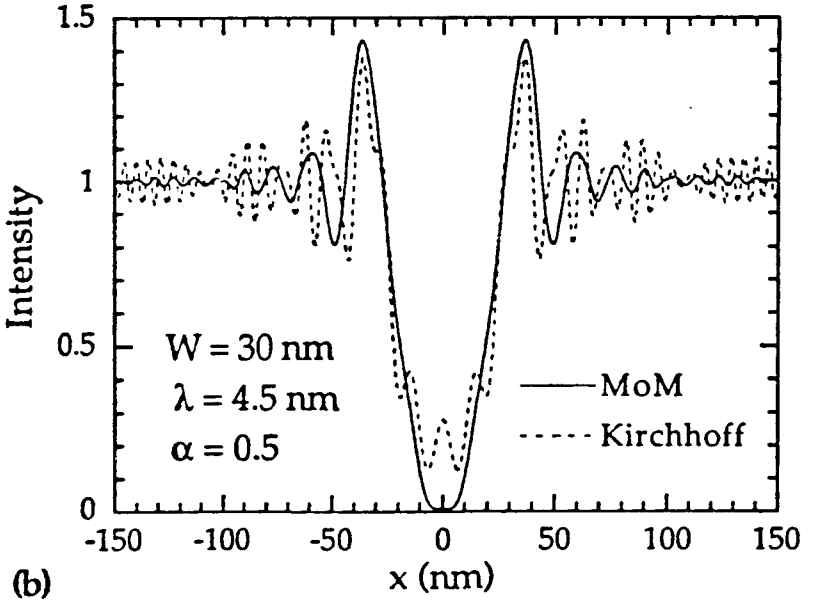
1.5
1
0.5
0
Intensity
W = 30 nm
λ = 4.5 nm
α = 0.5
MoM
Kirchhoff
-150
-100
-50
0
50
100
150
x (nm)
(b)

Fig. 1 (a), (b)

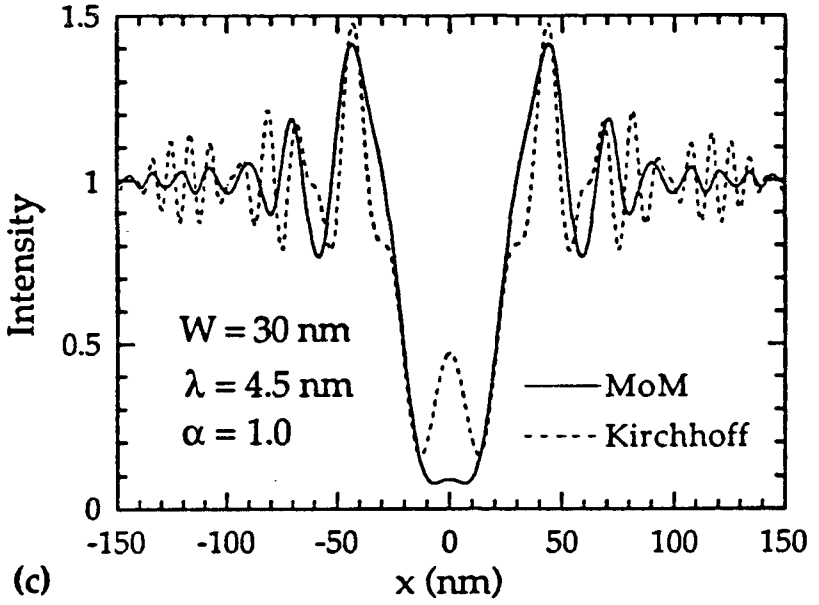
1.5
1
0.5
0
Intensity
W = 30 nm
λ = 4.5 nm
α = 1.0
MoM
Kirchhoff
-150
-100
-50
0
50
100
150
x (nm)

(c)

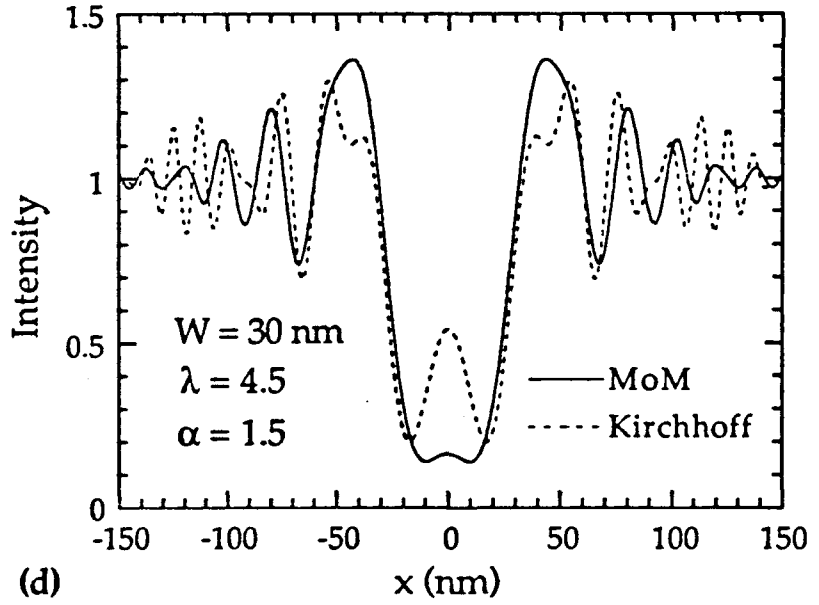
1.5
1
0.5
0
Intensity
W = 30 nm
λ = 4.5
α = 1.5
MoM
Kirchhoff
-150
-100
-50
0
50
100
150
x (nm)

(d)

Fig. 1 (c), (d)

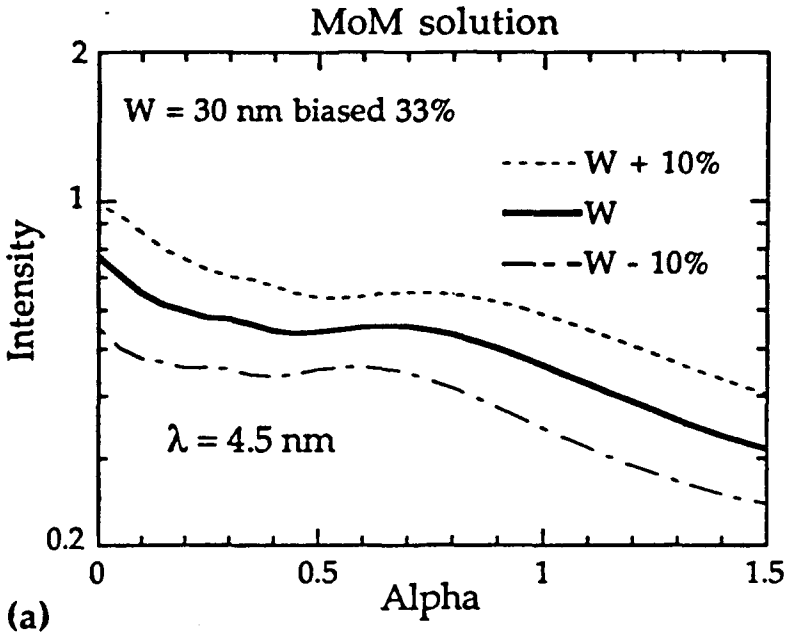
MoM solution
W = 30 nm biased 33%
W + 10%
W
W - 10%
λ = 4.5 nm
Intensity
Alpha
2
1
0.2
0
0.5
1
1.5

(a)

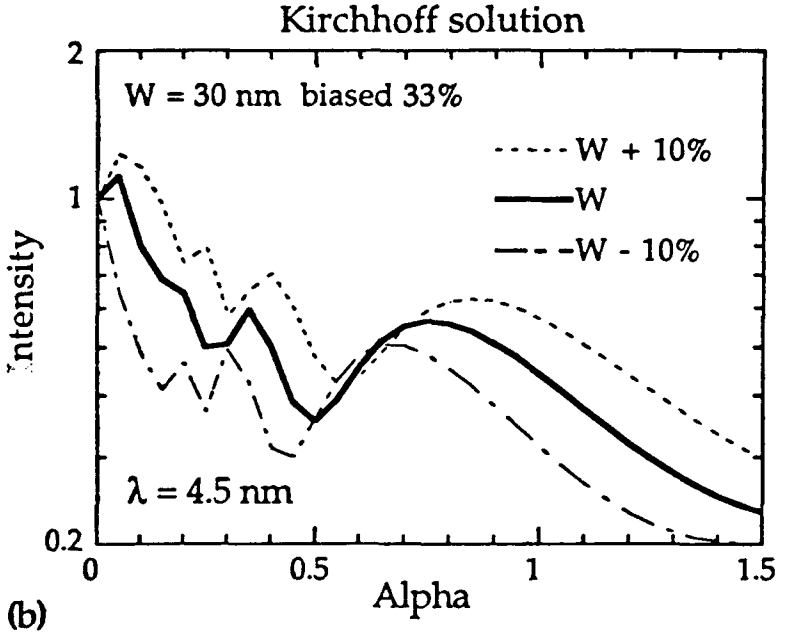
Kirchhoff solution
W = 30 nm biased 33%
W + 10%
W
W - 10%
λ = 4.5 nm
Intensity
Alpha
2
1
0.2
0
0.5
1
1.5

(b)

Fig. 2 (a), (b)

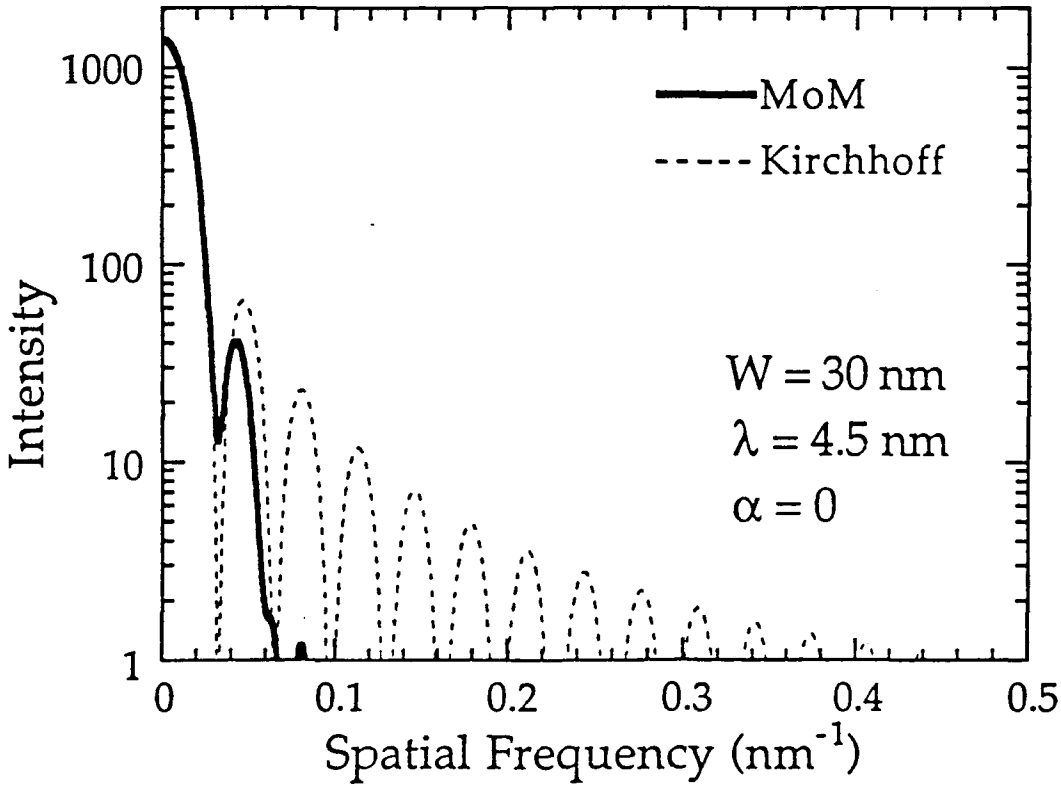
1000
100
10
1
Intensity
0
0.1
0.2
0.3
0.4
0.5
Spatial Frequency (nm^{-1})
MoM
Kirchhoff
W = 30 nm
λ = 4.5 nm
α = 0

Fig. 3

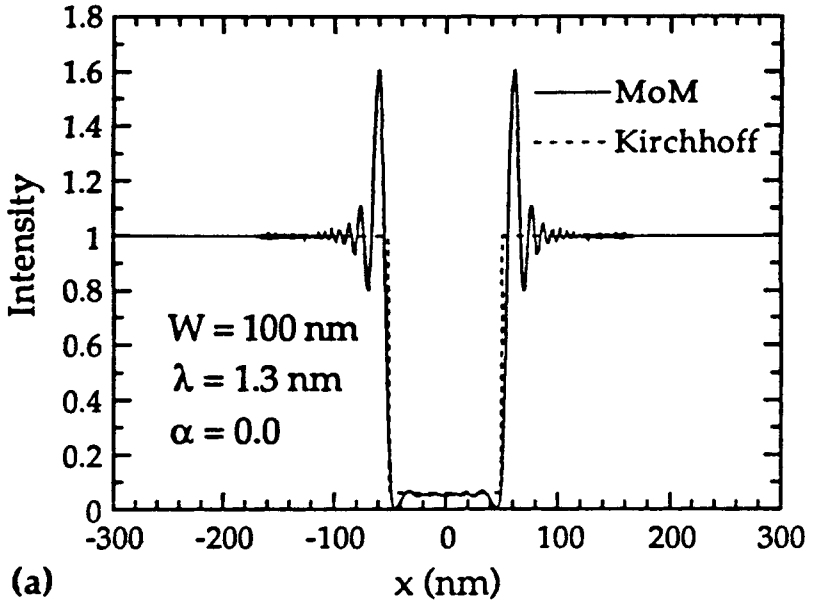
1.8
1.6
1.4
1.2
1
0.8
0.6
0.4
0.2
0
Intensity
MoM
Kirchhoff
W = 100 nm
λ = 1.3 nm
α = 0.0
-300
-200
-100
0
100
200
300
x (nm)
(a)

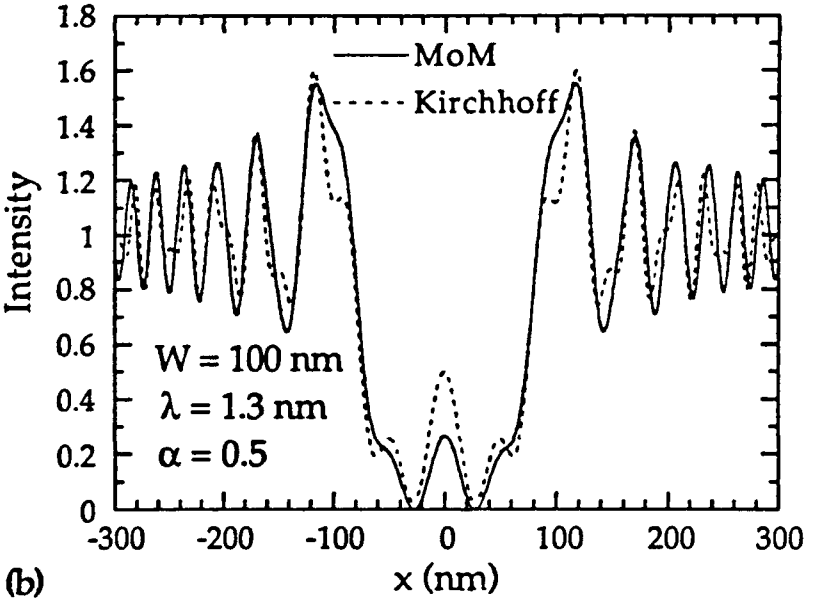
1.8
1.6
1.4
1.2
1
0.8
0.6
0.4
0.2
0
Intensity
MoM
Kirchhoff
W = 100 nm
λ = 1.3 nm
α = 0.5
-300
-200
-100
0
100
200
300
x (nm)
(b)

Fig. 4 (a), (b)

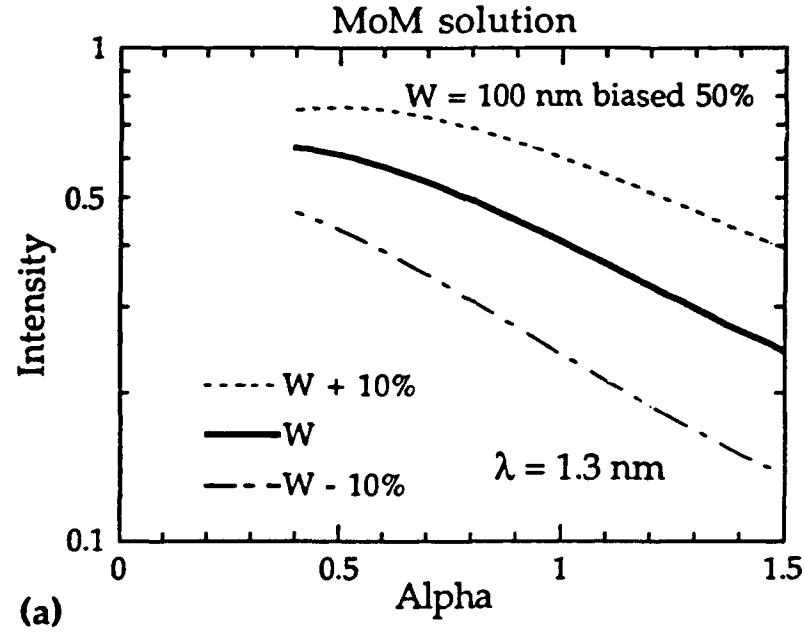
MoM solution
W = 100 nm biased 50%
W + 10%
W
W - 10%
λ = 1.3 nm
Intensity
Alpha
1
0.5
0.1
0
0.5
1
1.5

(a)

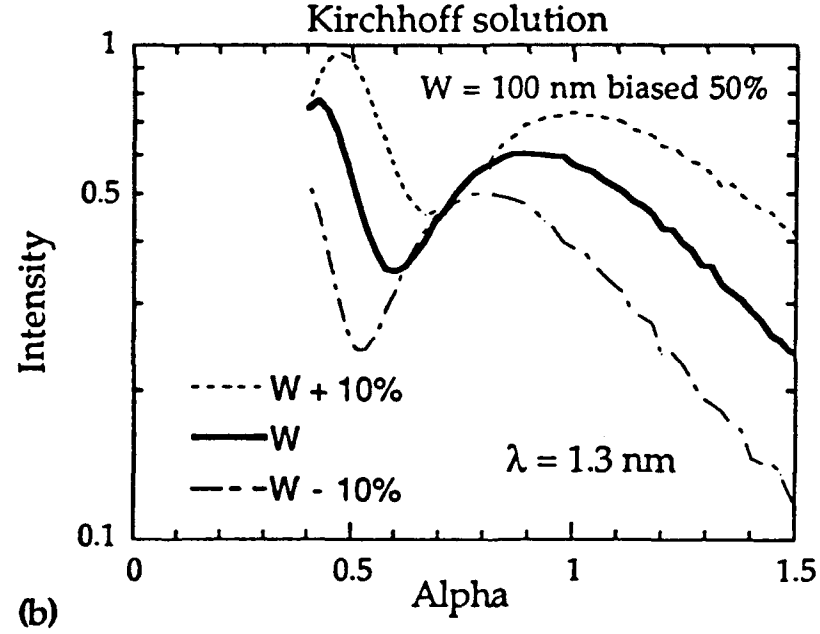
Kirchhoff solution
W = 100 nm biased 50%
W + 10%
W
W - 10%
λ = 1.3 nm
Intensity
Alpha
1
0.5
0.1
0
0.5
1
1.5

(b)

Fig. 5 (a), (b)

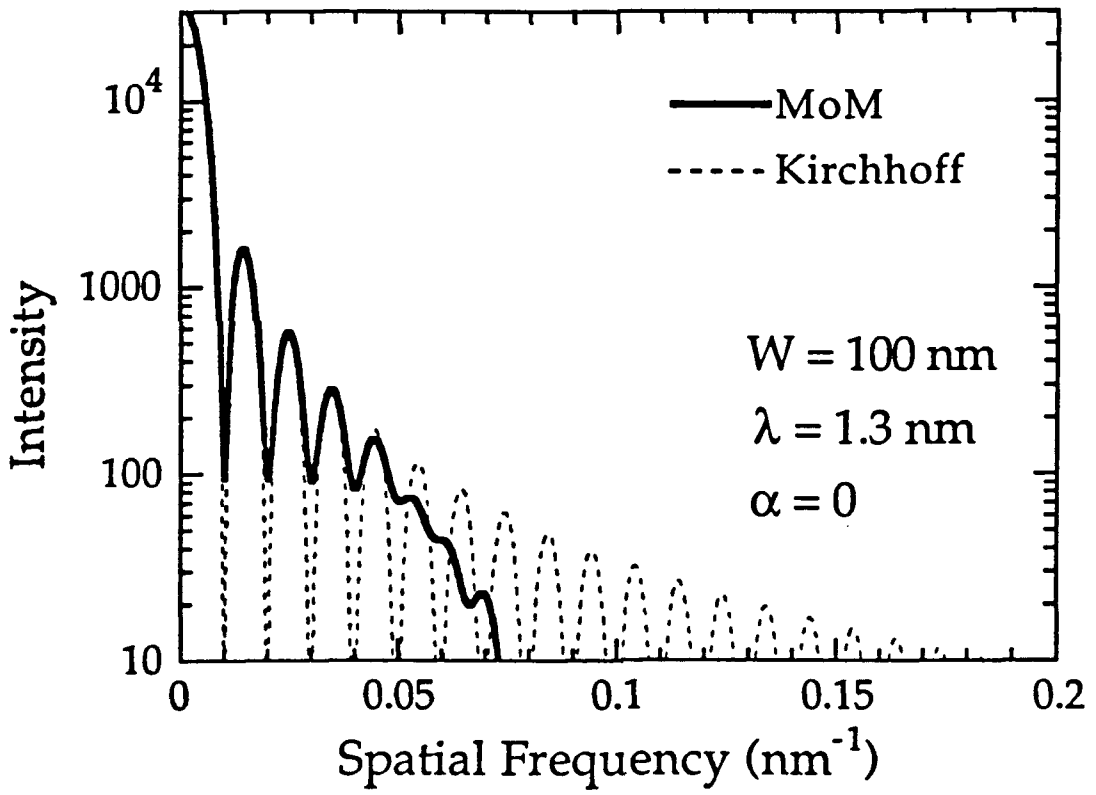
MoM
Kirchhoff
W = 100 nm
λ = 1.3 nm
α = 0
Intensity
10^4
1000
100
10
0
0.05
0.1
0.15
0.2
Spatial Frequency (nm^-1)

Fig. 6

Office of Naval Research

DISTRIBUTION LIST

Arthur K. Jordan

:ode: 1114 SE
)ffice of Naval Research
)00 North Quincy Street
\rlington, VA 22217

3 copies

\dministrative Contracting Officer
:19-628
lassachusetts Institute of Technology
:ambridge, MA 02139

1 copy

)irector
laval Research Laboratory
lashington, DC 20375
:ttn: Code 2627

6 copies

)efense Technical Information Center
)ldg. 5, Cameron Station
\lexandria, VA 22314

2 copies